HYBRID PHOTONIC CRYSTAL AND CONVENTIONAL WAVEGUIDE STRUCTURES

by

SEUNGHYUN KIM

A DISSERTATION

**Submitted in partial fulfillment of the requirements
for the degree of Doctor of Philosophy
in
The Optical Science and Engineering Program
to
The School of Graduate Studies
of
The University of Alabama in Huntsville**

HUNTSVILLE, ALABAMA

2004

In presenting this dissertation in partial fulfillment of the requirements for a doctoral degree from The University of Alabama in Huntsville, I agree that the Library of this University shall make it freely available for inspection. I further agree that permission for extensive copying for scholarly purposes may be granted by my advisor or, in his/her absence, by the Director of the Program or the Dean of the School of Graduate Studies. It is also understood that due recognition shall be given to me and to The University of Alabama in Huntsville in any scholarly use which may be made of any material in this dissertation.

__________________________ ____________

(student signature) (date)

DISSERTATION APPROVAL FORM

Submitted by Seunghyun Kim in partial fulfillment of the requirements for the degree of Doctor of Philosophy in Optical Science and Engineering and accepted on behalf of the Faculty of the School of Graduate Studies by the dissertation committee.

We, the undersigned members of the Graduate Faculty of The University of Alabama in Huntsville, certify that we have advised and/or supervised the candidate on the work described in this dissertation. We further certify that we have reviewed the dissertation manuscript and approve it in partial fulfillment of the requirements of the degree of Doctor of Philosophy in Optical Science & Engineering.

___________________________________ Committee Chair

____

____

____

____

____

___________________________________ Program Director

___________________________________ College Dean

___________________________________ Graduate Dean

ABSTRACT
School of Graduate Studies
The University of Alabama in Huntsville

Degree Doctor of Philosophy Program Optical Science and Engineering

Name of Candidate Seunghyun Kim

Title Hybrid Photonic Crystal and Conventional Waveguide Structures

Higher levels of integration are required in planar lightwave circuits (PLCs) to lower costs and increase functionality in smaller footprint. Many different approaches using conventional waveguides (CWGs) and photonic crystal (PhC) structures have been proposed to meet such demands. CWGs are attractive due to low propagation loss, low coupling loss to and from fiber, and low dispersion. However the large radius of curvature required for high efficiency bends limits the possible level of integration in PLCs. Alternatively, PhCs have received much attention due to their capability to manipulate light propagation in a compact region. However, high propagation loss and coupling loss from and to fiber are problematic issues for PhC structures.

In this dissertation, I examine the combination of PhCs and CWGs in hybrid structures that leverage the advantages of each approach. Hybrid structures consist of CWGs for the low loss transport of light integrated with PhC regions of very limited spatial extent to dramatically reduce the size of waveguide devices. This preserves the traditional advantages of CWGs while advantageously using the attractive properties of PhCs.

Ultracompact high efficiency 90 degree bends, splitters, and a polarizing beam splitter using hybrid PhC and CWG structures are numerically designed and analyzed. Wave vector diagrams have been used to understand hybrid PhC and CWG structures. For some cases, diffraction at the periodic boundary surface of PhC limits the maximum 90 degree bend efficiencies. A micro genetic algorithm (μGA) combined with 2-D finite difference time domain (FDTD) method is used to effectively suppress undesired diffraction by manipulating parameters of the PhC region and the periodic boundary layer which in turn maximizes the bend efficiency. A compact Mach-Zender interferometer and ring resonators are designed by combining ultracompact high efficiency hybrid PhC and CWG 90 degree bend and splitter structures. The proposed Mach-Zender interferometer and ring resonator show attractive performance characteristics and design flexibilities.

Abstract Approval: Committee Chair ______________________________

(Date)

Department Chair ______________________________

Graduate Dean ______________________________

ACKNOWLEDGMENTS

I would like first to thank my advisor, Dr. Greg Nordin, for his invaluable guidance throughout entire process of the work. This work would not have been possible without his support in innumerable ways. Secondly, I thank committee members for their helpful comments. I also would like to thank staffs and graduate students of the Nano and Micro Devices Laboratory (NMDL) for their support and collaboration.

Finally, very special thanks go to my wife, Younglim Lee. She provided not only support but also encouragement throughout the work. I also would like to thank my parents for their care and support to pursue education.

TABLE OF CONTENTS

Page

LIST OF FIGURES x

LIST OF SYMBOLS xix

Chapter 1 INTRODUCTION 1

1.1 Motivation 1

1.2 Overview of the dissertation 3

1.3 New contributions 5

Chapter 2 BACKGROUND 7

2.1 Conventional waveguides 7

2.1.1 Review of conventional waveguides 7

2.1.2 Conventional waveguide issues 12

2.2 Photonic Crystals (PhC) 14

2.2.1 Review of photonic crystals 14

2.2.2 Photonic bandgap and PhC waveguide 20

2.2.3 Photonic crystal slab and problems 23

2.3 Computational tools 24

2.3.1 MIT photonic-bands (MPB) 24

2.3.2 Finite difference time domain (FDTD) method 25

2.3.3 Micro genetic algorithm (μGA) 27

2.4 Conclusions 27

Chapter 3 HYBRID PHC AND CWG STRUCTURES FOR A LOW REFRACTIVE INDEX WAVEGUIDE WITH A LOW INDEX CONTRAST 29

3.1 Ultracompact high efficiency CWG bend structure 29

3.2 High efficiency beamsplitter 35

3.3 Mach-Zender interferometer using hybrid bends and beamsplitters 36

3.4 Conclusions 38

Chapter 4 A POLARIZING BEAM SPLITTER USING A HYBRID PHC AND CWG STRUCTURE 39

4.1 Design and analysis 39

4.2 Fabrication tolerance of the structure 46

4.3 Conclusions 48

Chapter 5 HYBRID PHC AND CWG STRUCTURES FOR A HIGH REFRACTIVE INDEX WAVEGUIDE WITH A LOW INDEX CONTRAST 49

5.1 90° bend – TE polarization and triangular PhC lattice 50

5.2 90° bend – TM polarization and square PhC lattice 56

5.3 High efficiency beam splitters 61

5.4 Conclusions 64

Chapter 6 ULTRACOMPACT HIGH EFFICIENCY BEND STRUCTURE FOR LOW INDEX WAVEGUIDE USING AIR HOLE PHC STRUCTURES 65

6.1 Designs and numerical simulation results for silica waveguide bend 65

6.2 Designs and numerical simulation results for Waveguide 1 72

6.3 Designs and numerical simulation results for Waveguide 2 75

6.4 Conclusions 77

Chapter 7 NEW RING RESONATOR CONFIGURATION USING HYBRID PHC AND CWG STRUCTURES.. 79

7.1 Motivation.. 80

7.2 Design of a ring resonator... 81

7.3 Ring resonators with larger FSR and Q factor than the base structure............. 87

7.4 Conclusion 92

Chapter 8 DISCUSSION AND CONCLUSIONS... 93

8.1 Summary.. 94

8.2 Future research.. 96

8.2.1 Fabrication of the hybrid PhC and CWG structures.................................... 96

8.2.2 Design devices using hybrid PhC and CWG structures 97

APPENDIX: ANALYSIS FOR THE RING RESONATOR USING HYBRID PHOTONIC CRYSTAL AND CONVENTIONAL WAVEGUIDE STRUCTURES..... 99

REFERENCES 103

LIST OF FIGURES

Figure Page

2.1 Geometrical interpretations of a waveguide and its wave vector space analyses for three different light propagation angles. There is a possible mode in the cladding region when light propagates with an angle smaller than the critical angle. 8

2.2 Waveguide bend geometry. T is the thickness of a single mode waveguide and R is the radius of curvature of the bend. This figure shows the power radiation from the outer tail side of the waveguide mode by the waveguide bend [4]. 13

2.3 Basic 1-D (left) and 2-D PhC structures composed of a square (center) and triangular (right) periodic arrays. 15

2.4 Geometry of a square lattice PhC (left) in real space and its counterpart in the reciprocal space (right). The Brillouin zone is indicated in the right figure. 19

2.5 Photonic bandgap for TM polarization along the Γ-X direction of a square lattice PhC. Calculation results with MPB (dispersion relation) and 2-D FDTD (transmission) are presented with the geometry (right). 21

2.6 Dispersion relation showing the photonic bandgap and PhC waveguide mode (gray curve in the photonic bandgap region) for a square Si posts PhC and time snap shots of PhC waveguide modes for three different frequencies (From left, $\omega_n = 0.334$, $\omega_n = 0.379$, and $\omega_n = 0.436$). 22

2.7 Geometry of a PhC slab. 24

3.1 (a) PhC composed of a square Si lattice embedded in a waveguide bend. The square inset is the Brillouin zone of the PhC. Source and detector lines are described in the text. (b) Efficiency (i.e., power that crosses a given detector line divided by the incident power launched at the waveguide mode source) as a function of wavelength. 31

3.2 Image plot (λ = 1.55μm) of the magnitude squared of the time-average electric field calculated with 2-D FDTD. Yi cell size: 12 nm (λ/130). 32

3.3 (a) Band diagram for the PhC lattice. (b) Wave vector diagram for three cases: λ= 1.55μm (middle), λ= 1.74μm (right), and λ = 1.24μm (left). The solid arrows denote the primary wave vector of the guided mode incidents on the PhC interface. The dashed arrows along the horizontal axis are corresponding to the grating vectors from the periodicity of the boundary layer. The dotted arrows are the wave vectors of possible propagation modes by the reflection, refraction, and diffraction from the PhC interface. The inset shows the first Brillouin zone to aid comparison to the PhC orientation in Figure 3.1(a). 34

3.4 Image plots of 2-D FDTD simulation results for sources with wavelengths of 1.74μm (left) and 1.24μm (right), respectively. In both cases the Yi cell size is 10 nm. 35

3.5 (a) Geometry for beamsplitter. (b) Simulation results for the efficiency as a function of wavelength with which incident light is directed into the horizontal (—) and vertical (- - - -) waveguides for 1 layer of posts (*a* = 300 nm, r = 80 nm) and the horizontal (··········) and vertical (– – · – –) waveguides for 2 layers of posts (*a* = 300 nm, r = 83 nm). 37

3.6 Geometry and simulation result for Mach-Zender interferometer (λ=1.55μm). The horizontal and vertical center-to-center waveguide spacing in the interferometer is 9μm. Yi cell size: 12.9 nm (λ /120). 38

4.1 (a) The geometry for a polarizing beam splitter composed of a square array of Si posts embedded in waveguides. Waveguide mode source line and detector lines for efficiency calculations are indicated. The square inset is the Brillouin zone of the PhC. (b) Efficiencies as a function of wavelength for the TE and TM polarized incident light calculated at the detectors on the vertical and horizontal output waveguides as indicated in (a). 40

4.2 Magnitude squared time averaged (a) electric field (TM) and (b) magnetic field (TE) at λ= 1.55μm calculated by 2-D FDTD. The Yee cell size in the FDTD simulation is 10nm. 42

4.3 Wave vector diagrams for polarizing beam splitter at λ=1.55μm. The diamond insets indicate the first Brillouin zone with respect to the wave vector diagram. (a) TM and (b) TE. 44

4.4 Tolerance simulation results as a function of wavelength for variation in (a) Si posts radius (design parameter 86.8 nm), (b) Si posts period (design parameter 0.38 μm). 45

4.5 Tolerance simulation results as a function of wavelength for variation in (a) PhC region shift along the y axis (the inset is for the shift along the x axis; the design parameter is indicated as 0 offset), and (b) angle of the PhC surface with respect to the input waveguide. 47

5.1 (a) Dispersion relation of a PhC composed of a triangular air (n=1.000) hole array in the waveguide material (assumed to be a quasi-homogeneous material with effective index of waveguide, n=3.239) for r/*a* = 0.4. (b) Geometry of the hybrid PhC/CWG structure 51

5.2 (a) FDTD simulation result of magnitude squared time averaged magnetic field at λ=1.55μm (Yee cell size : 15nm). (b) Wave vector diagram corresponding to the hybrid structure. Inset indicates the Brillouin zone of the triangular lattice PhC. The grating wave vector is calculated as 2π/*a* (in which *a* is the period of PhC lattice) and is oriented in the direction of the boundary of the PhC.....................................53

5.3 (a) Bend efficiency comparison between the structures before and after optimization. (b) Optimized hybrid structure and magnitude squared time averaged magnetic field for λ=1.55μm. 55

5.4 (a) Band diagram for the PhC region of hybrid structure. (b) Geometry of hybrid PhC/CWG bend for high refractive index waveguide and a PhC composed of a square array air hole lattice. A detector is used to calculate the bending efficiency. The diamond inset is the Brillouin zone of the PhC. 57

5.5 (a) Magnitude squared time averaged electric field for TM polarized light for λ=1.55μm. (b) Corresponding wave vector diagram. Two solid arrows indicate the incident light and light reflected into the output waveguide. The dashed arrow indicates the grating vector for the periodicity of the first layer of the PhC. The dotted arrows denote the diffracted light. The inset shows the orientation of the Brillouin zone with respect to the wavevector diagram. See Figure 5.4(a) for how this relates to the bend structure orientation. 58

5.6 Efficiencies as a function of wavelength for the initial structure (dotted line), μGA optimized structure (dashed line), and manually adjusted structure (solid line) with removal of 75nm minimum wall size limitation. 60

5.7 μGA-optimized hybrid structure for high index waveguide and simulation result for λ=1.55μm 61

5.8 (a) Geometry of high efficiency beam splitter for high refractive index and low index contrast waveguide (For TM polarization). Detector positions to calculate the efficiencies at the horizontal and vertical output waveguides are indicated. (b) The efficiencies at the horizontal and vertical output waveguides as a function of wavelength. 62

5.9 (a) High efficiency beam splitter geometry for TE polarization with input waveguide mode source line and detectors for calculating efficiencies at both output waveguides. (b) Spectral responses for the geometry shown in Figure 5.9(a) at both horizontal and vertical output waveguides. 63

6.1 (a) The base hybrid structure. White arrows in the input and output waveguides indicate light propagation directions. (b) Dispersion relation for r/*a*=0.4, air hole array (n=1.000) in quasi-homogeneous medium (n_{eff}=1.451, which is the effective index of waveguide mode) for TM polarization...67

6.2 (a) Magnitude squared time averaged electric field calculated by 2-D FDTD for the structure shown in Figure 6.1(a) at λ= 1.55µm. (b) Corresponding wave vector diagram for the base structure. The diamond inset indicates the Brillouin zone of the PhC.................................69

6.3 Bend efficiency as a function of wavelength for the initial structure (dashed line) and the structure after the optimization process (solid line) 71

6.4 Magnitude squared time averaged electric field at λ=1.55μm for the final optimized geometry. 72

6.5 Geometry of the hybrid 90 degree waveguide bend for the Waveguide 1 before the μGA optimization. 73

6.6 Magnitude squared time averaged electric field for structures (a) before and (b) after optimization. 74

6.7 Spectral responses for the structures of before and after the optimization 75

6.8 Magnitude squared time averaged electric field for λ= 1.33μm with geometry of hybrid PhC and polymer waveguide structure (a) before and (b) after μGA optimization. The radii of air holes for the PhC and boundary layer are increased to 190nm and 221nm after the optimization. The boundary layer is shifted 988nm to negative Y direction. 76

6.9 Spectral responses for structures before (dashed line) and after (solid line) optimization. 77

7.1 Hybrid PhC and CWG structures for (a) a high efficiency 90 degree bend and (b) a high efficiency beam splitter. Square inset in Figure 7.1(a) indicate the Brilluin zone of the PhC. 82

7.2 Efficiencies as a function of wavelength for TM polarization. Solid line indicates the bend efficiency of the hybrid structure while the other two lines correspond to the efficiencies at channels of the splitter. 83

7.3 Geometry for the base ring resonator constructed with hybrid PhC and CWG structures. To maximize the efficiency, the throughput port is shifted 120nm to left and the waveguide in the middle of two splitters is shifted 120nm up. 84

7.4 Spectral responses of the base ring resonator at the drop (solid line) and throughput (dashed line) ports. 85

7.5 Time snap shot of the electric field at the drop wavelength. The computation is done by 4 CPUs with the parallelized 2-D FDTD. Yee cell size: 15nm and time step: 500,000. 86

7.6 Ring resonator geometry which occupies 35μm x 35μm to increase the FSR. 88

7.7 Spectral responses for the ring resonator which occupies 35μm x 35μm (dotted curve) compared with the base ring resonator structure (solid curve). 89

7.8 (a) The double Si posts array splitter structures with 100nm Si post radius and (b) spectral responses of all single and double Si posts array splitters as a function of wavelength. Solid line corresponds to the single Si posts array splitter and dashed and dotted lines are for the double Si posts array splitters with 95nm and 100 nm Si posts radii, respectively. 90

7.9 The efficiencies at the drop port of the ring resonators using single Si posts array splitter (solid line), double Si posts array splitter with 95nm radius (dashed line) and 100 nm radius (dotted line). 91

A.1 Geometry of ring resonator for an analysis. 100

LIST OF SYMBOLS

Symbol	Definition
a	Period of periodic structure
$\overline{b}$	Primitive reciprocal lattice vector
$\overline{B}$	Magnetic induction field vector
c	Speed of light
d	Overall propagation distance in the ring resonator
$\overline{d}$	Lattice vector of a translational symmetry system
$\overline{D}$	Displacement field vector
$\overline{E}$	Electric field vector
$\lvert \overline{E}_0 \rvert$	Input field amplitude of the ring resonator
E_c, E_f, E_s	Amplitudes of E_y at the waveguide upper clad, core, and substrate
E_x, E_y, E_z	Electric field components for each rectangular coordinate
$\overline{E}_{drop}$	Electric field vector at the drop port of the ring resonator
$\overline{E}_{inc}$	Incident electric field vector
$\overline{G_m}$	Reciprocal lattice vectors
h_m	Basis coefficient of function u
$\overline{H}$	Magnetic field vector
H_x, H_y,, H_z	Magnetic field components for each rectangular coordinate
$\overline{k}$	Reciprocal lattice vector

n	Refractive index of material
n_c, n_f, n_s	Refractive indices of waveguide upper clad, core, and substrate
N	Effective index of waveguide mode
r	Post or hole radius of periodic material for a photonic crystal
r_{b1}, r_{b2}	Reflection coefficient of hybrid 90 degree bend structure
r_{s1}, r_{s2}	Reflection coefficient along the channel 2 of hybrid splitter
$\bar{r}$	Radial distance vector
R_b	90 degree bend efficiency
R_s	Efficiency along the channel 2 of the splitter
s	Separation between two splitters in the ring resonator
t	Time variable
t_{s1}, t_{s2}	Transmission coefficient along the channel 1 of hybrid splitter
T	Waveguide thickness
T_s	Efficiency along the channel 1 of the splitter
$T\{\}$	Translation operator
TM	Transverse magnetic field polarization mode
TE	Transverse electric field polarization mode
u	Periodic function in a certain direction
x	Rectangular coordinate axis (x-axis)
y	Rectangular coordinate axis (y-axis)
z	Rectangular coordinate axis (z-axis)
β	Propagation constant of light
β_x	Propagation constant in the x direction

β_0	Free space propagation constant
θ	Incidence angle of wave
θ_0	Input field phase of the ring resonator
θ_{b1}, θ_{b2},	Phase delays at the hybrid 90 degree waveguide bend
θ_c	Critical angle
θ_{sr1}, θ_{sr2}, θ_{st1}, θ_{st2}	Phase delays at the hybrid splitter structures
ε	Relative dielectric constant
ε_0	Permittivity of free space
λ	Wavelength
λ_0	Free space wavelength
μ_0	Permeability of free space
π	Physical constant pi
ω	Angular frequency
ω_n	Normalized frequency
Δ	Refractive index contrast
Δt	Sampling time interval of FDTD
Δx	Sampling step of FDTD in x-direction
Δz	Sampling step of FDTD in z-direction
Γ, X, M	Critical points comprising irreducible Brillouin zone
δ	Phase term defined by $\delta = \theta_0 + \theta_{st1} + \theta_{st2} + ka$
ϕ	Phase term defined by $\phi = \theta_{b1} + \theta_{b2} + \theta_{sb1} + \theta_{sb2} + 2\pi Nd/\lambda_0$

Chapter 1

INTRODUCTION

1.1 Motivation

In order to lower costs and increase functionality in a smaller footprint, there is a need for higher levels of integration in planar lightwave circuits (PLCs). Conventional waveguide (CWG) structures are attractive platforms for PLC designs with advantages, such as low propagation loss, low coupling loss to and from optical fiber, and low dispersion. Using those advantages, many efforts have been made to realize CWGs based PLCs [1],[2],[3]. However those CWGs require a large radius of curvature (mm to cm for typical low index contrast waveguide structures) to achieve high efficiency bend [4]. Such large radius of curvature of CWGs limits the possible integration level of CWG devices in PLCs. Although there have been many efforts to achieve high efficiency waveguide bends within a small area, successful approaches have not yet been reported [5],[6],[7],[8],[9].

Since the concept of photonic crystal (PhC) structures was introduced by Dr. Yablonovitch in 1987 [10], they have been the focus of intense research in recent years [11] in part because of their potential to realize ultracompact PLCs. Two-dimensional (2-D) PhCs implemented in an index guiding slab that confines light vertically within the slab through total internal reflection (TIR) have received particular attention [12],[13],[14],[15],[16],[17],[18],[19],[20],[21],[22],[23],[24],[25],[26],[27],[28],[29],[30],[31], [32],[33],[34] owing to their relative ease of fabrication compared to 3-D PhCs. Much of the work reported in the literature on PhC slab structures has focused on creating fundamental elements of PLCs such as waveguides, bends, splitters, and resonators [35],[36]. The common theme for the vast majority of this work is to implement these functions with a 2-D PhC containing suitable lattice defects such that light is confined laterally by the photonic bandgap (forbidden frequency range in PhC) of the periodic structure. For this approach, issues such as scattering loss [29],[30],[31], relationship of defect waveguide modes to the light line [18],[32],[33], single mode versus multimode waveguide operation [16],[18],[21], and flatness of the dispersion relation of the fundamental guided mode [24] are problematic and require careful design consideration.

This dissertation is focused on hybrid photonic crystal and conventional waveguide structures [37],[38],[39],[40],[41]. Hybrid PhC and CWG structures take advantage of the attractive properties of both PhCs and CWGs. The PhC portion of a hybrid structure is used to manipulate the light propagation direction within a small area while CWGs are used for low loss propagation. In this dissertation, I will show how high efficiency waveguide bends and splitters [37],[38],[40],[41], polarizing beam splitter [39], Mach Zender interferometer [37], and ring resonators can be realized with such structures.

1.2 Overview of the dissertation

The light guiding mechanism in CWGs by the phenomenon of TIR is briefly covered in Chapter 2. Then, the basic concepts of PhC structures are followed. The photonic bandgaps of a PhC calculated by the plane wave expansion method and 2-D finite different time domain (FDTD) method [42] are presented. The 2-D FDTD simulation results of PhC waveguides created by removing a line of periodic material are also presented here. Brief descriptions for the numerical calculation tools are summarized at the end of the chapter.

As a first example of hybrid PhC and CWG structures, a single mode low refractive index waveguide structure with low index contrast between core and clad is considered in Chapter 3 [37],[41]. In order to achieve the high efficiency 90 degree waveguide bend for TM polarized light (out of plane electric field) within a small area, a silicon (Si) posts PhC region is integrated at the waveguide bend corner. The core of the waveguide has 2μm width and its refractive index is 1.5. The cladding refractive index is 1.465. The refractive index of Si posts is 3.481. High efficiency ultracompact 90 degree bend structure and splitter are successfully designed. By combining those bends and splitters, a compact and high efficiency Mach-Zender interferometer (within the area of 18 μm x 18 μm) is constructed and presented in this chapter.

An ultracompact high efficiency polarizing beam splitter that operates over a wide wavelength range based on a hybrid PhC and CWG structure is presented in Chapter 4 [39]. The CWG and PhC structures for this polarizing beam splitter are the same as the structures of the high efficiency 90 degree bend hybrid structure in Chapter 3. Within a small area (15 μm X 10 μm), this polarizing beam splitter separates TM and TE (in plane electric field) polarized modes into two different orthogonal output waveguides. The tolerance simulation results presented at the end of the chapter show the wide tolerance ranges for possible fabrication errors.

In Chapter 5, high efficiency ultracompact 90 degree bends and splitters with high refractive index waveguides with low index contrast and air hole PhC structures are presented [38]. The waveguide core width is still 2μm and the core and clad refractive indices are 3.25 and 3.2, respectively. In the case of a 90 degree bend, the periodicity of the PhC boundary in conjunction with the high index of the core and clad regions give rise to diffraction that limits the maximum optical efficiency of the bend. This can be overcome by changing the PhC region to suppress this diffraction. Structures are modified to maximize the bend efficiencies with the aid of a rigorous design tool that has been developed by Dr. Jianhua Jiang [43],[44], which consists of a micro genetic algorithm (μGA) for optimization combined with a 2-D FDTD method for rigorous electromagnetic computation of candidate structure properties.

In Chapter 6, an air hole PhC region is used to achieve a high efficiency 90 degree bend for a single mode silica waveguide (Δ=0.75%) which has a wider core (6μm) than the previously used waveguides [40]. The effective 2-D core and cladding refractive indices used for 2-D FDTD calculations are 1.453 and 1.445, respectively. A μGA is used to optimize hybrid PhC and CWG structures again in order to suppress diffraction. After the optimization, the bend efficiency is significantly improved (99.4% for λ=1.55μm) compared with the efficiency of the structure before the optimization. With the same approach, hybrid PhC and CWG structures of ultracompact high efficiency bends for two different polymer waveguide structures with air hole PhC regions are designed. One of polymer waveguides considered has core and cladding refractive indices of 1.486 and 1.477 (core width 4.0μm) while another has core refractive index of 1.630 and cladding refractive index of 1.625 (core width 3.5μm). The air hole PhC region and boundary layer for each polymer waveguide structure have been optimized with μGA at the wavelength of either 1.55μm or 1.33μm to suppress diffraction. Bend efficiencies are improved significantly after the optimization.

By combining the hybrid PhC and CWG structures of 90 degree bend structure and splitter with low refractive index waveguide, a ring resonator is realized and presented in Chapter 7. The waveguide structure used in Chapter 3 (n_{core}=1.5, n_{clad}=1.465, and 2μm core width) is considered again. The PhC region is composed of the Si posts array (n_{Si}=3.481). A base ring resonator which is used for further modification is constructed within 35μm X 50μm area and showed high drop efficiency (92.7%). In order to show the wide design freedom of this ring resonator configuration, the base ring resonator has been modified to have large FSR (19.8nm) and Q factor (1600).

The summary of accomplishments made in this dissertation is covered in Chapter 8 with some future research recommendations.

1.3 New contributions

Major new work that is presented in this dissertation includes the following:

1. A novel concept of hybrid PhC and CWG structures is proposed to realize ultracompact PLCs.
2. The phenomena associated with hybrid PhC and CWG structures are explained by use of wave vector diagram.

3. A method to suppress undesired diffraction from hybrid structures in order to maximize bend efficiencies is developed.
4. Various hybrid structures to achieve bends, splitters, and polarizing beam splitter for different waveguide structures are investigated.
5. A new method of realizing ring resonator structures which are useful for many compact integrated PLCs, such as add/drop filters, band pass filters, wavelength division multi-/demultiplexers, and all optical switches, is proposed.

Chapter 2

BACKGROUND

The basic idea of conventional waveguide structures (CWGs) is briefly covered in this chapter, since details can be found in literatures. The concept of PhC is discussed in some detail with explanation about PhC defect modes, PhC slabs, and issues on PhC slabs. Brief descriptions of the computational tools used throughout the work are followed at the end of this chapter.

2.1 Conventional waveguides

2.1.1 Review of conventional waveguides

When light is incident upon a boundary of different materials which have different refractive indices, part of the light will propagate through the boundary with an angle and other parts of the light will be reflected back. If light propagates from a higher refractive index material to a lower refractive index material with an angle greater than the critical angle, light can be completely reflected back from the boundary by the phenomenon of total internal reflection (TIR). A conventional waveguide (CWG) has a sandwich structure of different materials. A higher refractive index material is placed in between lower refractive index materials. This higher refractive index region is called the core region and lower index regions are called the cladding or substrate regions. If the angles of incident light are greater than the critical angles on both boundaries of the sandwiched structure, light is trapped in the core region by TIR and can be guided along the waveguide [2].

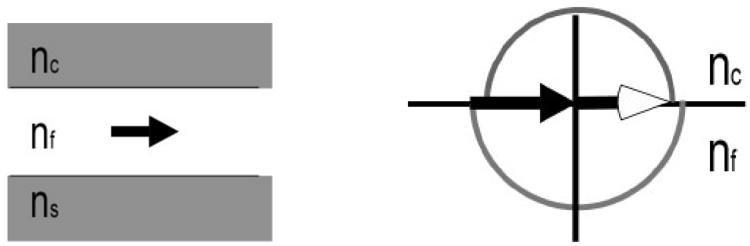

(a)

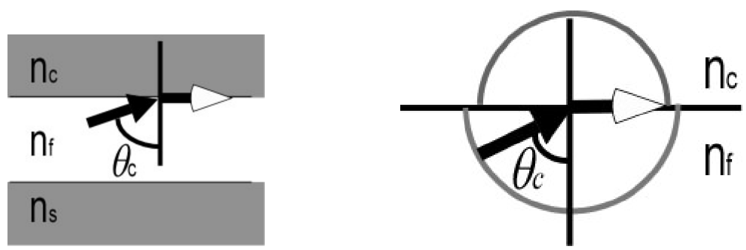

(b)

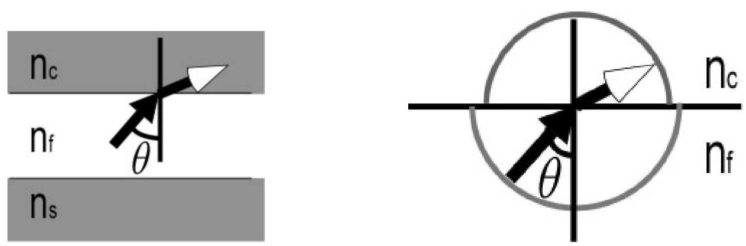

(c)

Figure 2.1. Geometrical interpretations of a waveguide and its wave vector space analyses for three different light propagation angles. There is a possible mode in the cladding region when light propagates with angle smaller than critical angle.

It is useful to use wave vector space analysis because light propagation characteristics can be illustrated easily in wave vector space. A CWG and its wave vector space analyses for different light propagation angles are shown in Figure 2.1. The arrows in Figure 2.1 indicate the light propagation directions. Figure 2.1(a) shows that the incident light with the 90 degree angle at the boundary of the core and cladding region is guided along the core region. Figure 2.1(b) shows the light propagation with the critical angle (θ_c) at the interface between core and upper cladding region while the light propagation with an angle smaller than the critical angle is presented in Figure 2.1(c). Since there is a possible propagation mode in the upper cladding region for the case shown in Figure 2.1(c), light is not trapped in the core region of the waveguide and cannot be guided. The electromagnetic fields of light from reflections at the upper and lower boundaries of the waveguide core interfere with one another. For constructive interference among them, light can be guided along the waveguide with a propagation mode.

Waveguide modes can be described in detail with the electromagnetic expressions [2]. Let's suppose that a plane wave propagates along the z direction, which is along the waveguide direction with the propagation constant of β. The electromagnetic fields vary as

$$\overline{E}(\overline{r},t) = \overline{E}(x,y)\exp j(\omega t - \beta z), \text{ and } \overline{H}(\overline{r},t) = \overline{H}(x,y)\exp j(\omega t - \beta z), \tag{2.1}$$

where the angular frequency $\omega = 2\pi c/\lambda$, and c is the velocity of light in free space ($c = 1/\sqrt{\varepsilon_0 \mu_0}$).

Depending on the polarization state of light, modes can be distinguished as TE and TM. A TE mode has one magnetic field component which is pointed out of the propagation plane and two electric field components which are within the plane. TM polarized light has one electric field component which is pointed out of the plane and two magnetic field components which are within the plane. The wave equations (with X-Z propagation plane) for the TE mode are

$$\frac{\partial^2 H_y}{\partial x^2} + (\beta_0^2 n^2 - \beta^2) H_y = 0, \tag{2.2}$$

$$E_x = \frac{\beta}{\omega \varepsilon_0 n^2} H_y, \tag{2.3}$$

$$E_z = \frac{1}{j\omega \varepsilon_0 n^2} \frac{\partial H_y}{\partial x}, \tag{2.4}$$

and the wave equations for the TM mode are

$$\frac{\partial^2 E_y}{\partial x^2} + (\beta_0^2 n^2 - \beta^2) E_y = 0, \tag{2.5}$$

$$H_x = -\frac{\beta}{\omega \mu_0} E_y, \tag{2.6}$$

$$H_z = -\frac{1}{j\omega \mu_0} \frac{\partial E_y}{\partial x}, \tag{2.7}$$

where ε_0, μ_0 are the dielectric permittivity and magnetic permeability of free space. The wave propagation constant in free space is written as $\beta_0 = 2\pi / \lambda_0$ for wavelength in free space, λ_0 and *n* is the refractive index of material.

Let us consider the CWG structure and assume the boundary between the upper clad and the core is at X=0. The thickness of the waveguide is T. Then the boundary between the substrate and the core is at X=-T. The tangential components of the fields have to be continuous at the boundaries (boundary conditions). The field solution and the boundary conditions at the interfaces lead to eigenvalue equations that determine the propagation characteristics of the TE and TM modes.

Only the TM mode is discussed in here as an example because the same analysis can be made for the TE mode. The electromagnetic fields for the guided modes of CWGs can be expressed in three different regions including the upper cladding, core, and substrate regions. Fields of the waveguide mode at the cladding and the substrate regions decay as the fields are away from the boundary with the core region. The electric fields at every region have to satisfy Equations (2.5), (2.6), and (2.7).

$$E_y = E_C \exp(-\gamma_C x), \; x > 0 \quad \text{(In the upper cladding)}$$

$$E_y = E_f \cos(\beta_X x + \phi_C), \; -T < x < 0 \quad \text{(In the core)} \tag{2.8}$$

$$E_y = E_S \exp\{\gamma_S (x+T)\}, \; x < -T \quad \text{(In the substrate),}$$

where the propagation constants in the X direction are expressed in terms of the effective index $N = n_f \sin\theta$, the refractive index of core n_f, the refractive index of cladding n_C, and the refractive index of substrate n_S as follows:

$$\gamma_C = \beta_0 \sqrt{N^2 - n_C^2}, \beta_X = \beta_0 \sqrt{n_f^2 - N^2}, \gamma_S = \beta_0 \sqrt{N^2 - n_S^2} . \tag{2.9}$$

The boundary conditions that the tangential field components E_y and H_z are continuous at the interface X=0. This yield

$$E_C = E_f \cos\phi_C, \; \tan\phi_C = \gamma_C / \beta_X . \tag{2.10}$$

Similarly, at X=-T

$$E_S = E_f \cos(\beta_X T - \phi_C), \; \tan(\beta_X T - \phi_C) = \gamma_S / \beta_X . \tag{2.11}$$

Eliminating arbitrary coefficients in the preceding relations results in an eigenvalue equation

$$\beta_X T = (m+1)\pi - \tan^{-1}(\frac{\beta_X}{\gamma_S}) - \tan^{-1}(\frac{\beta_X}{\gamma_C}) , \tag{2.12}$$

where $m = 0, 1, 2$ ….. denotes the mode number.

In the multimode waveguides which support more than one guided mode for a given polarization, mode interference and undesired mode conversion due to small disturbances reduce waveguide device performance significantly [2]. By selecting proper thickness for given waveguide materials, a single mode waveguide can be obtained.

More detailed information which is not covered here can be found from other literature [1],[2],[3],[4].

2.1.2 Conventional waveguide issues

A key drawback of CWGs with low refractive index contrast, $\Delta = (n_{core}-n_{clad})/n_{core}$ for symmetric CWG structures, is the relatively large radius of curvature (on the order of multiple mm's to cm's [3]) required to achieve high efficiency waveguide bends. The waveguide bends are necessary to achieve densely integrated PLCs. Let us consider the propagating waveguide mode of a single mode waveguide bend as shown in Figure 2.2. As the propagating waveguide mode enters into a bend with a radius of curvature, R, the evanescent field in the cladding region cannot travel as quickly as the field in the core region along the bend. Therefore, the evanescent tail of the guided mode is separated from the guide at the bend and radiated into the cladding region. Since the guided mode lost its tail by the radiation at the bend, in order to keep its waveguide mode profile, the tail is continually resupplied from the remainder of the guided mode [4]. As a consequence, the guided mode loses part of its power. This is the radiation loss of a CWG bend.

As the radius of curvature R increases, this radiation loss is decreased. Thus, to minimize radiation loss of a CWG bend, R should be large which in turn limits the possible integration level of PLCs.

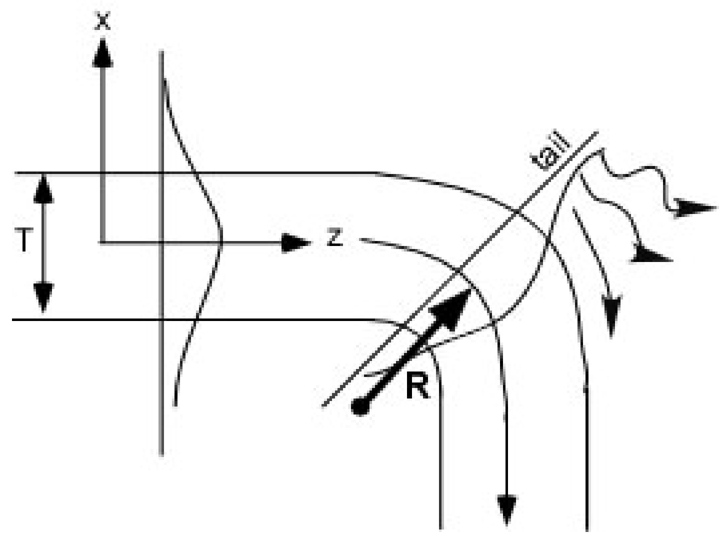

Figure 2.2. Waveguide bend geometry. T is the thickness of a single mode waveguide and R is the radius of curvature of the bend. This figure shows the power radiation from the outer tail side of waveguide mode by the waveguide bend [4].

To improve bend efficiency in a small area, many different approaches are proposed in literature [5],[6],[45],[7]. A waveguide bend structure with a core material which has a positive index response for the exposure to UV irradiation is proposed by R. A. Jarvis, *et al*. [6]. By exposing the waveguide bend region with UV irradiation, the core index is increased to suppress the bend loss. But this approach still requires 10mm radius of curvature to achieve a 0.5dB loss for a 90˚ bend. C. Manolatou, *et al.*[45] improved the 90 degree bend efficiency of the high index contrast waveguides up to 70% with 3% reflection from 30% bend efficiency with corner resonator structures. They had better results by cutting the corner of the resonator at 45 degrees with respect to the input waveguide. They reported 98.6% bend efficiency and very low reflection over a 240nm wavelength range centered at the 1.55μm wavelength. However, because of the high index contrast between core and clad, their core width is only 0.2μm which causes the problem of coupling between the fiber and waveguide. R. L. Espinola, *et al.* [7] showed a comparison between a resonant cavity structure and a corner mirror design for the high index contrast waveguide 90 degree bend. Their results show that the single corner mirror design without a resonator has a 97% bend efficiency over a 600nm wavelength range while a double mirror design has a 99% bend efficiency over a 200nm wavelength range centered at λ=1.55μm. However, since they worked with high index contrast waveguide design, their designs are also hindered by high coupling losses. C. T. Lee [5] proposed apexes-linked circle gratings at the bending region for improving the bend efficiency by phase compensation and avoiding distortion of the eigenmode of the waveguide. Their transmitted power efficiency was as high as 89% for a bending of up to 10^{o}.

2.2 Photonic Crystals (PhC)

2.2.1 Review of photonic crystals [46]

A PhC structure consists of a periodic array of dielectric material in a background dielectric material. Such periodic structure has forbidden propagation frequency ranges which are called photonic bandgaps. Depending on the dimensions of periodic array, 1-D, 2-D, and 3-D PhCs can be realized. A dielectric bragg mirror, which is well known for many different applications, is an example of 1-D PhC. In Figure 2.3, 1-D PhC structure created by alternating layers of two different materials (black bar and white background) is presented with 2-D PhCs composed of a square or triangular array of a dielectric material (black circles) embedded in a background material (white background). Dielectric materials (black and white) shown in Figure 2.3 are infinite in the third dimension.

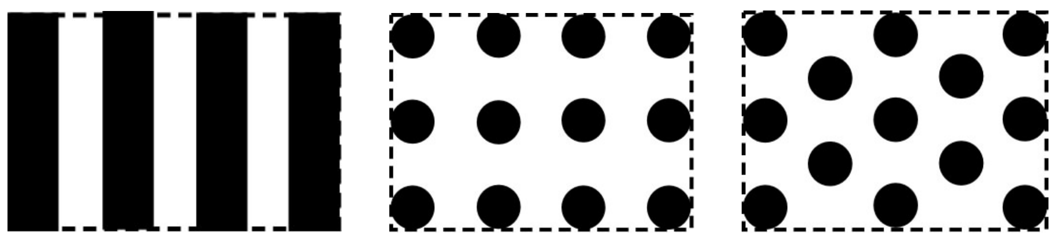

Figure 2.3. Basic 1-D (left) and 2-D PhC structures composed of a square (center) and triangular (right) periodic arrays.

Maxwell equations have been employed to analyze such periodic structures.

In MKS units,

$$\nabla \bullet \overline{B} = 0, \qquad \nabla \times \overline{E} + \frac{\partial \overline{B}}{\partial t} = 0, \qquad \nabla \bullet \overline{D} = 0, \qquad \nabla \times \overline{H} - \frac{\partial \overline{D}}{\partial t} = 0, \qquad (2.13)$$

where $\overline{E}$ and $\overline{H}$ are the electric and magnetic fields, $\overline{D}$ and $\overline{B}$ are the displacement and magnetic induction fields, and it is assumed that free charges and the electric current are absent.

For linear, lossless, and isotropic materials, the electric field and the displacement can be related by the relative dielectric constant $\varepsilon(\bar{r},\omega)$ and the dielectric constant of free space ε_0.

$$\bar{D}(\bar{r}) = \varepsilon_0 \varepsilon(\bar{r}) \bar{E}(\bar{r}) . \tag{2.14}$$

And for most dielectric materials of interest, one can assume that the magnetic permeability of the PhC is the same as that of free space, μ_0,

$$\bar{B} = \mu_0 \bar{H} . \tag{2.15}$$

By substituting Equation (2.14) and Equation (2.15) into Equation (2.13), the Maxwell equations become

$$\nabla \bullet \bar{H}(\bar{r},t) = 0 , \qquad \nabla \times \bar{E}(\bar{r},t) + \mu_0 \frac{\partial \bar{H}(\bar{r},t)}{\partial t} = 0 ,$$

$$\nabla \bullet \varepsilon(\bar{r}) \bar{E}(\bar{r},t) = 0 , \quad \nabla \times \bar{H}(\bar{r},t) - \varepsilon_0 \varepsilon(\bar{r}) \frac{\partial \bar{E}(\bar{r},t)}{\partial t} = 0 . \tag{2.16}$$

Since the Equation (2.16) contains linear equations and a complex valued field is employed for mathematical convenience, $\bar{E}$ and $\bar{H}$ can be written as harmonic modes and the time and spatial dependence of $\bar{E}$ and $\bar{H}$ can be separated.

$$\bar{H}(\bar{r},t) = \bar{H}(\bar{r}) e^{i\omega t} ,$$

$$\bar{E}(\bar{r},t) = \bar{E}(\bar{r}) e^{i\omega t} . \tag{2.17}$$

Two divergence and two curl equations can be obtained by substituting Equation (2.17) into Equation (2.16).

Two divergence equations are

$$\nabla \bullet \bar{H}(\bar{r}) = 0 , \qquad \nabla \bullet \varepsilon(\bar{r}) \bar{E}(\bar{r}) = 0 , \tag{2.18}$$

and two curl equations are

$$\nabla\times\overline{E}(\overline{r})+i\omega\mu_0\overline{H}(\overline{r})=0\,, \qquad \nabla\times\overline{H}(\overline{r})-i\omega\varepsilon_0\varepsilon(\overline{r})\overline{E}(\overline{r})=0\,. \tag{2.19}$$

From these two curl equations, the following equation can be obtained

$$\nabla\times(\frac{1}{\varepsilon(\overline{r})}\nabla\times\overline{H}(\overline{r}))=(\frac{\omega}{c})^2\,\overline{H}(\overline{r})\,, \tag{2.20}$$

where c is the velocity of light in free space ($c=1/\sqrt{\varepsilon_0\mu_0}$).

This is called the master equation [46].

By use of the master and divergence equations, $\overline{H}(\overline{r})$ can be completely determined.

For a PhC structure with a periodic dielectric material array, the electromagnetic modes have to satisfy not only the master and divergence equations but also a periodic condition. Because of the periodicity of a PhC structure, the PhC material system is unchanged for the translation along the direction of periodic array. This relation can be expressed as an equation,

$$T\{\varepsilon(\overline{r})\}=\varepsilon(\overline{r}+\overline{d})=\varepsilon(\overline{r})\,. \tag{2.21}$$

Such a system satisfying the Equation (2.21) is called a translational symmetry system and $\overline{d}$ denotes the lattice vector. Electromagnetic modes for a translational symmetry system can be written in a “Bloch form.”

$$T\{\overline{H}(\overline{r})\}=\overline{H}(\overline{r}+\overline{d})=\overline{H}(\overline{r})=e^{i2\pi}\,\overline{H}(\overline{r})\,. \tag{2.22}$$

This leads to the following electromagnetic mode expression:

$$\overline{H}(\overline{r})=e^{i\bar{k}\bullet\bar{r}}u(\overline{r})\,, \tag{2.23}$$

where $u(\overline{r})$ is a periodic function in a certain direction.

This implies

$$\overline{H}(\overline{r}+\overline{d}) = e^{i\overline{k}\bullet\overline{d}} e^{i\overline{k}\bullet\overline{r}} u(\overline{r}+\overline{d}) = e^{i\overline{k}\bullet\overline{r}} u(\overline{r}),$$

$$\overline{k}\bullet\overline{d} = 2\pi n \ \ (n = 0,\ 1,\ 2,\ \ldots\ldots). \tag{2.24}$$

The wave vectors $\overline{k}$ satisfying Equation (2.24) are called reciprocal lattice vectors. The lattice vectors $\overline{d}$ that translate the lattice of a structure into itself are expressed by

$$\overline{d} = la\hat{x} + ma\hat{y} + na\hat{z}, \tag{2.25}$$

where a is the period of a PhC array and l, m, n are integers.

And every reciprocal lattice vector can be written as

$$\overline{k} = l'\hat{b}_1 + m'\hat{b}_2 + n'\hat{b}_3, \tag{2.26}$$

where $\hat{b}$ s are called primitive reciprocal lattice vectors.

For $\overline{d}$ and $\overline{k}$ to satisfy the relationship in Equation (2.24), we have

$$(la\hat{x} + ma\hat{y} + na\hat{z})\bullet(l'\hat{b}_1 + m'\hat{b}_2 + n'\hat{b}) = 2\pi n. \tag{2.27}$$

The primitive reciprocal lattice vectors satisfying Equation (2.27) are

$$\hat{b}_1 = \frac{2\pi}{a}\frac{\hat{y}\times\hat{z}}{\hat{x}\bullet\hat{y}\times\hat{z}},$$

$$\hat{b}_2 = \frac{2\pi}{a}\frac{\hat{z}\times\hat{x}}{\hat{x}\bullet\hat{y}\times\hat{z}}, \tag{2.28}$$

$$\hat{b}_3 = \frac{2\pi}{a}\frac{\hat{x}\times\hat{y}}{\hat{x}\bullet\hat{y}\times\hat{z}}.$$

From Equation (2.28), reciprocal lattice vectors can be constructed based on primitive reciprocal lattice vectors in the reciprocal space.

The smallest size of the periodic structure in real space which holds translational symmetry for the lattice vector $\bar{d}$ is called the unit cell. In reciprocal space, the minimum region which will be duplicated for all over the structure by translational symmetry is called “Brillouin zone.” In Figure 2.4, a square lattice PhC in real space and corresponding Brillouin zone in reciprocal space are shown as an example. As seen in Figure 2.4, the triangle region comprised of Γ, X, and M in the Brillouin zone represents other sides of the zone by the rotation and reflection symmetries. This triangle region is called the irreducible Brillouin zone. Therefore the calculations for the wave vectors in the irreducible Brillouin zone are sufficient to find all electromagnetic modes of a PhC.

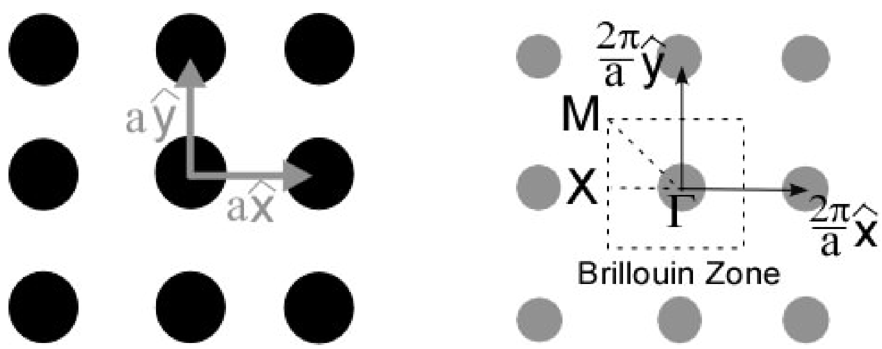

Figure 2.4. Geometry of a square lattice PhC (left) in real space and its counterpart in the reciprocal space (right). The Brillouin zone is indicated in the right figure.

Detailed theoretical methods and considerations to calculate PhC modes using the plane wave expansions are available in the literature [46],[47],[48]. The dispersion relation, PhC modes as a function of reciprocal lattice vector (same as the wave vector for a mode in the PhC), is useful to find photonic bandgap. Throughout this dissertation, the MIT Photonic-Bands (MPB) [46] is used to calculate dispersion relation of PhCs. MPB was developed by Dr. Steven G. Johnson of the Joannopoulos *Ab Initio* Physics Group in the Condensed Matter Theory division of the MIT Physics Department and is downloadable from their website. To rigorously calculate the power and field distributions of the PhC structures and their frequency spectrum, numerical codes based on the 2-D Finite Different Time Domain (FDTD) method [42] have been also used. These codes are developed by Dr. Jianhua Jiang and Mr. Jingbo Cai of the Nano and Micro Devices Laboratory (NMDL) at the University of Alabama in Huntsville. Numerical tools used in this work are briefly summarized in Section 2.3.

2.2.2 Photonic bandgap and PhC waveguide

In Figure 2.5, the dispersion relation and transmission spectrum of a square lattice PhC for TM polarization are shown with the geometry.

The normalized frequency used in Figure 2.5 is expressed by

$$\omega_n = \frac{\omega a}{2\pi c}, \tag{2.29}$$

where a is the lattice constant and c is speed of light in free space.

The normalized frequency range which has no possible wave vector along the Γ-X direction of the square lattice is found from the dispersion relation. This is the directional photonic bandgap along the Γ-X direction for a given geometry. This photonic bandgap is also distinguished from the transmission spectrum calculated by 2-D FDTD. For the photonic bandgap frequencies, the transmissions are zero for the plane wave incidence as shown in Figure 2.5.

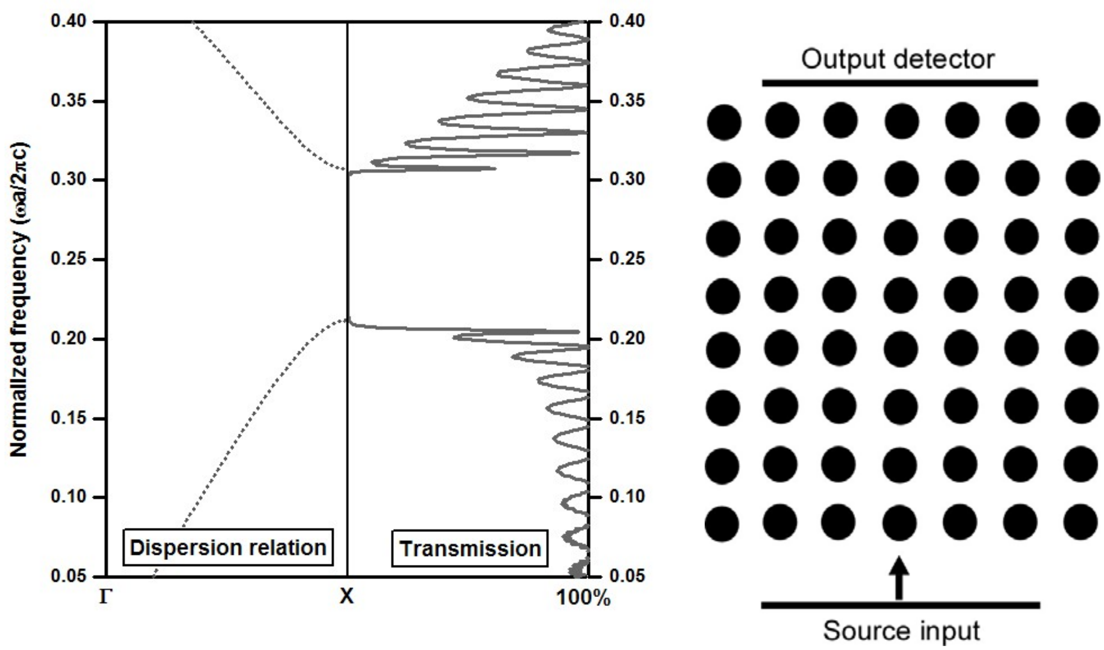

Figure 2.5. Photonic bandgap for TM polarization along the Γ-X direction of a square lattice PhC. Calculation results with MPB (dispersion relation) and 2-D FDTD (transmission) are presented with the geometry (right).

However, those frequencies in the photonic bandgap can have modes at the defects where the periodicity of the PhC is broken. As an example to show those modes in defects for the photonic bandgap frequencies, another square array PhC is designed and a line defect was created by removing a column of dielectric material along the light propagation direction. The PhC is composed of a square array of silicon (Si) posts (refractive index 3.4) in the air (refractive index 1.0) and its lattice constant and radius of the Si posts array are 0.34μm and 0.06μm, respectively.

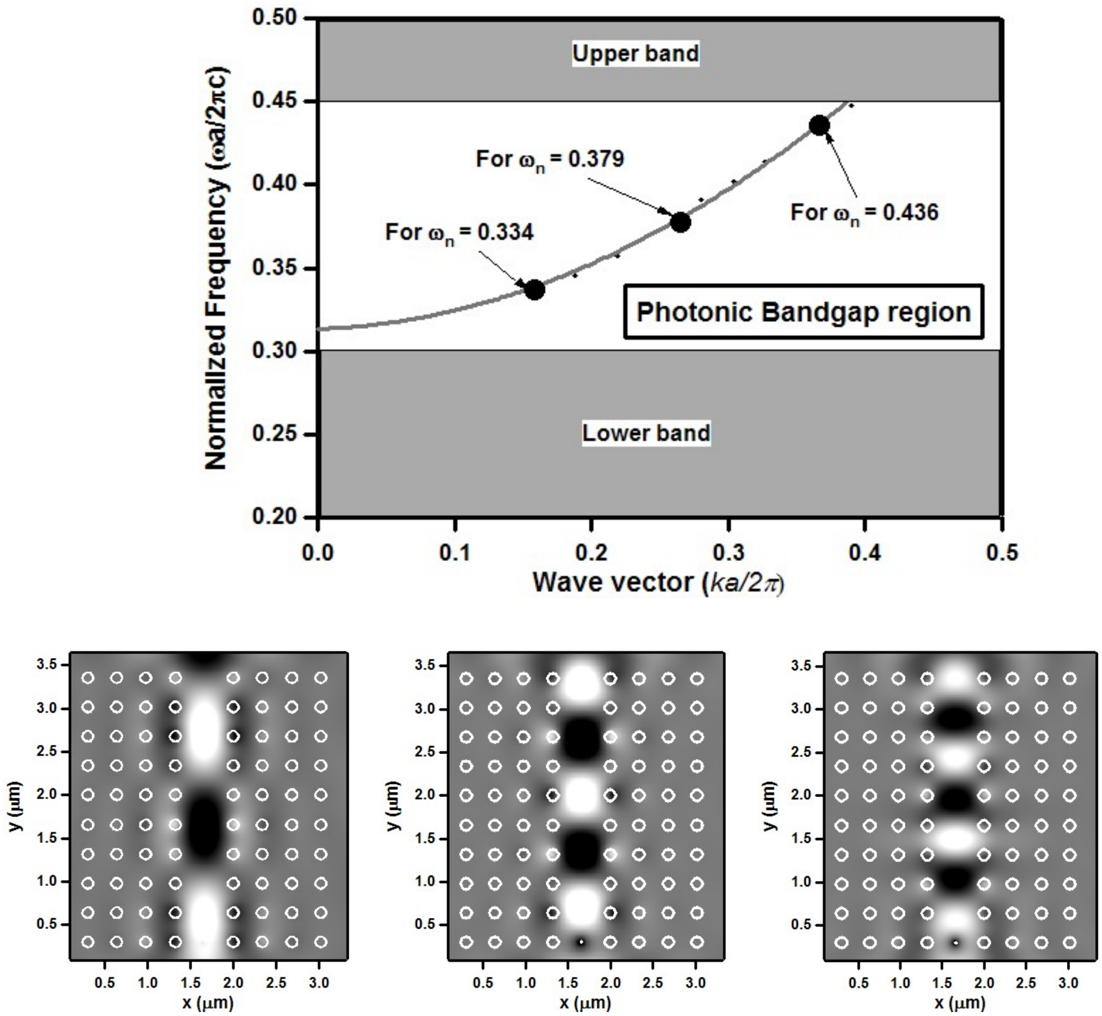

Figure 2.6. Dispersion relation showing the photonic bandgap and PhC waveguide mode (gray curve in the photonic bandgap region) for a square Si posts PhC and time snap shots of PhC waveguide modes for three different frequencies (From left, $\omega_n = 0.334$, $\omega_n = 0.379$, and $\omega_n = 0.436$).

In Figure 2.6, the dispersion relation calculated by MPB for the geometries with and without defects is shown. The normalized frequency in the range of 0.3 to 0.45 cannot have possible electromagnetic modes in the given PhC structure. However, with a line defect, those frequencies in the photonic bandgap have possible wave vectors along the defect which is shown as a curve in the photonic bandgap. Since there is no possible mode in the PhC region for the frequencies in the photonic bandgap, those are confined and guided along the defect region. Such a structure which guides frequencies only along the defect of the PhC is a PhC waveguide structure and those modes are called the PhC waveguide modes. To show the propagation of the PhC waveguide modes along the line defect, the time snap shots of electric fields for three different frequencies are calculated by 2-D FDTD with Berenger perfectly matched layer boundary conditions [49] and presented in Figure 2.6.

There have been many efforts to design defect PhC structures to achieve high efficiency waveguides [13],[14],[15],[16],[17],[18],[19],[20],[21],[29],[30],[31],[32],[33], bends [18],[22],[23],[24],[34], splitters [25],[26], and resonators [27],[28],[35],[36]. To realize realistic PhC devices, full 3-D PhCs have to be designed, analyzed, and fabricated. However, since fabricating 3-D periodic structure is not an easy task, PhC slabs which confine light within the slab through total internal reflection (TIR) have received particular attention [50].

2.2.3 Photonic crystal slab and problems

Figure 2.7 shows a PhC slab geometry, which has a finite height in the Y axis with periodic dielectric material array along the X-Z plane. A PhC slab defect waveguide can be realized by removing holes or posts along the light propagation direction as presented before. Modes of the PhC slab waveguide are confined not only by the PhC in the X-Z plane but also by the finite slab thickness in the Y direction [50]. Even though PhC slabs are attractive approaches to confine light in three dimensions, experimental and theoretical works indicate that propagation and out of plane scattering losses of PhC slab defect waveguides are high [30],[31],[32],[51].

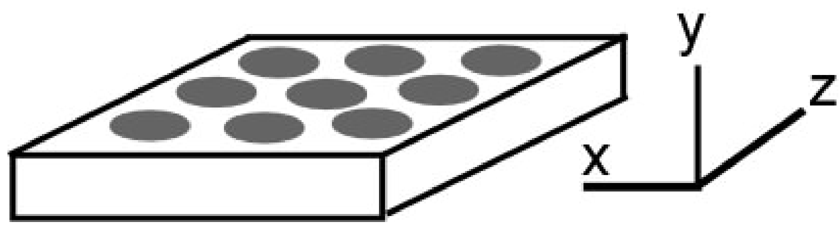

Figure 2.7. Geometry of a PhC slab.

Many efforts to analyze and improve the out of plane radiation losses have been made and reported [29],[30],[31]. However other problematic issues are associated from those proposed approaches, such as PhC slab waveguide modes above the light line [18],[32],[33] and single mode versus multimode waveguide operation [16],[18],[21].

2.3 Computational tools

Three major computational tools, MPB, 2-D FDTD, and μGA, are used throughout the work. In this section, I briefly cover basic information for those tools. Serious readers have to refer to the references.

2.3.1 MIT photonic-bands (MPB) [46]

The MPB solves the master equation and the divergence equation covered in Section 2.2.1. The PhC mode, which is a time harmonic mode and translationally invariant for a given periodicity, can be expressed by

$$\overline{H}(\bar{r},t)=e^{i(\bar{k}\bullet\bar{r}-\omega t)}u(\bar{r})\,. \tag{2.30}$$

And those PhC modes satisfy the master equation and the divergence equation

$$\nabla\times\frac{1}{\varepsilon(\bar{r})}\nabla\times\overline{H}(\bar{r},t)=-\frac{1}{c^2}\frac{\partial^2}{\partial t^2}\overline{H}(\bar{r},t)\quad,$$

$$\nabla\bullet\overline{H}(\bar{r},t)=0\,. \tag{2.31}$$

As Equation (2.30) is substituted into Equation (2.31), the following equation can be obtained:

$$(\nabla+i\bar{k})\times\frac{1}{\varepsilon(\bar{r})}(\nabla+i\bar{k})\times u(\bar{r})=(\frac{\omega}{c})^2u(\bar{r})\,. \tag{2.32}$$

$u(\bar{r})$ can be expanded by the planewave basis

$$u(\bar{r})=\sum_{m=1}^{N}h_m e^{i\overline{G}_m\bullet\bar{r}}\quad, \tag{2.33}$$

where h_m are the basis coefficients and $\overline{G}_m$ are some reciprocal lattice vectors.

By employing the planewave basis, the master equation forms an eigenvalue equation. MPB uses a Fast Fourier Transform (FFT) to solve the eigenvalue equation and determine the eigenfrequency ω and the basis coeffiecients h_m effectively. Other details can be found in Reference 46.

2.3.2 Finite difference time domain (FDTD) Method [42]

A FDTD method solves the following Maxwell curl equations numerically

$$\nabla\times\overline{E}(\bar{r},t)=-\frac{1}{c}\frac{\partial}{\partial t}\overline{H}(\bar{r},t)\quad,$$

$$\nabla\times\overline{H}(\bar{r},t)=\frac{\varepsilon(\bar{r})}{c}\frac{\partial\overline{E}(\bar{r},t)}{\partial t}. \tag{2.34}$$

The derivatives in the Maxwell equations are approximated to be calculated by finite differences and the electromagnetic field components located on a Yee cell [52]. For 2-D FDTD, the electric field components at time $n\Delta t$ are located on the sides of the Yee cell while the magnetic field components at times $(n+\frac{1}{2})\Delta t$ are located at the center of the Yee cell.

In this dissertation, the 2-D finite difference equations for the TM polarized case are presented. More details can be found in Reference 42.

For the TM polarization, only E_y, H_x, and H_z are involved and are governed by the time-dependent Maxwell's equations. The electric field component is pointed out of the horizontal plane and two magnetic field components are within the horizontal plane.

$$E_y\,|_{i,k}^{n+1} = E_y\,|_{i,k}^{n} + \frac{\Delta t}{\varepsilon_{i,k}}[(H_x\,|_{i,k+1/2}^{n+1/2} - H_x\,|_{i,k-1/2}^{n+1/2})/\Delta z$$

$$-(H_z\,|_{i+1/2,k}^{n+1/2} - H_z\,|_{i-1/2,k}^{n+1/2})/\Delta x], \tag{2.35}$$

$$H_x\,|_{i,k+1/2}^{n+1/2} = H_x\,|_{i,k+1/2}^{n-1/2} + \frac{\Delta t}{\mu\Delta z}[(E_y\,|_{i,k+1}^{n} - E_y\,|_{i,k}^{n}), \tag{2.36}$$

$$H_z\,|_{i+1/2,k}^{n+1/2} = H_x\,|_{i+1/2,k}^{n-1/2} + \frac{\Delta t}{\mu\Delta x}[(E_y\,|_{i+1,k}^{n} - E_y\,|_{i,k}^{n}). \tag{2.37}$$

E_y is computed in the FDTD grid area and stored in the computer memory for a particular time point using the H data previously stored in the computer memory. Then all of the H computations are completed and stored in the computer memory using the E_y data just computed. The cycle can begin with the re-calculation of the E_y based on the latest H. This process continues until the time-marching is finished. The 2-D FDTD codes used throughout this work were developed by Dr. Jianhua Jiang and Mr. Jingbo Cai of the Nano and Mirco Devices Laboratory (NMDL) in the University of Alabama in Huntsville. The Berenger Perfectly Matched Layer (PML) boundary condition [49] is employed for this 2-D FDTD codes. The codes have the capability to excite many different types of sources, such as pulsed and single frequency plane wave sources, gaussian wave sources, and waveguide mode sources.

2.3.3 Micro genetic algorithm (μGA) [53]

A micro genetic algorithm (μGA) is a genetic algorithm using a small population size (in our case usually 5). A μGA integrated with FDTD (μGA-FDTD) has been developed by Dr. Jianhua Jiang and used to optimize some hybrid PhC and CWG structures. The μGA optimized selected parameters to maximize the power at the detector for a certain frequency or a certain position calculated by 2-D FDTD.

Details about μGA-FDTD can be found from Reference 53.

2.4 Conclusions

In this chapter, the concepts and tools behind the work presented in this dissertation are introduced. The basic ideas of CWG and PhC, which are necessary to understand the work in this dissertation, are introduced. The problematic issues from CWG and PhC are covered which in turn supports the motivation of this work. The size limitation to achieve a high efficiency 90 degree CWG bend is the main issue of CWG applications for ultracompact PLCs. The high propagation and out of plane radiation losses of the PhC slab should be addressed in order so that PhC slab could be useful for many applications. The summaries of computational tools used in this dissertation are followed at the end.

Chapter 3

HYBRID PHC AND CWG STRUCTURES FOR A LOW REFRACTIVE INDEX WAVEGUIDE WITH A LOW INDEX CONTRAST

In this chapter hybrid PhC and CWG structures designed for low refractive index waveguides with low index contrast between core and clad are presented [37]. The PhC regions augment the CWGs to reduce overall device size while preserving the traditional advantages of CWGs. The potential of this approach has been demonstrated in this chapter by investigating high efficiency 90-degree bends and beam splitters, and, as an example, showing how these elements can be combined to form a very compact, high efficiency planar Mach-Zender interferometer.

3.1 Ultracompact high efficiency CWG bend structure

First let us consider the geometry shown in Figure 3.1(a) in which a small 2-D PhC region forms a 90-degree corner for a CWG. The CWG has core and clad refractive indices of n_1=1.500 and n_2=1.465, respectively, for a refractive index contrast (Δ) of 2.3%. (Note: since our analysis is 2-D in nature, these refractive indices are for 2-D waveguides. A similar approach may be taken to approximate 3-D channel waveguides if effective indices are used.) The CWG has a core width of 2 microns, so it supports a single guided mode for wavelengths in the telecommunication band near 1.55 μm. The

PhC lattice is composed of a square array of silicon (Si) posts (refractive index 3.481) with a lattice constant, *a*, of 380 nm and a post radius, r, of 86.8 nm.

A 2-D FDTD method [42] with Berenger perfectly matched layer boundary conditions [49] has been used to numerically calculate the optical properties of the structure shown in Figure 3.1(a). The fundamental waveguide mode is sourced along an 8 μm wide line centered on the input waveguide and directed toward the PhC region as indicated in the figure. The light is TM polarized (electric field orientation parallel to the posts). The field is monitored along 8 μm wide detector lines for light that is transmitted through the PhC region, reflected by the structure toward the input waveguide, and deflected into the output waveguide.

Figure 3.1(b) shows a plot as a function of wavelength of the fraction of the incident light that is deflected into the output waveguide (which is defined as bend efficiency), reflected back toward the input waveguide, and lost through the top of the PhC region. For wavelengths between 1.23 μm and 1.68 μm, very little light is lost through the PhC structure. Instead, most of it is either reflected back in the direction of the source or deflected into the output waveguide. Note that there is a broad wavelength region (~1.43 to 1.64 μm, $\Delta\lambda/\lambda$ = 13.5%) in which the bend efficiency is greater than 95%.

In Figure 3.2, the magnitude squared time averaged electric field is shown for a wavelength of 1.55 μm. The bend efficiency for this case is 98.7%, while only 0.14% of the incident light is reflected back in the direction of the input waveguide. The bend radius for a curved waveguide with the same bend efficiency is 2.5 mm. Insertion of the PhC region essentially introduces a high efficiency, mode-matched mirror into the waveguide to achieve a dramatic reduction in the area required to realize a 90-degree bend.

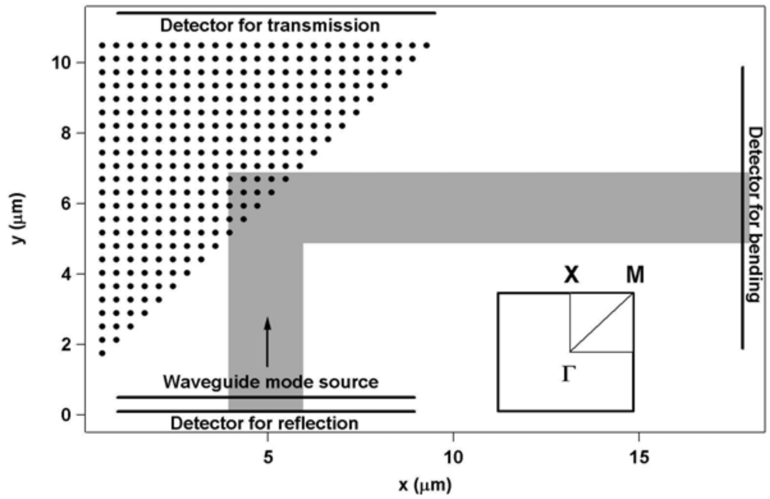

(a)

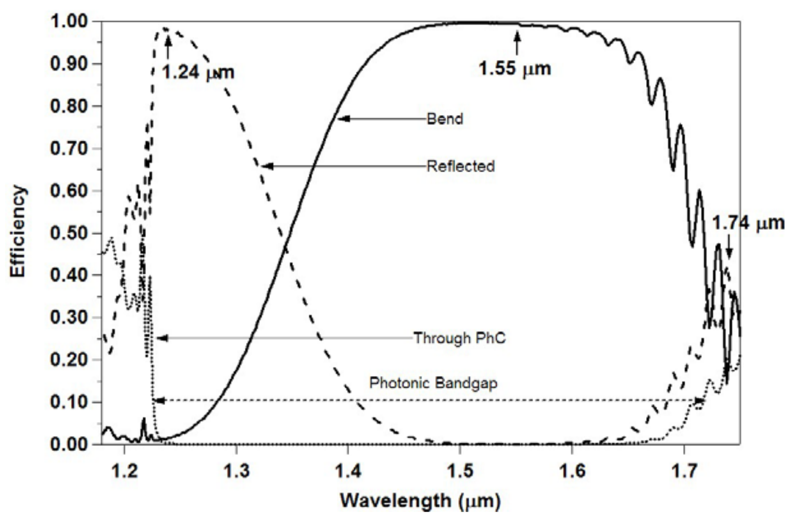

(b)

Figure 3.1. (a) PhC composed of a square Si lattice embedded in a waveguide bend. The square inset is the Brillouin zone of the PhC. Source and detector lines are described in the text. (b) Efficiency (i.e., power that crosses a given detector line divided by the incident power launched at the waveguide mode source) as a function of wavelength.

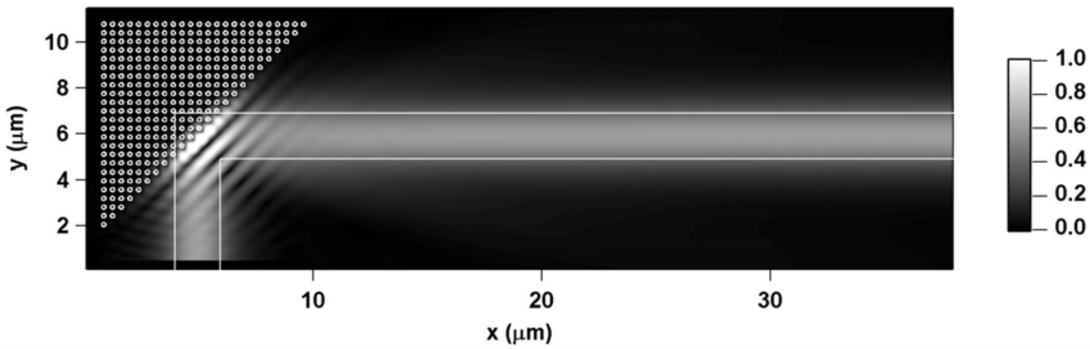

Figure 3.2. Image plot (λ = 1.55μm) of the magnitude squared of the time-average electric field calculated with 2-D FDTD. Yi cell size: 12 nm (λ/130).

An interesting feature of this result is illustrated in the band diagram for the PhC region, which is shown in Figure 3.3(a). Note that a wavelength of 1.55 μm (normalized frequency of 0.243) does not lie in the bandgap, but rather is just below it. However, as seen in Figure 3.2, light does not couple into a propagating mode of the PhC and instead is reflected with great efficiency into the output waveguide.

This can be understood by examination of the wave vector diagram [54],[55],[56] in Figure 3.3(b) in which the horizontal axes are the Γ-M direction, which coincides with the direction of the PhC surface that is at 45 degrees to the input and output waveguides. For all wavelengths, the semi circle indicates the allowed wave vectors in the core and clad regions (which CWG region is treated as homogeneous for simplicity in constructing the wave vector diagram), while the dotted curves denote the wave vectors for allowable propagation modes in the PhC region. For λ=1.55μm (middle in Figure 3.3(b)), note that for light incident from the input waveguide at 45 degrees to the PhC surface (solid arrow), there are no allowed states in the PhC that the light can couple into (i.e., the black dashed vertical line does not intersect the allowed PhC wave vector curves). Therefore it is not necessary that the PhC be designed such that the wavelengths of interest for device operation fall strictly within the photonic bandgap.

Alternatively, consider propagation at $\lambda = 1.75$ μm, which, from Figure 3.3(a), is considerably below the low frequency edge of the photonic bandgap. As shown in Figure 3.4, much of the light is coupled into the PhC structure. Referring to the wave vector curves (right side) in Figure 3.3(b), it is clear that the incident light (solid arrow) can directly couple into an allowed PhC propagating mode (dotted arrow). Moreover, the first diffraction order (with a wave vector component in the Γ-M direction given by the end of the dashed arrow) couples into a PhC propagating mode (dotted arrow) as well.

It is also useful to understand why such a large fraction of light within the bandgap in the 1.23 – 1.32 μm wavelength range is reflected toward the input waveguide rather than deflected into the output waveguide. From Figure 3.1(b), the peak reflection efficiency occurs at a wavelength of 1.24 μm. As seen in Figure 3.3(a), this wavelength is just below the high frequency edge of the bandgap. As shown in Figure 3.4, the reflected light is not directed exactly back along the input waveguide. The corresponding wave vector diagram is shown on the left side in Figure 3.3(b), in which there are no allowed propagating modes in the PhC. However, the first diffraction order (dotted arrow) is not evanescent, but propagates at an angle of 9 degrees relative to the input waveguide. This diffraction order contains most of optical power that is redirected by the PhC region. Thus the existence of allowed diffraction orders in the nearly homogeneous CWG areas due to diffraction from the periodic PhC interface is a critical design consideration when integrating limited PhC regions with CWGs.

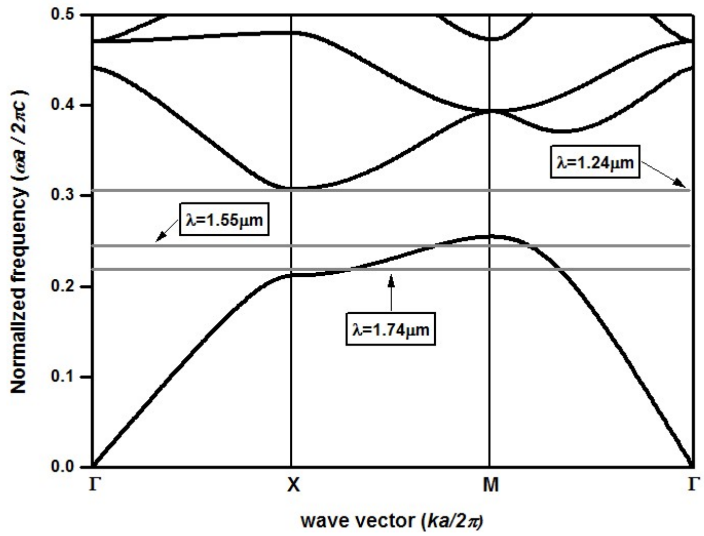

(a)

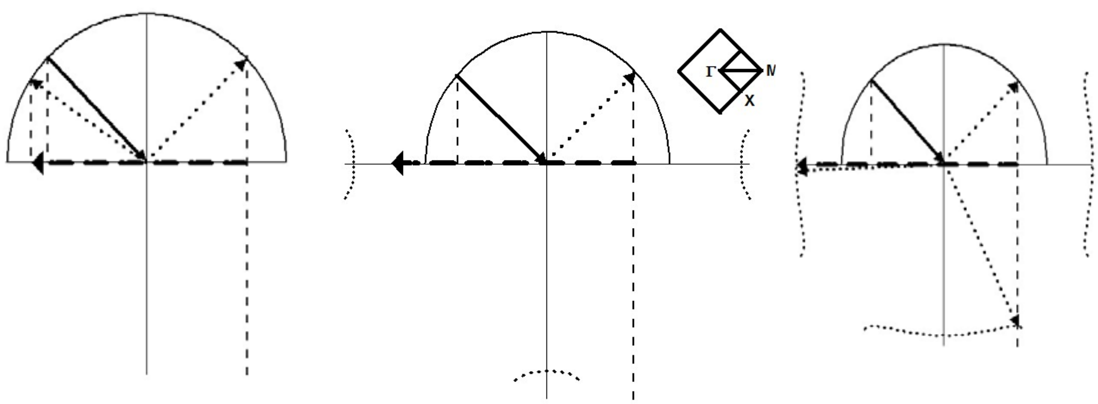

(b)

Figure 3.3. (a) Band diagram for the PhC lattice. (b) Wave vector diagram for three cases: λ= 1.55µm (middle), λ= 1.74µm (right), and λ = 1.24µm (left). The solid arrows denote the primary wave vector of the guided mode incidents on the PhC interface. The dashed arrows along the horizontal axis are corresponding to the grating vectors from the periodicity of the boundary layer. The dotted arrows are the wave vectors of possible propagation modes by the reflection, refraction, and diffraction from the PhC interface. The inset shows the first Brillouin zone to aid comparison to the PhC orientation in Figure 3.1(a).

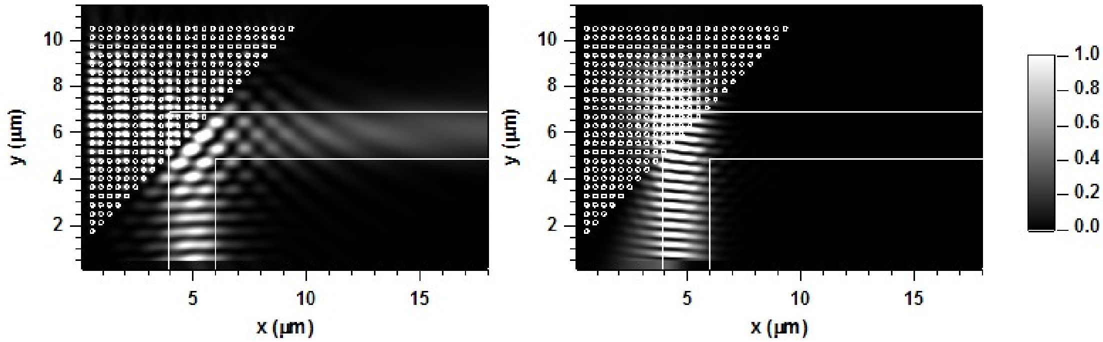

Figure 3.4. Image plots of 2-D FDTD simulation results for sources with wavelengths of 1.74μm (left) and 1.24μm (right), respectively. In both cases the Yi cell size is 10 nm.

3.2 High efficiency beamsplitter

Now let's consider beamsplitters. The basic geometry is shown in Figure 3.5(a) in which, as an example, two layers of a square lattice of Si posts cross a CWG intersection at 45 degrees.

Figure 3.5(b) shows the efficiency with which light is split into the two output ports as a function of wavelength for both single and double layers of Si posts. In each case the Si post arrays have been designed to yield equal splitting of the incident power into the two output waveguides aṭ a wavelength of 1.55 μm. For the single layer of posts, the fraction of the incident optical power directed into each waveguide is 49.7% (for 99.4% total efficiency) and only 0.012% is reflected back into the input waveguide. For the double layer of posts, 50.2% of the incident light is directed into the horizontal output waveguide, 49.2% into the vertical output waveguide (for, again, 99.4% total efficiency), and 0.05% is reflected. As one would expect, when the number of Si post layers is increased beyond two the total efficiency of directing light into the output waveguides rapidly decreases.

Also, as shown in Figure 3.5(b), the ratio of power split between the two output waveguides is less sensitive to wavelength for a single layer of Si posts. In essence, this structure is a subwavelength diffraction grating for which all of the diffraction orders are evanescent except the reflected and transmitted zero orders, and the grating structure is tuned to direct equal power into these two orders.

3.3 Mach-Zender interferometer using hybrid bends and beamsplitters

As shown in Figure 3.6, the single layer beamsplitter can be combined with the waveguide bend from Figure 3.1(a) to form a compact (18 μm x 18 μm), high efficiency, planar Mach-Zender interferometer. For the particular simulation result shown in the figure (λ = 1.55 μm), the fraction of the incident optical power that is directed into the horizontal output waveguide is 97.8%, while only 0.6% is coupled into the vertical output waveguide and 0.08% is reflected back into the input waveguide.

As one would expect, simulation results show that arbitrary power splitting between the two output waveguides occurs when the optical path lengths of the two interferometer legs are changed by small shifts in the position of the bend elements. If a phase modulator is introduced in one leg of the interferometer, the overall interferometer footprint will be limited by the phase modulator length (for phase modulators with refractive index modulation of $\sim 10^{-2}$ or less) rather than the size of the bend and beamsplitting regions.

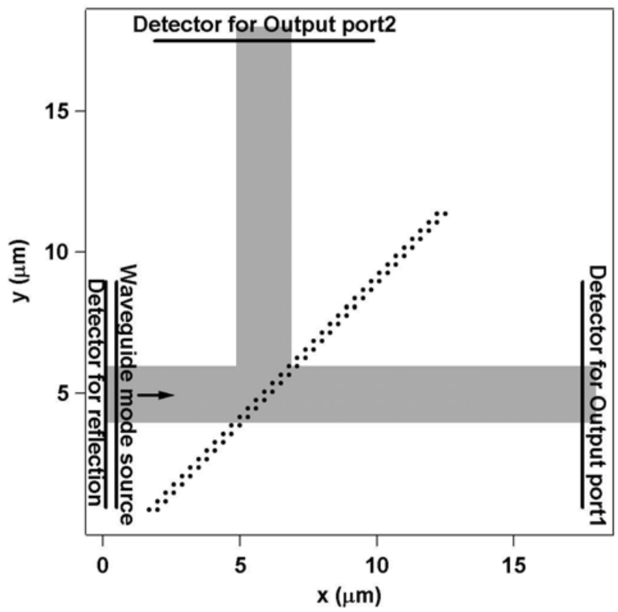

(a)

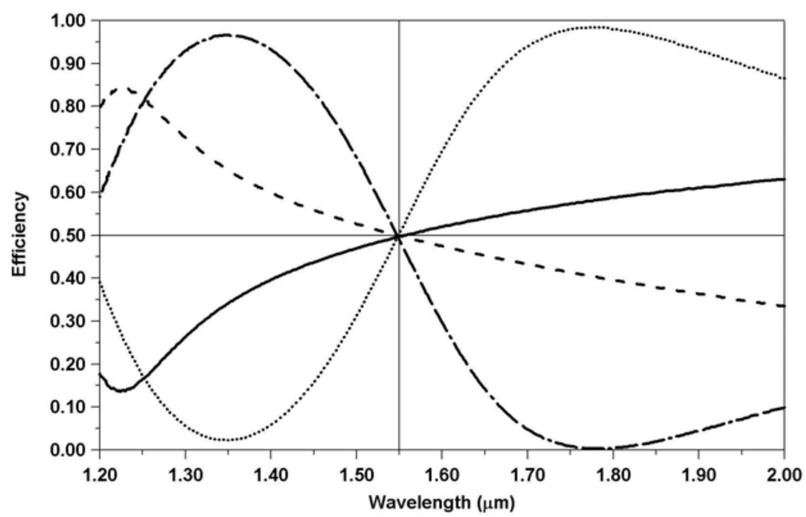

(b)

Figure 3.5. (a) Geometry for beamsplitter. (b) Simulation results for the efficiency as a function of wavelength with which incident light is directed into the horizontal (——) and vertical (- - - -) waveguides for 1 layer of posts (a = 300 nm, r = 80 nm) and the horizontal (··········) and vertical (–·–·–) waveguides for 2 layers of posts (a = 300 nm, r = 83 nm).

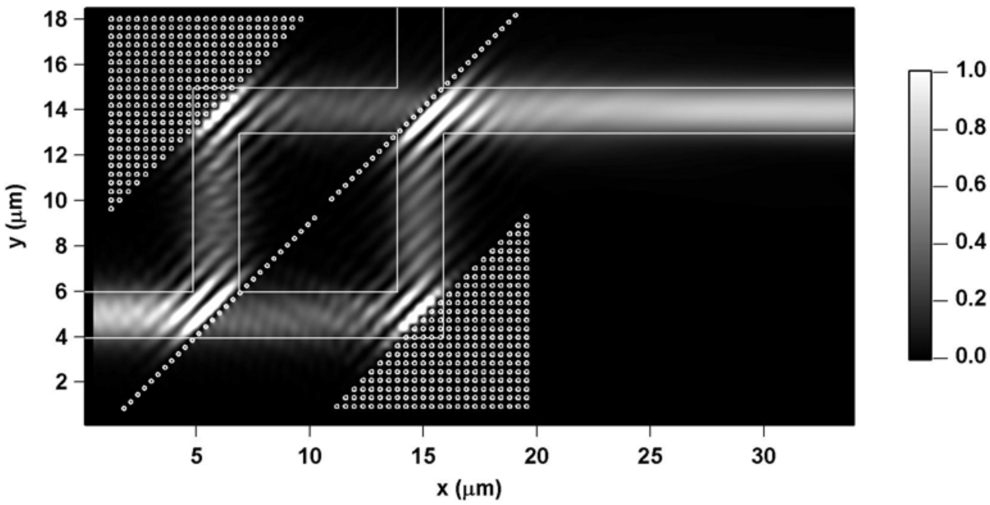

Figure 3.6. Geometry and simulation result for Mach-Zender interferometer (λ=1.55μm). The horizontal and vertical center-to-center waveguide spacing in the interferometer is 9μm. Yi cell size: 12.9 nm (λ /120).

3.4 Conclusions

In this chapter, CWGs augmented by small PhC regions offer a potential path to dramatically reduce the size of PLC components and thereby permit the realization of compact, highly integrated photonic circuits. To verify the 2-D numerical simulation results, a parallelized three-dimensional (3-D) FDTD code has been used to analyze the hybrid PhC/CWG 90 degree bend [41]. The 3-D bend efficiency is calculated as a function of the Si post height. For a Si post length of 6.5 μm, the bend efficiency is 98.6% which is very close to the 2-D FDTD result (98.7%). As long as the Si posts are long enough to intersect most of the waveguide mode, 2-D calculations are representative of actual 3-D structures.

Chapter 4

A POLARIZING BEAM SPLITTER USING A HYBRID PHC AND CWG STRUCTURE

The numerical design and analysis of an ultracompact high efficiency polarizing beam splitter with high extinction ratio are presented in this chapter [39]. While numerous approaches to realizing waveguide polarizing beam splitters have been reported in the literature [57],[58],[59],[60],[61], they typically require relatively long waveguide structures to implement (~ mm lengths). The example of the approach presented in this chapter occupies an area of only 15 μm X 10 μm. Moreover, tolerance simulation results show that its performance permits reasonable fabrication tolerances.

4.1 Design and analysis

The geometry of a high efficiency PhC/CWG polarizing beam splitter is shown in Figure 4.1(a). Light incident from the left is split into the vertical or horizontal output waveguide according to its polarization state (vertical: TM, horizontal: TE, with TM and TE defined as the electric field out of the plane or in plane, respectively). The low refractive index waveguide used in Chapter 3 is also considered here (2μm width, n_{core}=1.500, n_{clad}=1.465). The PhC is composed of a square array of silicon posts (n=3.481).

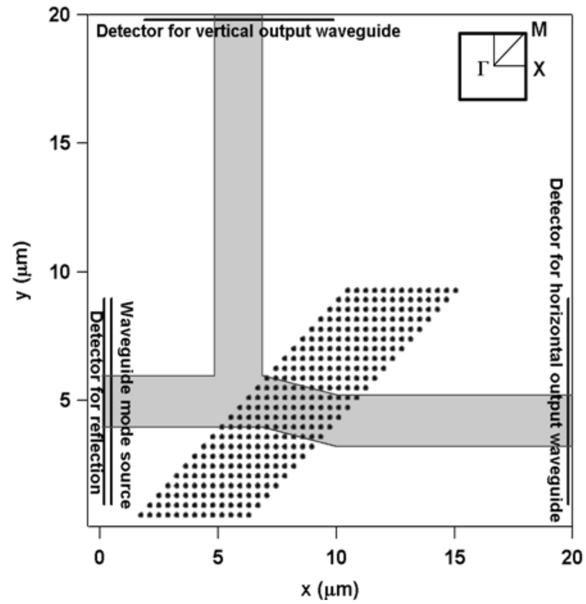

(a)

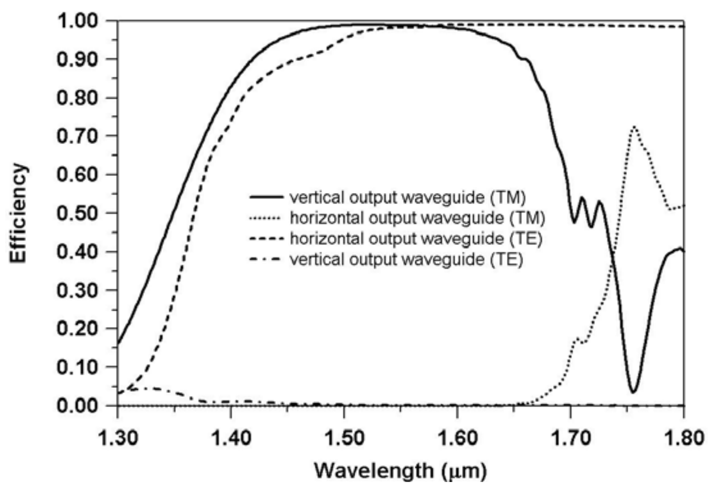

(b)

Figure 4.1. (a) The geometry for a polarizing beam splitter composed of a square array of Si posts embedded in waveguides. Waveguide mode source line and detector lines for efficiency calculations are indicated. The square inset is the Brillouin zone of the PhC. (b) Efficiencies as a function of wavelength for the TE and TM polarized incident light calculated at the detectors on the vertical and horizontal output waveguides as indicated in (a).

The boundaries between the PhC region and the CWGs are created by cuts Γ-M direction of the PhC, which is at 45 degrees with respect to the input waveguide. The lattice constant and radius of the Si posts of the PhC are 380nm and 86.8nm, respectively.

The spectral response of this structure for both TM and TE polarized incident light is shown in Figure 4.1(b) as calculated with the 2-D FDTD with Berenger perfectly matched layer boundary conditions. In the simulations, a single mode source is used to launch TM or TE light into the input waveguide and a poynting vector calculation is used to monitor the optical power in the output waveguides, which is divided by the incident power to obtain the efficiency with which light is directed into the output waveguides. From Figure 4.1(b), it is clear that this hybrid structure splits TM and TE polarizations to the output waveguides effectively for a wide wavelength range. The waveguide inside the PhC region is designed to follow the propagation direction of the TE polarized light, which leads to a 0.75 μm shift of the horizontal output waveguide in –Y direction from the input waveguide as seen in Figure 4.1(a).

The magnitude squared time averaged electric field (TM) and magnetic field (TE) at λ=1.55 μm are shown in Figures 4.2(a) and 4.2(b), respectively. TM polarized light is reflected with 99.3% efficiency at the PhC surface and guided along the vertical output waveguide while 0.06% of incident light passes through the PhC region. In the case of TE polarized light, 99.0% passes through the PhC region into the horizontal waveguide and 0.16% is reflected into the vertical output waveguide. The TM and TE output extinction ratios are 28.0dB and 32.2dB, respectively.

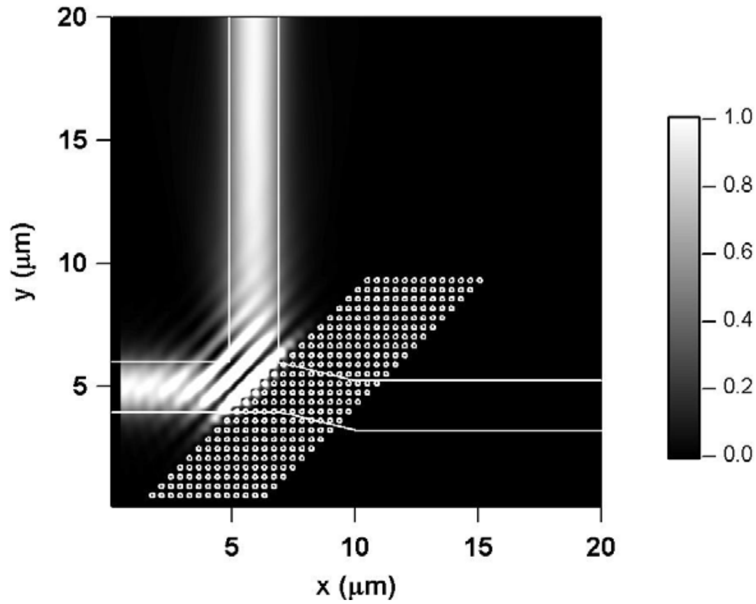

(a)

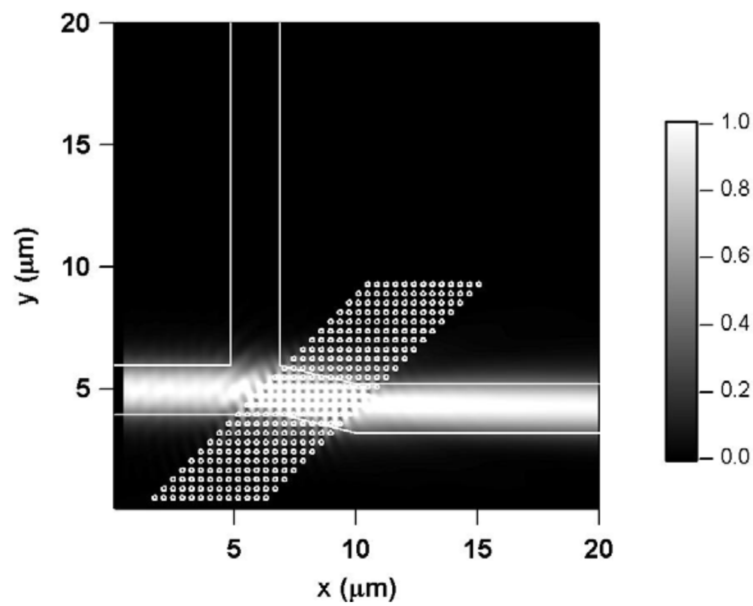

(b)

Figure 4.2. Magnitude squared time averaged (a) electric field (TM) and (b) magnetic field (TE) at λ= 1.55µm calculated by 2-D FDTD. The Yee cell size in the FDTD simulation is 10nm.

Wave vector (i.e., equifrequency) diagrams are useful to understand how the hybrid structure operates. In Figure 4.3, the wave vector diagrams for TM and TE polarization are shown for λ=1.55 μm. The horizontal axes of the wave vector diagrams correspond to the Γ-M direction of the PhC, which forms the incident interface of the PhC. The square and diamond insets in Figure 4.1 and Figure 4.3, which indicate the Brillouin zone of the PhC, show how the physical geometry is related to the wave vector diagram. In Figure 4.3, the solid semi circles in the upper half-space are allowed wave vectors in the non-PhC region (assuming this region is quasi-homogeneous with refractive index 1.485) and the dotted curves are the wave vectors of allowed propagation modes in the PhC. The solid arrows denote propagation directions of the incident, reflected, and refracted light. The refracted light propagation direction in the PhC is determined by the group velocity direction, which is calculated by the gradient of the dispersion surface. The grating vector associated with the periodicity at the boundary of the PhC is represented by the dashed arrows in Figure 4.3.

From Figure 4.3(a), one can easily see that there is no possible mode in the PhC region for TM polarized light incident along the input waveguide at a 45 degree angle with respect to the PhC surface. Moreover, there are no allowed diffraction orders from diffraction by the periodic PhC boundary. Therefore, only zero order reflection is allowed for light incidence upon the PhC boundary and this reflected light couples into the vertical output waveguide. On the other hand, TE polarized light at 45 degree incidence to the PhC boundary has a possible propagation mode in the PhC region while there are still no allowed diffraction orders as shown in Figure 4.3(b). Because the allowed wave vectors in the PhC for TE polarization form a semi-circle, the PhC region can be considered as an effective isotropic material. The calculated effective index from the wave vector diagram in Figure 4.3(b) is 1.682. This value is smaller than the effective index calculated by the area-weighted average index of the PhC because the field propagating through the PhC region is localized primarily in the low index material.

Using the effective index and considering the PhC region as an isotropic material, we can explain why 99.0% of TE polarized light can be coupled into the horizontal output waveguide. The Brewster angle calculated for the PhC effective index is 48.56°, which is close to the incident angle (45°). The reflections at both interfaces are therefore very small (0.015% for Fresnel reflection calculated with effective indices of the non-PhC region (1.485) and PhC region (1.682)). Since the reflections at both interfaces are so small, high coupling efficiency into the horizontal output waveguide for TE polarized light is obtained.

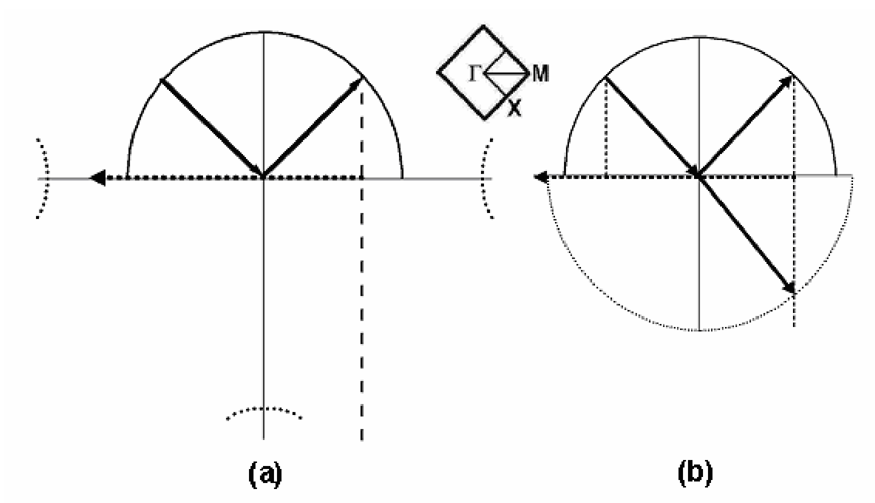

Figure 4.3. Wave vector diagrams for polarizing beam splitter at λ=1.55μm. The diamond insets indicate the first Brillouin zone with respect to the wave vector diagram. (a) TM and (b) TE.

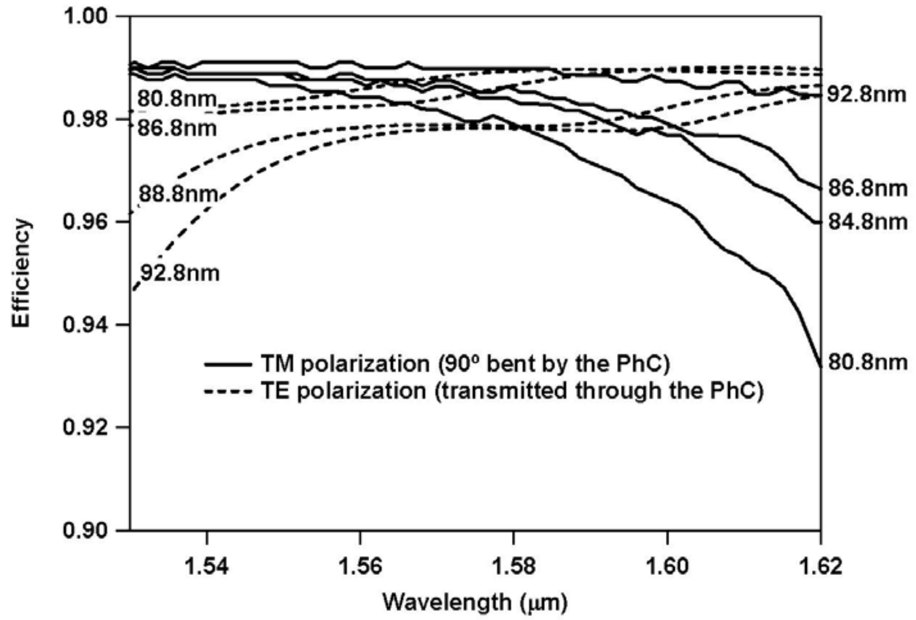

(a)

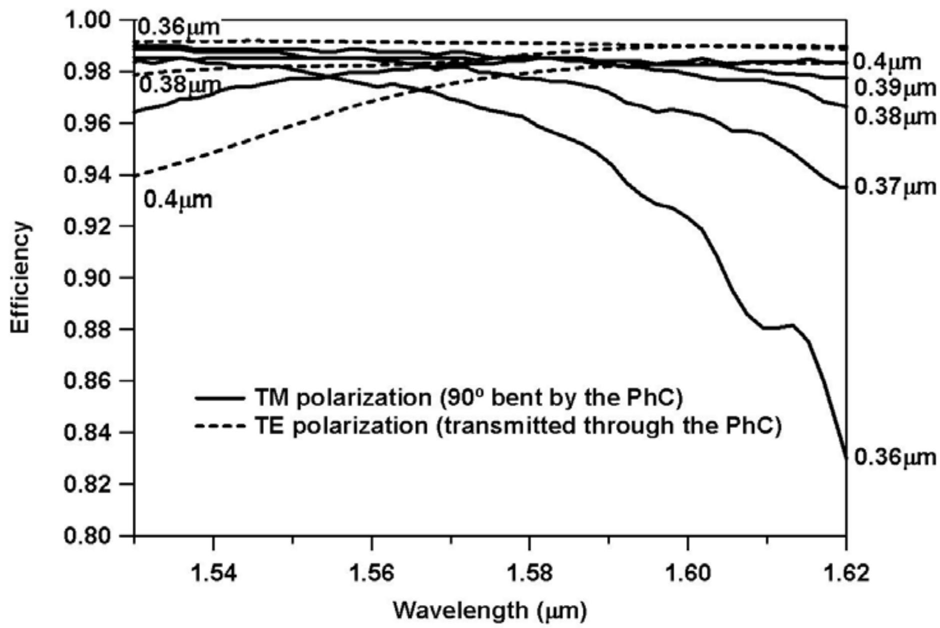

(b)

Figure 4.4. Tolerance simulation results as a function of wavelength for variation in (a) Si posts radius (design parameter 86.8 nm), (b) Si posts period (design parameter 0.38 μm).

4.2 Fabrication tolerance of the structure

In addition, polarizing beam splitter performance has been examined as a function of potential fabrication errors that affect Si post radius and period, and positional and angular misalignment of the PhC region with respect to the waveguides over the wavelength range of 1.53μm to 1.62μm (C and L bands for optical communication).

As shown in Figure 4.4(a), results for a variation in Si posts radius from 80.8nm to 90.8nm (20 nm range for the diameter) show that the TM efficiency varies between 93.0% and 99.3% while the corresponding range for the TE efficiency is 94.5% to 99.0%. At a wavelength of 1.55 μm, the efficiency for the TM polarized light at the vertical output waveguide is in the range of 98.7% to 99.3% while over 97.2% of TE polarized light is coupled into the horizontal output waveguide. The efficiencies as a function of wavelength for the PhC period changes are shown in Figure 4.4(b). The efficiencies of TM and TE polarized modes are greater than 94% for changes of the PhC period from 370nm to 400nm over the C and L bands. Also the TM and TE efficiencies are greater than 95% for ±0.5 μm misalignment of the PhC region in both the x and y directions as shown in Figure 4.5(a). A PhC angular misalignment tolerance presented in Figure 4.5(b) shows that misalignment of greater than ±1° is required before the TM efficiency drops to 95% over the wavelength range. Actual fabrication angular misalignments are of course much smaller than a degree. Our tolerance simulations show that the proposed polarizing beam splitter design has reasonable fabrication tolerances for operation over the C and L bands.

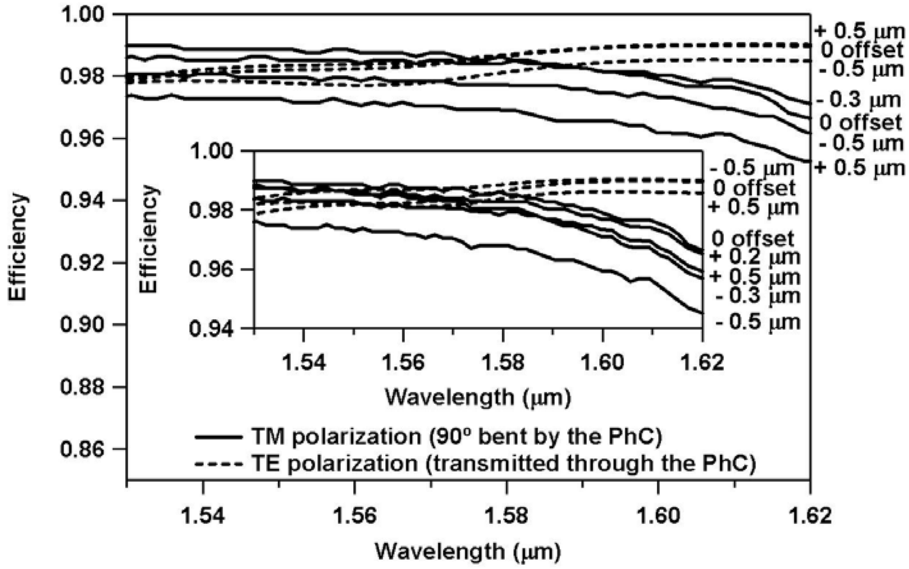

(a)

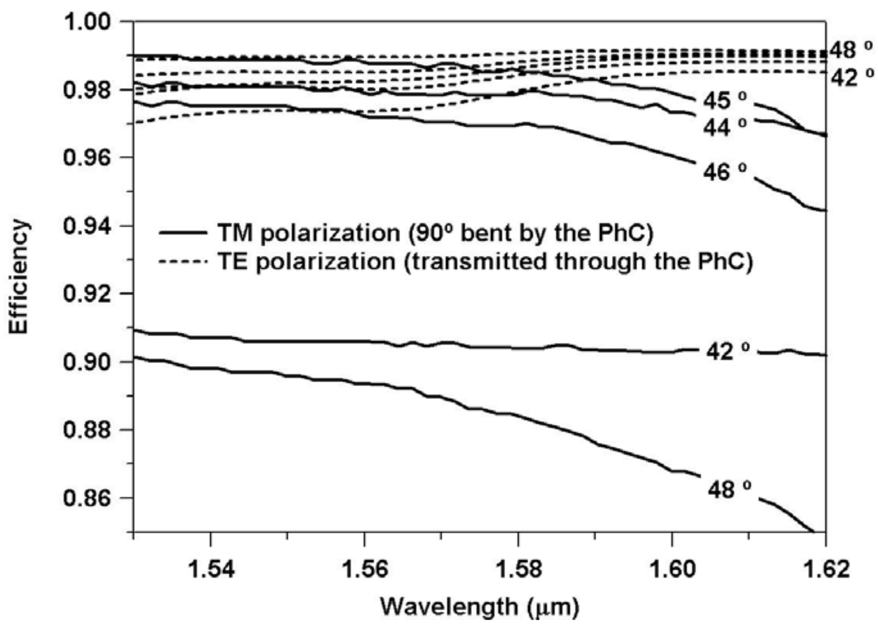

(b)

Figure 4.5. Tolerance simulation results as a function of wavelength for variation in (a) PhC region shift along the y axis (the inset is for the shift along the x axis; the design parameter is indicated as 0 offset), and (b) angle of the PhC surface with respect to the input waveguide.

4.3 Conclusions

In this chapter, an ultracompact (15 μm X 10 μm area) polarizing beam splitter design has been proposed with high efficiency (99.3% for TM polarized light and 99.0% for TE polarized light) and high extinction ratio (28.0dB for TM polarization and 32.2dB for TE polarization). The proposed ultracompact polarizing beam splitter is composed of a PhC embedded in low refractive index CWGs. The polarizing beam splitter has reasonable tolerances to fabrication errors.

Chapter 5

HYBRID PHC AND CWG STRUCTURES FOR A HIGH REFRACTIVE INDEX WAVEGUIDE WITH A LOW INDEX CONTRAST

In Chapters 3 and 4, high refractive index PhC posts embedded in low refractive index waveguides with low refractive index contrast have been examined. In this chapter the opposite case in which the PhC region is comprised of air holes in a CWG with a high refractive index core and a low refractive index contrast between the core and cladding materials is considered. A triangular lattice PhC (which has a wider photonic bandgap for TE polarization than a square lattice) is used for a 90° bend for TE polarized incident light (in-plane electric field) while a 90° bend for TM polarized light is achieved with a square lattice PhC (which has a wider directional bandgap for TM polarization than a triangular lattice). In the case of a 90° bend, the periodicity of the PhC boundary in conjunction with the high index of the core & clad regions gives rise to diffraction that limits the maximum optical efficiency of the bend. This can be overcome by changing the first layer (boundary layer) of the PhC region to suppress this diffraction. I designed these modified structures with the aid of μGA for optimization combined with a 2-D FDTD method [43],[44], for rigorous electromagnetic computation of candidate structure properties. Application of this design tool results in increases of the optical efficiencies of the bends from 56.2% to 92.5% for TE polarized light and from 72.0% to 97.4% for TM polarized light. With rows of air holes, high efficiency 90° beam splitters having total optical efficiencies of 99.4% for TE polarization (49.8/49.6 splitting ratio) and 98.8 % for TM polarization (50.6/48.2 splitting ratio) have been designed and are presented in this chapter.

In Section 5.1, 90° bends with triangular lattice PhC for TE polarized light are examined. The optimized results based on the micro-genetic algorithm are presented in this section. In Section 5.2, the equivalent case for a square lattice and TM polarized light is considered. High efficiency beam splitters for TM and TE polarizations are then presented in Section 5.3.

5.1 90° bend – TE polarization and triangular PhC lattice

A hybrid PhC/CWG 90° bend structure is considered for TE polarized light. The core and clad refractive indices of the input and output waveguides for this case are 3.25 and 3.2 (Δ=1.54%) and their widths are 2 μm. As shown in Figure 5.1(a), the dispersion relation of the triangular lattice PhC composed of air holes (n=1.000) in waveguide material, which is assumed to be quasi-homogeneous with the effective index of 3.239, for TE polarization reveals a photonic bandgap in the range of normalized frequency between $0.245(a/\lambda_0)$ and $0.404(a/\lambda_0)$ for $r/a = 0.4$ (r: radius of air holes of the PhC, a: period of the PhC, and λ_0: wavelength in vacuum). A normalized frequency of $0.319(a/\lambda_0)$, which is close to the middle of the photonic bandgap, is selected. For λ_0=1.55μm, the triangular lattice PhC has parameters r=0.198μm and a=0.495μm. A hybrid 90° bend structure using this triangular lattice PhC is illustrated in Figure 5.1(b).

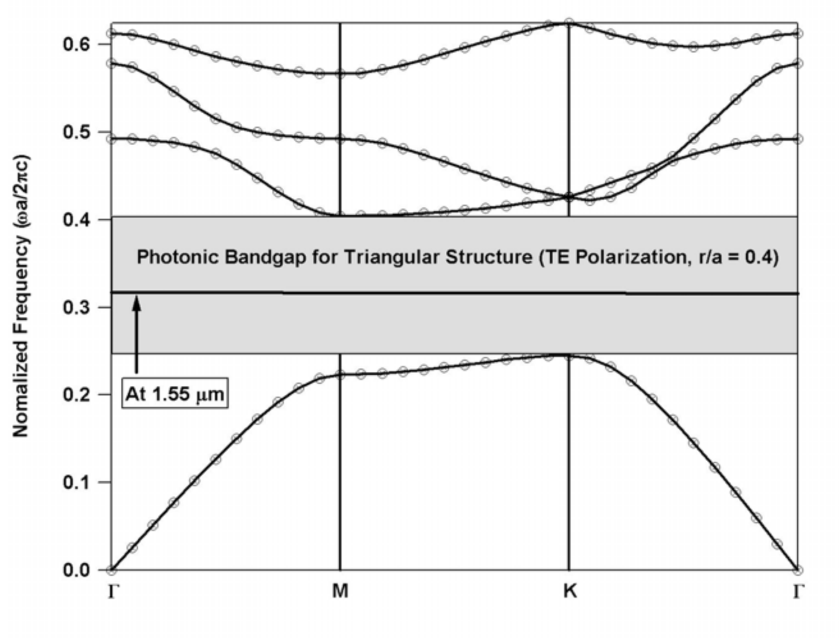

(a)

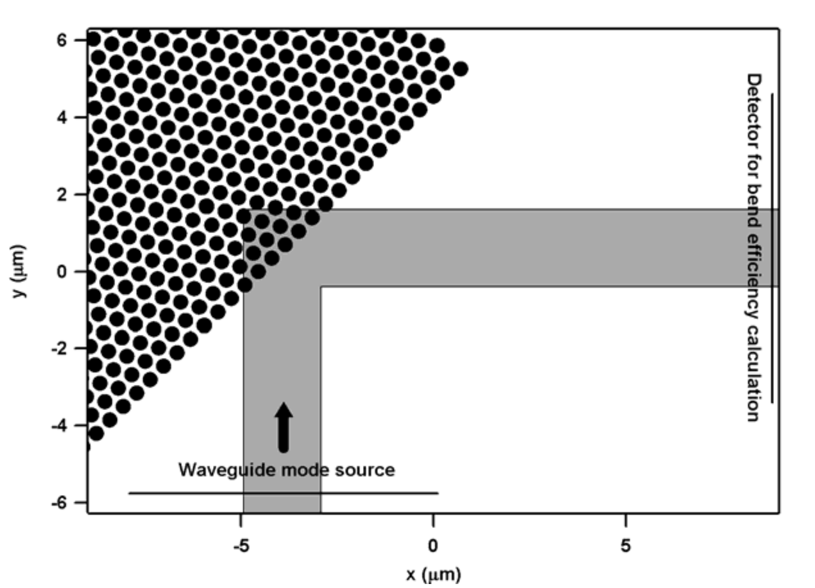

(b)

Figure 5.1. (a) Dispersion relation of a PhC composed of a triangular air (n=1.000) hole array in the waveguide material (assumed to be a quasi-homogeneous material with effective index of waveguide, n=3.239) for r/*a* = 0.4. (b) Geometry of the hybrid PhC/CWG structure.

The incident waveguide mode source position and its propagation direction are indicated, and the length and position of a detector for calculating the bend efficiency (i.e., the ratio of detected power to the incident power) are also shown. The PhC is placed at the corner of the waveguides at 45° with respect to the input waveguide. The boundary layer of the PhC corresponds to the Γ-K direction of the triangular lattice.

The magnitude squared time averaged magnetic field (which, for the TE case, is the tangential field) for the hybrid structure at λ=1.55μm is shown in Figure 5.2(a). This result is calculated with a 2-D FDTD method with Berenger perfectly matched layer boundary conditions. From Figure 5.2(a), it is found that high bend efficiency cannot be achieved because a significant fraction of incident light is diffracted by the PhC and propagates in an unwanted direction. The corresponding wave vector diagram is examined and shown in Figure 5.2(b) to understand the behavior of this structure.

In Figure 5.2(b), non-PhC and PhC regions are divided by the horizontal axis which corresponds to the PhC boundary along the Γ-K direction of the triangular lattice. The semi-circle in the upper half-space indicates the allowed wave vector in the CWG region. Since no possible mode exists in the PhC, there is nothing in the lower half-space. Solid arrows show the incident and reflected light propagation directions while the grating vector associated with the periodicity of the PhC boundary is represented by dashed arrows and an allowed diffraction order direction is indicated as a dotted arrow. For 45° incidence of the waveguide mode upon the PhC boundary, there is not only reflected light but also diffracted light propagating at a 30° angle with respect to the incident light. This agrees very well with the FDTD simulation result in Figure 5.2(a). It is clear that diffraction at the PhC boundary restricts the bend efficiency of this structure.

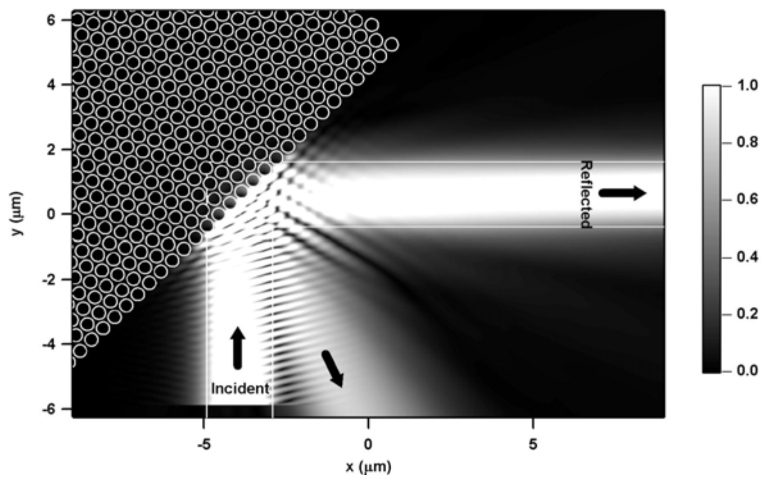

(a)

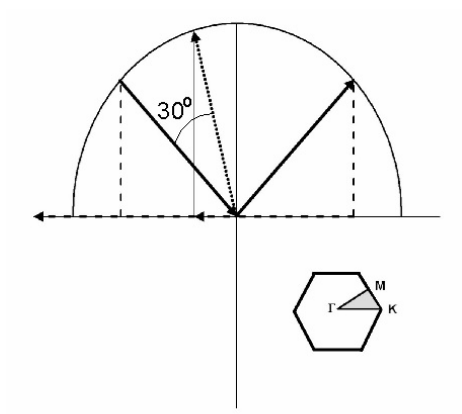

(b)

Figure 5.2. (a) FDTD simulation result of magnitude squared time averaged magnetic field at λ=1.55μm (Yee cell size : 15nm). (b) Wave vector diagram corresponding to the hybrid structure. Inset indicates the Brillouin zone of the triangular lattice PhC. The grating wave vector is calculated as $2\pi/a$ (in which a is the period of PhC lattice) and is oriented in the direction of the boundary of the PhC.

By modifying the boundary layer (i.e., the first layer) of the PhC, the diffraction effect caused by the periodicity of the boundary can be manipulated. A μGA combined with 2-D FDTD is used to maximize the bend efficiency for λ=1.55μm. The radius, period, and position of the air holes of the boundary layer are allowed to change in order to maximize the bend efficiency in the optimization process. Since there is a possible interaction between diffraction at the boundary and the allowed wave vectors in the PhC, the size of the air hole for the PhC is also allowed to change while its period and position are fixed.

In Figure 5.3(a), the bend efficiency as a function of wavelength is compared before and after μGA optimization. Structure optimization with μGA clearly results in a significantly improved bend efficiency at the design wavelength of 1.55μm. The optimized structure and the magnitude squared time averaged magnetic field for λ=1.55μm is shown in Figure 5.3(b). The radius and period of air holes for the boundary and the PhC of the optimized structure remains the same as before (r=0.198μm, *a*=0.495μm). The only difference between the structures before and after optimization is the position of the boundary layer. The boundary layer is shifted toward the CWG region by 0.566μm as shown in Figure 5.3(b) which in turn creates a small gap between the boundary layer and the PhC region. Destructive multiple beam interference for the diffracted light caused by this small gap suppresses the undesired diffraction order and increases the bend efficiency significantly from 56.2% to 92.5%.

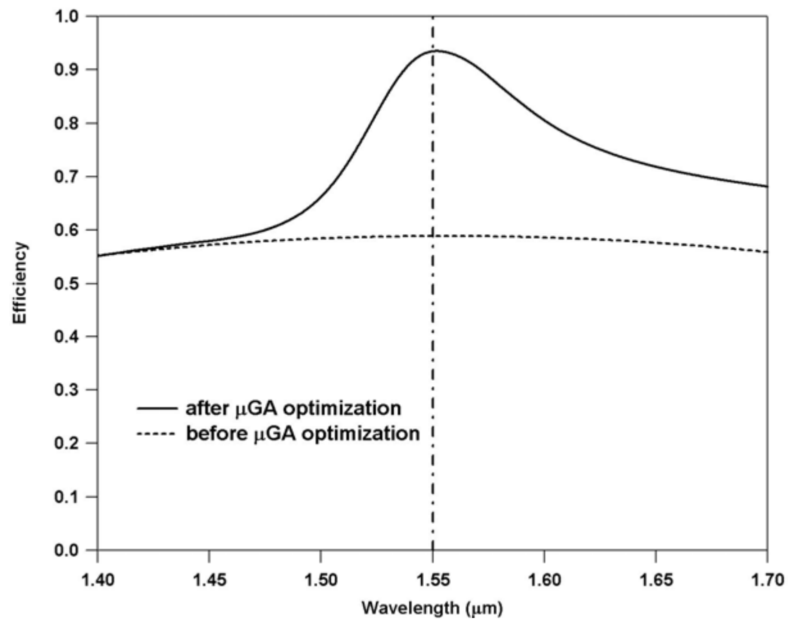

(a)

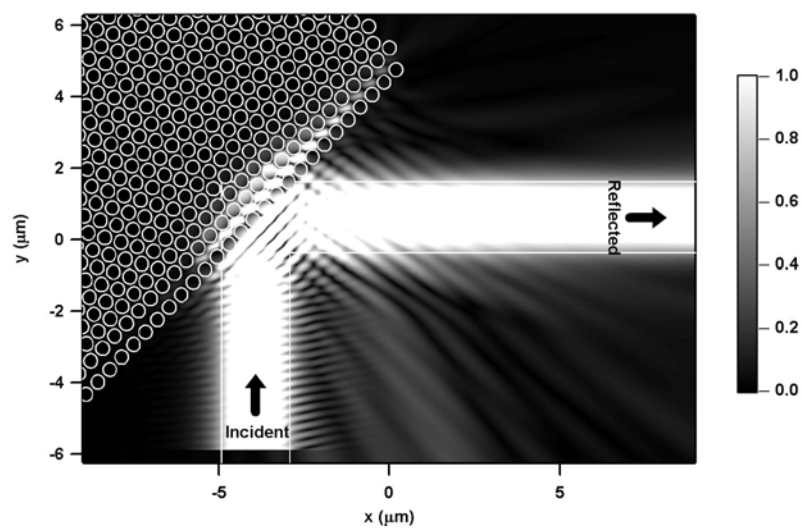

(b)

Figure 5.3. (a) Bend efficiency comparison between the structures before and after optimization. (b) Optimized hybrid structure and magnitude squared time averaged magnetic field for λ=1.55μm.

5.2 90° bend – TM polarization and square PhC lattice

A high efficiency 90° bend can be realized for TM polarized light using a square PhC lattice and the same CWG as in Section 5.1. The band diagram of a PhC composed of a square air hole array in the CWG material (quasi-homogeneous with n_{eff}=3.239) with r/*a*=0.39 is shown in Figure 5.4(a). This square lattice PhC has a directional bandgap (Γ-M lattice direction, normalized frequency range from 0.214(a/λ_0) to 0.251(a/λ_0)) that is wide enough to create a high efficiency 90° hybrid waveguide bend structure. A normalized frequency near the middle of the directional bandgap is selected to obtain an initial design for the hybrid structure. The geometry of the initial design (r=0.141μm, *a*=0.362μm) is shown in Figure 5.4(b).

Note that the boundary between the PhC and the CWGs corresponds to the Γ-X direction of the PhC lattice instead of the Γ-M direction for the low index waveguide case reported in Chapters 3 and 4. Use of the Γ-X direction as a boundary instead of the Γ-M direction presents a shorter period interface to the incident light, which decreases the number of possible propagating (i.e., non-evanescent) diffraction orders. This is a particularly important consideration for high index CWGs in which the wavelength of light in the medium is substantially smaller than for low index CWGs.

In Figure 5.5(a), the magnitude squared time averaged electric field (the tangential component of TM polarization) calculated by 2-D FDTD for λ=1.55 μm is shown with the initial hybrid structure geometry. The bend efficiency is 72.0%. A portion of the incident light is deflected backward toward the input waveguide while some propagates into the PhC region. The wave vector diagram for this structure is shown in Figure 5.5(b).

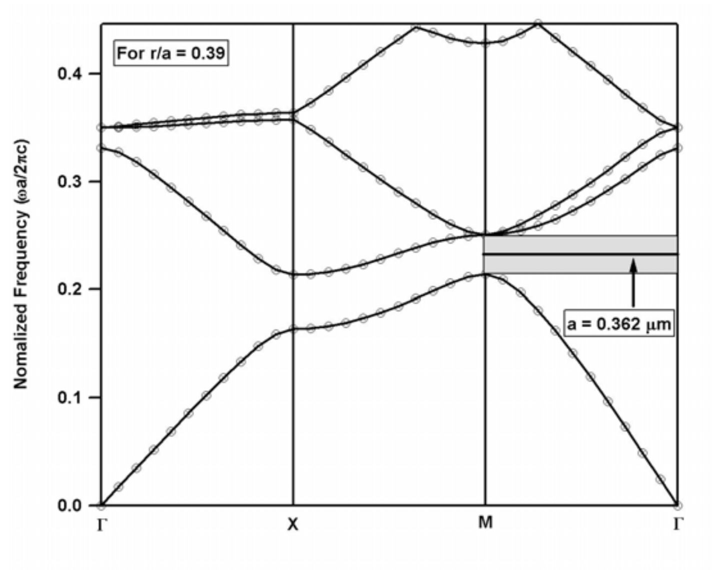

(a)

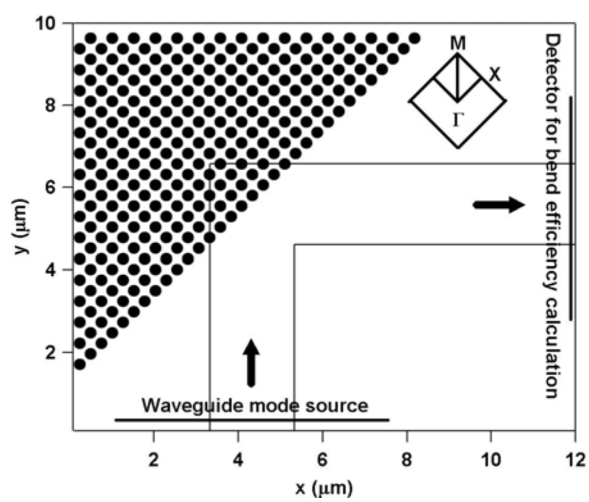

(b)

Figure 5.4. (a) Band diagram for the PhC region of hybrid structure. (b) Geometry of hybrid PhC/CWG bend for high refractive index waveguide and a PhC composed of a square array air hole lattice. A detector is used to calculate the bending efficiency. The diamond inset is the Brillouin zone of the PhC.

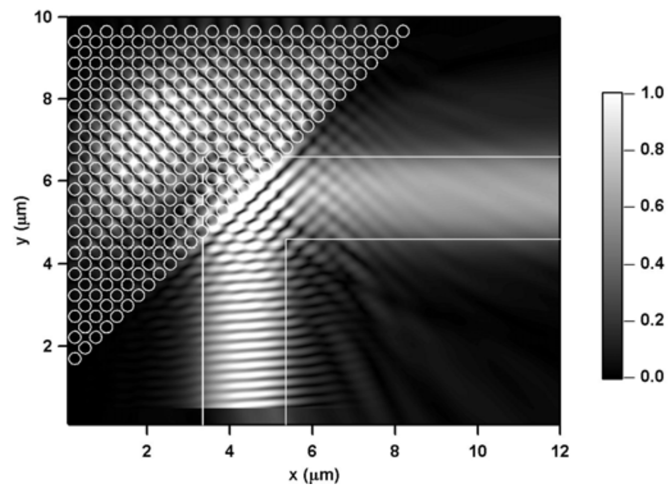

(a)

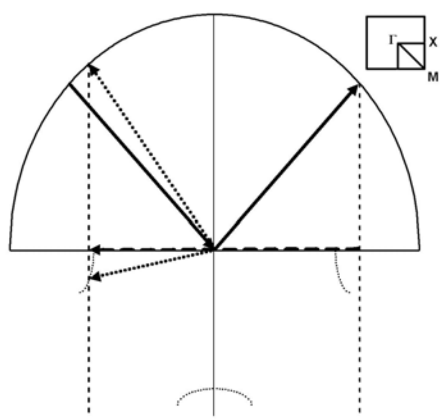

(b)

Figure 5.5. (a) Magnitude squared time averaged electric field for TM polarized light for λ=1.55μm. (b) Corresponding wave vector diagram. Two solid arrows indicate the incident light and light reflected into the output waveguide. The dashed arrow indicates the grating vector for the periodicity of the first layer of the PhC. The dotted arrows denote the diffracted light. The inset shows the orientation of the Brillouin zone with respect to the wavevector diagram. See Figure 5.4(a) for how this relates to the bend structure orientation.

The semi-circle in the upper half-space of Figure 5.5(b) indicates the allowed wave vectors in the waveguide region and the dotted curves in the lower half space denote the allowed modes in the PhC. It is evident that there are two allowed diffraction orders from diffraction by the periodic PhC boundary. One of the orders propagates nearly back along the incident waveguide and the other couples to a PhC mode as is noticed in Figure 5.5(a). The existence of these two diffraction orders limits the maximum bend efficiency that can be achieved.

Optimization with μGA is again used to design a structure with improved bend efficiency. The parameters varied in the optimization are the radius and period of the boundary layer air holes, the position of the boundary layer, and the size of the air holes for the PhC. The maximum size of the air holes in the bulk PhC region and the boundary layer is restricted such that the minimum allowable wall size (edge to edge separation of adjacent two holes) is 75 nm. Results for before and after μGA optimization are shown as the dotted and dashed lines, respectively, in Figure 5.6. The bend efficiency at λ=1.55 μm is improved significantly (95.0%) and there is a range of wavelengths (1.5133 μm to 1.5773 μm and 1.593 μm to 1.6067 μm) for which the bend efficiency is greater than 90%. Although optimization process is done for only λ = 1.55 μm, a significant improvement of the bend efficiency was obtained over most of the wavelength range shown in Figure 5.6. However, note that the peak bend efficiency is not at 1.55 μm. It is believed that this is caused by the restriction on the minimum 75nm wall size which limits the possible size of air holes of PhC. The final optimized structure is obtained by increasing the size of air holes of the PhC manually, which in turn decreases the wall size, and the result is shown as the solid line in Figure 5.6.

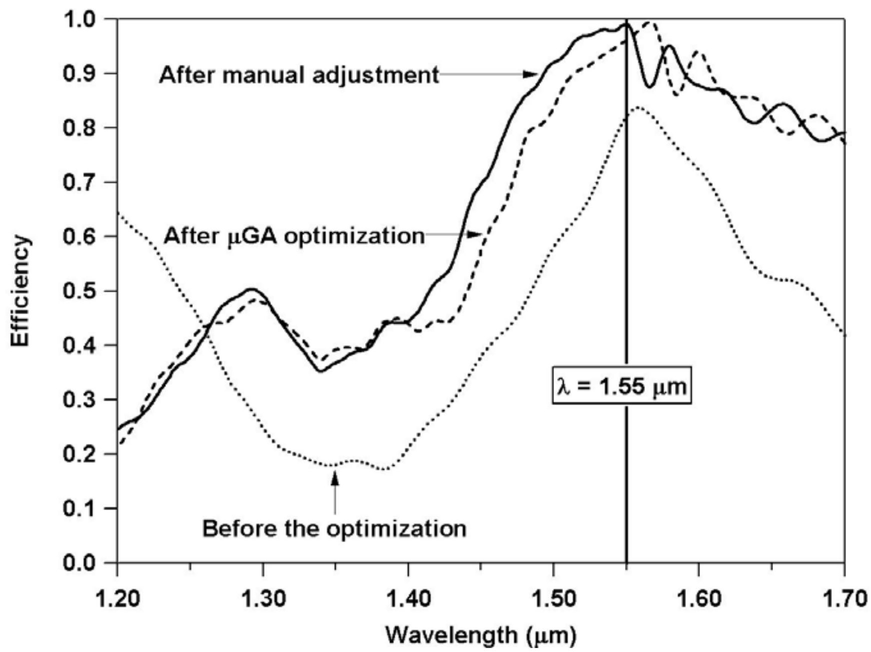

Figure 5.6. Efficiencies as a function of wavelength for the initial structure (dotted line), μGA optimized structure (dashed line), and manually adjusted structure (solid line) with removal of 75nm minimum wall size limitation.

The geometry of the final structure and magnitude squared time averaged electric field for λ=1.55 μm are shown in Figure 5.7. The air hole period of the PhC is 362 nm while the hole radius is 145 nm. The boundary layer of holes has a period of 253.85 nm with a hole radius of 89.33 nm. The position of the boundary layer is shifted 170.24 nm in the -y direction as seen in Figure 5.7. Now the wall sizes of the PhC and the optimized boundary layer are 72 nm and 75.19nm, respectively. The bending efficiency at 1.55μm is improved to 97.43%.

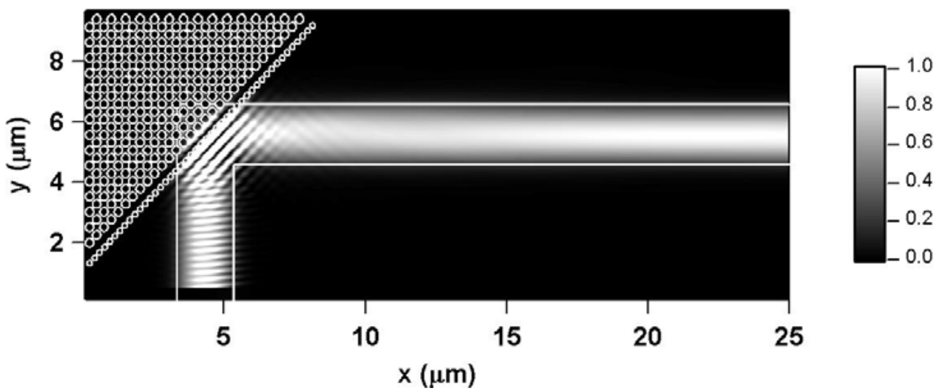

Figure 5.7. μGA-optimized hybrid structure for high index waveguide and simulation result for λ=1.55μm

5.3 High efficiency beam splitters

As illustrated in Figure 5.8(a), a 90° beam splitter can be formed with a row of air holes. The spectral response for TM polarized light and a 1 layer air hole array with a 268.7 nm period and a 105 nm air hole radius are shown in Figure 5.8(b). At λ=1.55μm, 49.8% of incident light is directed into the horizontal output waveguide while 49.6% is coupled into the vertical output waveguide (for a total efficiency of 99.4%).

Note that the spectral response of this is quite broad. This high efficiency beam splitter is essentially a subwavelength diffraction grating that generates no propagating diffraction orders beyond the transmitted and reflected zero orders.

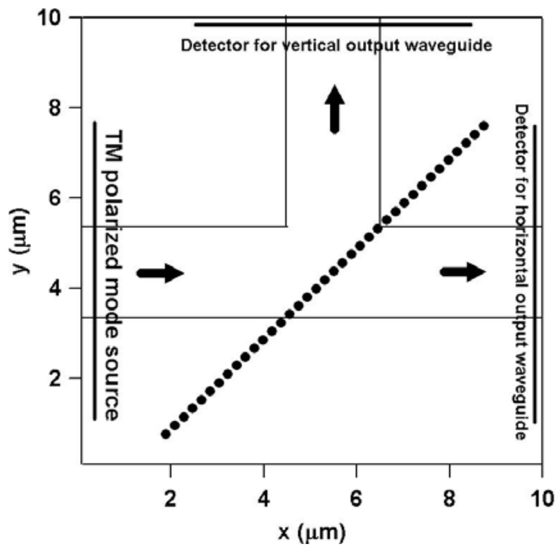

(a)

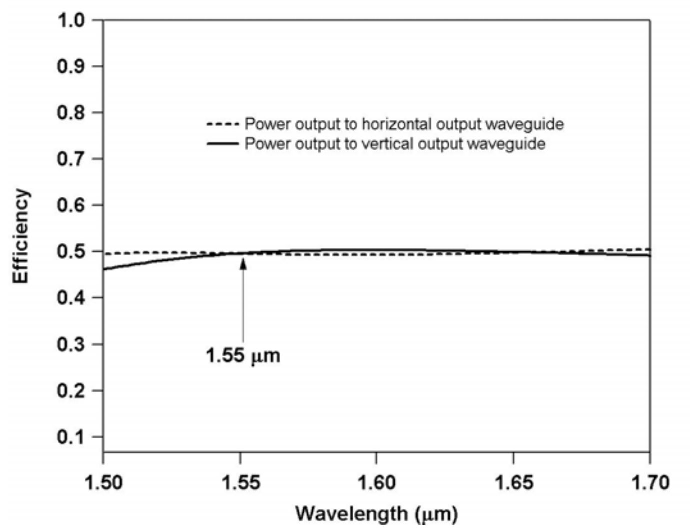

(b)

Figure 5.8. (a) Geometry of high efficiency beam splitter for high refractive index and low index contrast waveguide (For TM polarization). Detector positions to calculate the efficiencies at the horizontal and vertical output waveguides are indicated. (b) The efficiencies at the horizontal and vertical output waveguides as a function of wavelength.

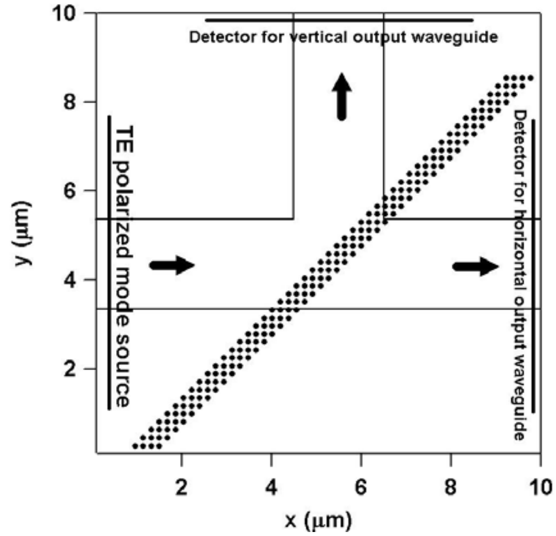

(a)

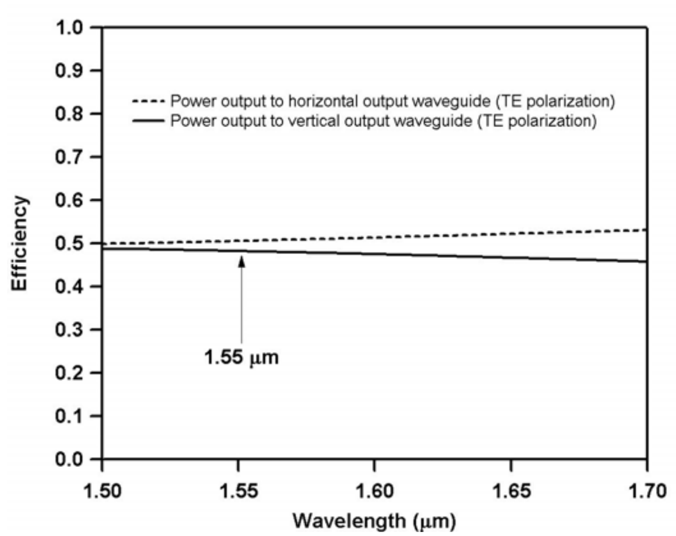

(b)

Figure 5.9. (a) High efficiency beam splitter geometry for TE polarization with input waveguide mode source line and detectors for calculating efficiencies at both output waveguides. (b) Spectral responses for the geometry shown in Figure 5.9(a) at both horizontal and vertical output waveguides.

A beam splitter for TE polarized light can be created alternatively with a 4-row air hole array as shown in Figure 5.9(a) (radius = 64nm, period = 255nm, row separation = 180nm). The spectral response of this structure is shown in Figure 5.9(b). At λ=1.55μm, 50.6% and 48.2 % of the incident light are directed into the horizontal and vertical output waveguides, respectively (98.8% total efficiency).

5.4 Conclusions

Hybrid PhC/CWG bends in high refractive index, low index contrast waveguide material systems require careful design to avoid efficiency-limiting diffraction from the periodic PhC boundary. Our rigorous μGA/FDTD design tool has been shown to be effective in designing high efficiency 90° bends by changing the properties of the boundary layer to suppress unwanted diffraction. High efficiency beam splitters for TM and TE polarizations using the given waveguide structure are designed by simply putting rows of 45 degree tilted air hole array. Wide wavelength ranges of high efficiency splitting are achieved for both TM and TE polarization.

Chapter 6

ULTRACOMPACT HIGH EFFICIENCY BEND STRUCTURE FOR LOW INDEX WAVEGUIDE USING AIR HOLE PHC STRUCTURES

Designs presented in previous chapters have high refractive index differences between the periodic materials for the PhC and waveguide materials. In contrast, low refractive index periodic materials for the PhC region are considered in this chapter to achieve high efficiency 90 degree bend of low refractive index waveguides. Air hole arrays for the PhC are used to achieve high efficiency 90 degree bend within a very small area for the silica and polymer waveguides. Those two polymer waveguides considered in this chapter are called Waveguides 1 and 2. The refractive indices of Waveguide 1 are n_{core}=1.486 and n_{clad}=1.477 with 4.0μm core width while Waveguide 2 has a 3.5μm core (n_{core}=1.630) surrounded by a clad (n_{clad}=1.625). In this chapter, bend efficiencies are calculated with the mode overlap integral (MOI) [62] method for accurate calculations.

6.1 Designs and numerical simulation results for silica waveguide bend

Silica waveguides are an especially attractive technology platform for planar lightwave circuits (PLCs) because of their low propagation loss, low coupling loss to optical fiber, and mature micro fabrication processes [63],[64],[65],[66],[67],[68]. However, a key drawback is the relatively large radius of curvature (on the order of multiple mm's to cm's, [3]) required to achieve high efficiency waveguide bends, which limits the compactness of PLC components.

Despite high propagation losses [51], most research has focused on material systems that have a large refractive index contrast ($\Delta n \geq 1.5$) in the PhC to maximize the photonic bandgap. Liguda et al. recently reported fabrication of a relatively low refractive index contrast ($\Delta n = 0.5$) PhC composed of a 2D array of air holes in a polymer slab waveguide. Both numerical and experimental results verify the presence of a directional bandgap (photonic bandgap only for specific lattice direction) [69].

In this section, an air hole PhC region in a high Δ (0.75%, $\Delta = (n_{core}-n_{clad})/n_{core}$) single mode silica waveguide is considered to achieve an ultracompact high efficiency 90 degree bend. A periodic air hole array in a silica waveguide is optimized to suppress diffraction from the periodic PhC boundary to achieve a high efficiency 90 degree bend for TM polarized light.

The initial hybrid structure considered is shown in Figure 6.1(a). The silica waveguide core has a 6μm square cross section. The core and clad refractive indices are 1.456 and 1.445, respectively. For our 2-D calculations, the 2-D effective index of the core region (1.453) is used. As shown in Figure 6.1(a), the PhC is composed of a square air hole array that is designed based on the dispersion relation shown in Figure 6.1(b). Although a full photonic bandgap is not found, there is a directional bandgap shown as the shaded region in the normalized frequency range from 0.375 (a/λ_0) to 0.429 (a/λ_0). To obtain an initial structure for the PhC region, a normalized frequency of 0.402 (a/λ_0) which is in the middle of the directional bandgap is selected. Then this normalized frequency is matched to the desired operational wavelength, which is 1.55 μm.

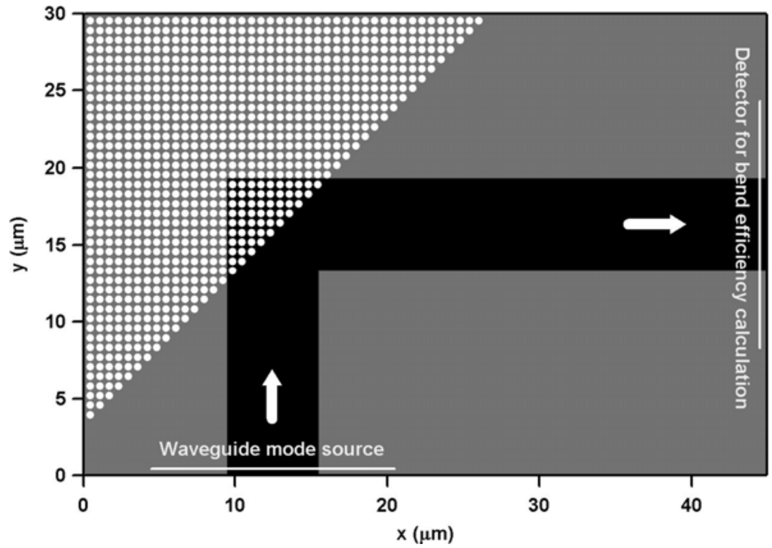

(a)

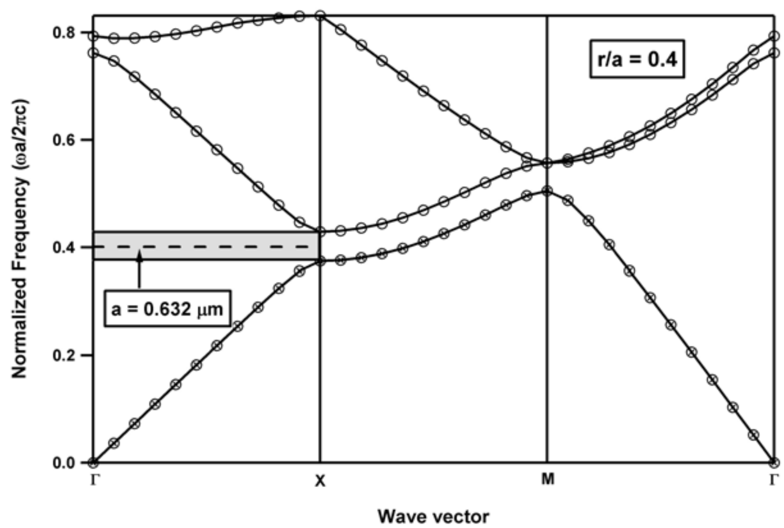

(b)

Figure 6.1. (a) The base hybrid structure. White arrows in the input and output waveguides indicate light propagation directions. (b) Dispersion relation for r/*a*=0.4, air hole array (n=1.000) in quasi-homogeneous medium (n_{eff}=1.451, which is the effective index of waveguide mode) for TM polarization.

The period of the air hole array for the PhC is calculated to be 0.623 μm and the air hole radius is 0.25μm (r/*a*=0.4). This PhC structure is placed at the silica waveguide 90^o bend.

The boundary surface between the PhC region and silica waveguide region is along the Γ-M lattice direction of the PhC and this surface is oriented at 45 degrees with respect to the input waveguide. The hybrid structure is rigorously simulated by a 2-D FDTD method with Berenger perfectly matched layer boundary conditions. A TM waveguide mode source is launched in the 2-D FDTD computational space and a line detector is used to calculate the bend efficiency at the output waveguide illustrated in Figure 6.1(a). The waveguide mode source and line detectors are 16 μm long. The bend efficiency of the hybrid structure is calculated with MOI and is defined as the ratio of the power in the guided mode at the output detector to the incident guided mode power.

In Figure 6.2(a), the magnitude squared time averaged electric field calculated by 2-D FDTD is shown superimposed on the hybrid structure geometry. Since the incident light propagation direction (Γ-X lattice direction of the PhC) corresponds to the directional bandgap for TM polarized light at λ=1.55μm, no light is coupled into the PhC region. However, the bend efficiency is only 8.3%. Most of incident light is diffracted backwards nearly towards the source.

The origin of this diffraction can be understood using the wave vector diagram in Figure 6.2(b) in which the horizontal axis corresponds to the Γ-M direction of the PhC (i.e., the boundary between the PhC and CWG regions). The diamond inset indicates the orientation of the first Brillouin zone of the PhC with respect to the wave vector diagram.

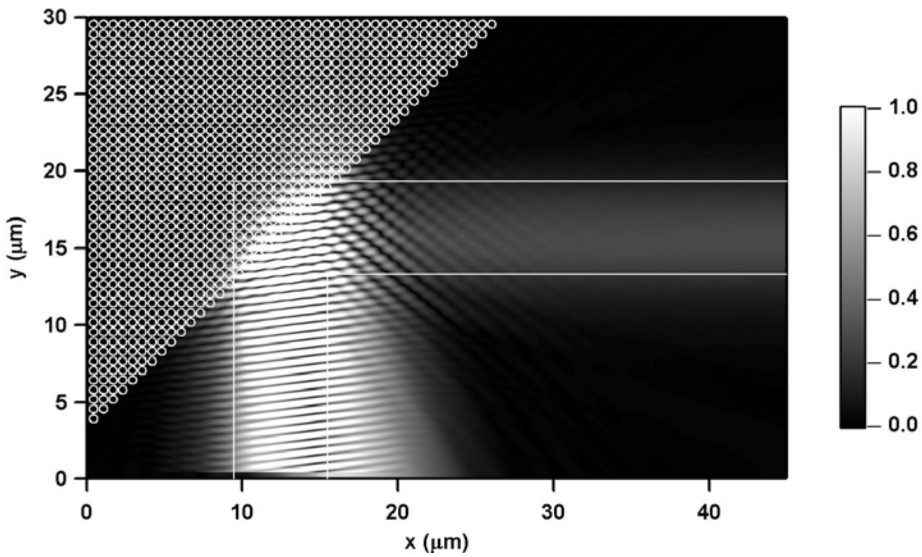

(a)

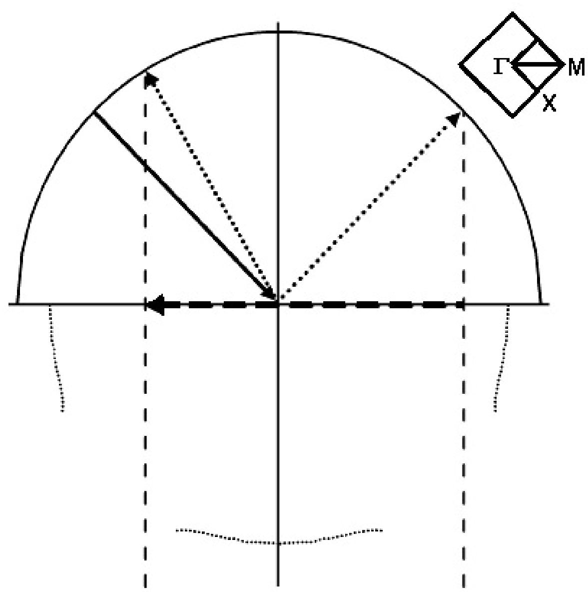

(b)

Figure 6.2. (a) Magnitude squared time averaged electric field calculated by 2-D FDTD for the structure shown in Figure 6.1(a) at λ= 1.55μm. (b) Corresponding wave vector diagram for the base structure. The diamond inset indicates the Brillouin zone of the PhC.

The upper solid semi circle indicates allowed wave vectors in the silica waveguide region (which is assumed to be quasi-homogeneous with a refractive index of 1.451). The lower dotted curves represent allowed propagation modes in the PhC region. The solid arrow corresponds to light from the waveguide incident at a 45 degree angle to the Γ-M boundary surface. The dashed arrow along the horizontal axis denotes the grating vector associated with the periodicity of the PhC boundary. The wave vector diagram clearly shows that no light can be coupled to allowed modes in the PhC region. Therefore, light can only be reflected or diffracted into the CWG region. These allowed states are denoted as dotted arrows in Figure 6.2(b), and are precisely what is observed in Figure 6.2(a), with most of the optical power carried in the diffraction order caused by the periodic PhC boundary.

Clearly, the diffracted light needs to be suppressed to obtain high bend efficiency. To this end, μGA combined with 2-D FDTD is again used to modify the boundary layer of the PhC. The variables to be optimized are the air hole radii of both PhC and the boundary layer, the period of boundary layer, and the X and Y position of the boundary layer. After μGA optimization, the bend efficiency is improved to 97.7% from 8.3% at λ=1.55μm.

Since μGA optimization is based on 2-D FDTD results with a relatively small number of time steps (8,000) and low resolution (31nm Yee cell size) in order to minimize computation time, a more detailed manual search is then performed. After all optimization processes, a bend efficiency of 99.4% is obtained at λ=1.55μm. The ratio of the power calculated at the detector to the input source power as a function of wavelength for the final optimized structure is shown in Figure 6.3 along with the bend efficiency (without MOI) before the optimization process. Using an MOI calculation, over 99.0% bend efficiencies are obtained for wavelengths in between 1.54μm and 1.56μm.

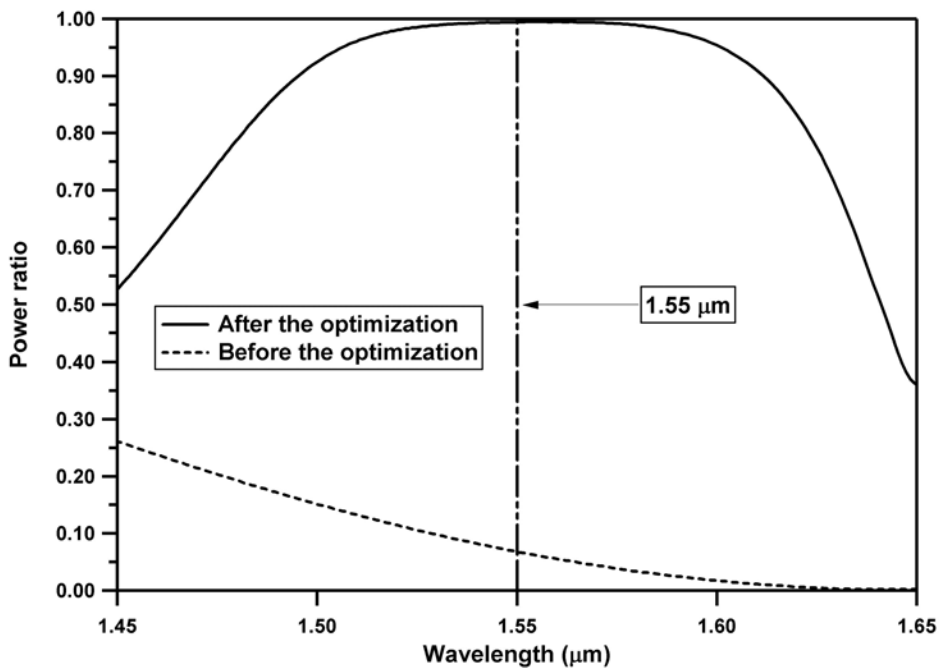

Figure 6.3. Bend efficiency as a function of wavelength for the initial structure (dashed line) and the structure after the optimization process (solid line).

The final optimized structure has an air hole radius in the PhC region of 0.26μm while in the boundary layer radius is increased to 0.275μm and the period is unchanged. The position of the boundary layer is shifted 0.2μm in the X direction and 0.82μm in the negative Y direction. The magnitude squared time averaged electric field plot with its optimized geometry is shown in Figure 6.4. There is no evidence of the diffraction order that spoiled the bend efficiency of the original structure. It has been effectively suppressed by the boundary layer and bulk PhC modifications such that the bend efficiency is increased to 99.4%.

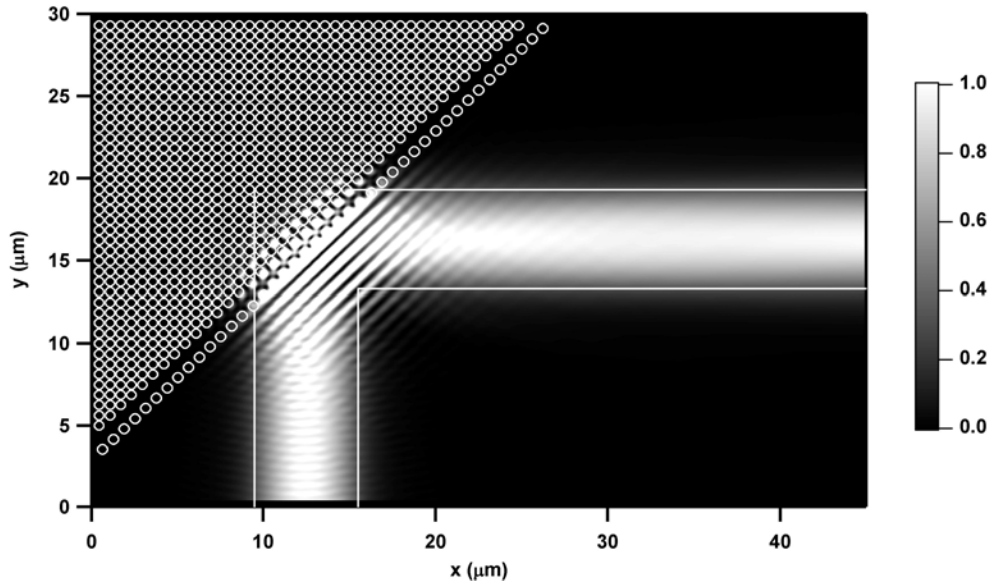

Figure 6.4. Magnitude squared time averaged electric field at λ=1.55μm for the final optimized geometry.

6.2 Designs and numerical simulation results for Waveguide 1

To design a polymer waveguide 90 degree bend structure using an air hole PhC region, the approach for high efficiency 90 degree silica waveguide bend structure design has been followed. The geometry of hybrid PhC and CWG structure for Waveguide 1 before the μGA optimization is shown in Figure 6.5. Waveguide 1 has refractive indices of n_{core}=1.486 and n_{clad}=1.477 with 4μm core width. The structure is chosen to be the wavelength of 1.55μm on the middle of the partial bandgap of PhC comprised of air holes (r/*a*=0.4).

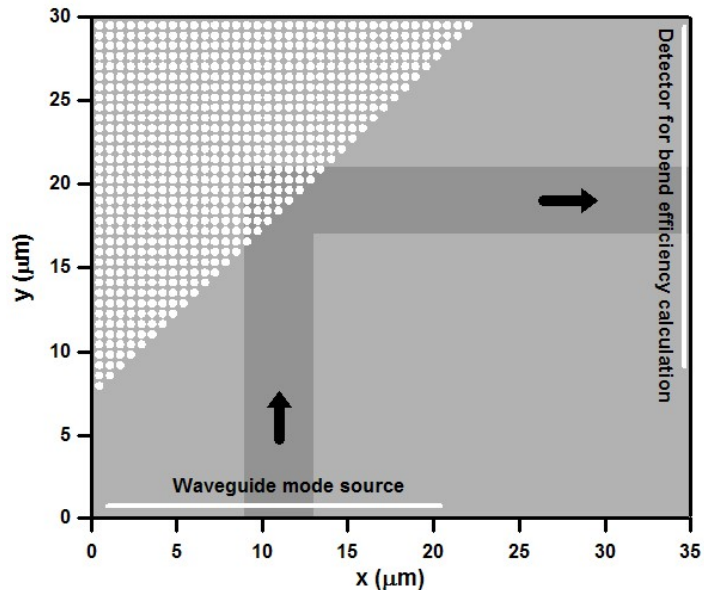

Figure 6.5. Geometry of the hybrid 90 degree waveguide bend for the Waveguide 1 before the μGA optimization.

The structure is optimized with μGA-FDTD by varying parameters of radii and periods of air holes for PhC and boundary layer and the position of the boundary layer relative to the PhC region. After the optimization, the radii of air holes for the PhC region and boundary layers are 180nm and 320nm while the periods of the PhC and boundary layers are 588nm and 597nm. The position of boundary layer is shifted 285nm to the X direction and 337nm to the negative Y direction from its initial position. The magnitude squared time averaged electric fields for the structures of both before and after the optimization are shown in Figure 6.6. Diffraction is well suppressed after the optimization and the bend efficiency at the wavelength of 1.55μm is improved to 98.95%

from 7.9%. The comparison of spectral responses between the structures before and after optimization is presented in Figure 6.7. It is clear that bend efficiency is well optimized over the wavelength range. For the wavelengths in between 1.53μm and 1.58μm, the bend efficiency is greater than 95.0%.

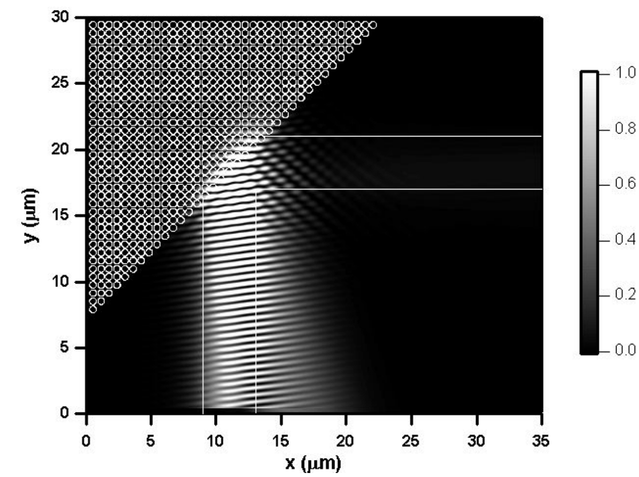

(a)

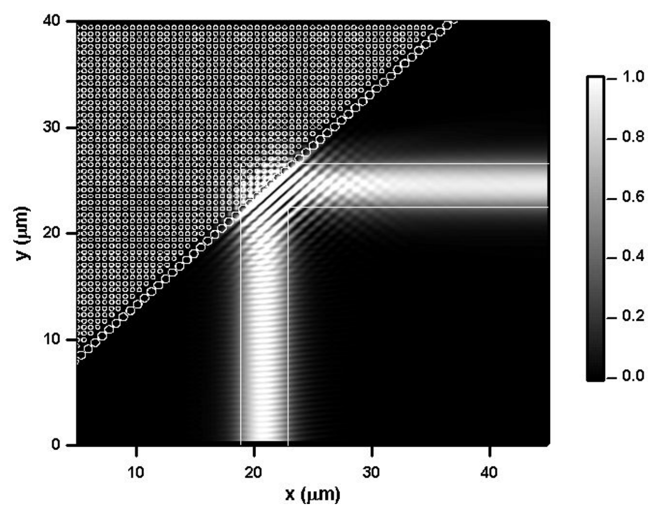

(b)

Figure 6.6. Magnitude squared time averaged electric field for structures (a) before and (b) after optimization.

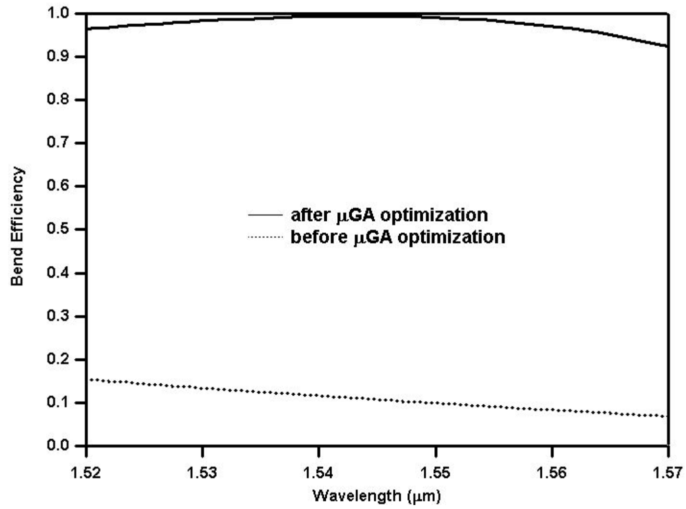

Figure 6.7. Spectral responses for the structures of before and after the optimization.

6.3 Designs and numerical simulation results for Waveguide 2

The approach using hybrid PhC and CWG structures to achieve 90 degree waveguide bends is not limited by the target wavelength. For λ=1.33μm, an ultracompact high efficiency polymer 90 degree bend for TM polarization is designed. The base geometry is presented in Figure 6.8(a) with the magnitude squared time averaged electric fields for structures before the optimization at the wavelength of 1.33μm. As seen from Figure 6.8, the waveguide has a 3.5μm wide core (refractive index=1.630) surrounded by clad (refractive index=1.625). Before the optimization, the PhC region is composed of an air hole array with the period of 480nm and the radius of 197nm. To maximize the bend efficiency, the boundary layer of the PhC is optimized by μGA.

As shown in Figure 6.8(b), bend efficiency at λ=1.55μm is improved significantly again after the optimization. The bend efficiency is improved to 99.3% from 14.5%.

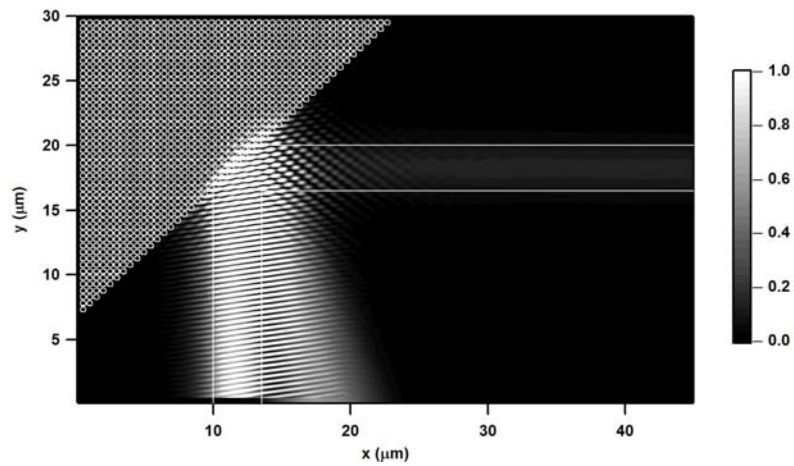

(a)

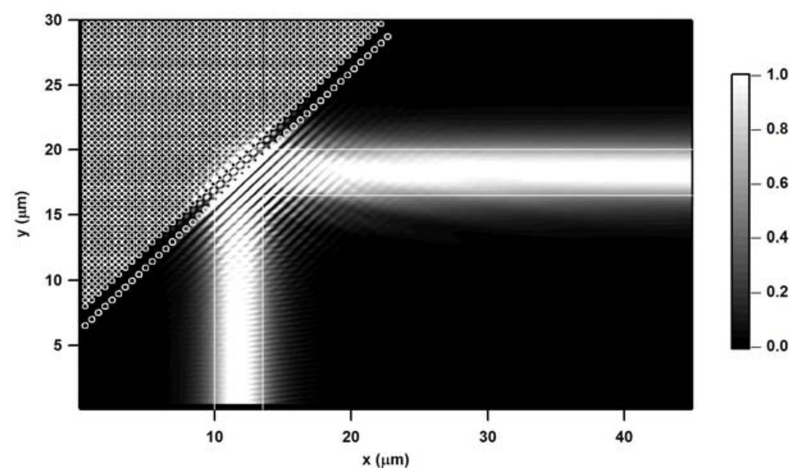

(b)

Figure 6.8. Magnitude squared time averaged electric field for λ= 1.33μm with geometry of hybrid PhC and polymer waveguide structure (a) before and (b) after μGA optimization. The radii of air holes for the PhC and boundary layer are increased to 190nm and 221nm after the optimization. The boundary layer is shifted 988nm to negative Y direction.

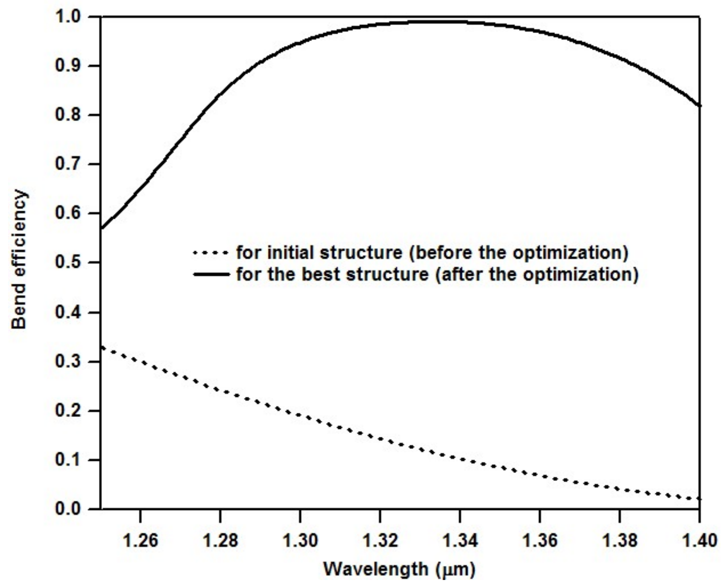

Figure 6.9. Spectral responses for structures before (dashed line) and after (solid line) optimization.

In Figure 6.9, the spectral responses for both structures before and after the optimization over the wavelength range (1.25µm-1.40µm) as a function of wavelength are presented. Even though the structure is optimized to maximize the bend efficiency for the wavelength 1.33µm, the bend efficiency is improved for all wavelengths.

6.4 Conclusions

High efficiency (99.4%) silica waveguide 90 degree PhC/CWG bend structure for TM polarized light that occupies an area of 27µm X 27µm is achieved and presented in this chapter. Two different polymer waveguide structures are considered to achieve high efficiency 90 degree bends with air hole PhC structures. One is optimized for the 1.55µm wavelength (with bend efficiency of 98.95%) and another is done for λ=1.33µm (with bend efficiency of 99.3%). Diffractions associated with the periodic boundaries of the PhC regions can be effectively suppressed by use of a μGA optimization procedure. For all three cases, the bend efficiencies are significantly improved after μGA optimizations.

Chapter 7

NEW RING RESONATOR CONFIGURATION USING HYBRID PHC AND CWG STRUCTURES

A new configuration to realize a ring resonator using the hybrid photonic crystal and conventional waveguide structures is presented in this chapter. The proposed ring resonator configuration is advantageous compared with general ring resonator structures for its performance and controllability of the quality (Q) factor, free spectral range (FSR), and full width at half maximum (FWHM) over a wide range. The ring resonator structures are based on a single mode waveguide with core and clad refractive indices of 1.5 and 1.465, respectively. A ring resonator is constructed within 35μm x 50μm area and used as a base ring resonator. 2-D FDTD simulation results demonstrate a FSR of 14.1nm and a Q factor of 595 with high optical efficiency (92.7%). Examples, which are modified from the base ring resonator to show the controllability of the FSR and Q factor, are followed. By decreasing the light propagation distance in the ring resonator, the FSR is increased to 19.8nm. A ring resonator with a 1600 Q factor is achieved by modifying splitter structures in order to increase the power fraction guided along the output waveguide which is at 90 degrees with respect to the input waveguide.

7.1 Motivation

Ring resonators have been investigated for a variety of applications including add/drop filters, band pass filters, wavelength division multiplexer/demultiplexers, and all optical switches [70],[71],[72],[73],[74],[75]. Ring resonators reported in the literature are generally constructed by placing a circular or oval waveguide between two straight waveguides. Light of particular wavelengths is coupled from one straight waveguide to the other. These are called drop wavelengths. As the platforms to build ring resonators, two waveguide types are mainly used. One is a low refractive index waveguide with low index contrast between the core and clad [72],[73],[74],[75]. This type of waveguides has advantages, such as low propagation loss, low coupling loss from the fiber, and low dispersion. However, since very large bend radius is needed for a low index contrast waveguide to achieve high efficiency bend, ring resonators based on such waveguides require a very large radius for the circular or oval waveguide which in turn increases the overall size of a ring resonator and limits the maximum free spectral range (FSR) [72], [73]. Another waveguide type is a high core refractive index waveguide with high index contrast [70],[71]. In this case, the waveguide mode is strongly confined in the core region. Therefore, high efficiency bend can be achieved with very small bend radius ($< 10\mu m$) which in turn results in a small ring resonator structure. However, high index contrast waveguides generally suffer high fiber to the waveguide coupling loss because the waveguide mode size ($< 2\mu m^2$) is so much smaller than that of a fiber ($\sim 50\mu m^2$) [70].

In this chapter, a new ring resonator configuration constructed by hybrid structures of low index contrast waveguide bends and splitters is presented. A ring resonator which has a 2.5nm full width at half maximum (FWHM which is a spectral width of adjacent wavelengths having half of the maximum power of a drop wavelength), a 14.1nm FSR (separation of two adjacent drop wavelengths), and a 595 quality (Q) factor ($\lambda_{drop}/\Delta\lambda_{FWHM}$) is designed. This structure is used as a base ring resonator for further modification to show how increased FSR and Q factor can be achieved. The FSR of 19.8nm is achieved by decreasing the light propagation distance in the ring resonator while the Q factor is increased to 1600 by changing the splitter structures of the base ring resonator to increase the power fraction guided along the orthogonal output waveguide with respect to the input waveguide.

7.2 Design of a ring resonator

A two-dimensional (2-D) single mode waveguide (at λ=1.55μm) with a 2μm core width and core and clad refractive indices of 1.5 and 1.465 is considered. As shown in Figure 7.1, a PhC region composed of a square Si (n=3.481) posts array (100nm radius and 380nm lattice constant) is used to achieve an high efficiency 90 degree waveguide bend while a single row of Si posts tilted at 45 degree (100nm radius and 424nm period) function as a high efficiency splitter. Both are designed to operate with TM polarized light (i.e., electric field out of the plane). To numerically calculate the optical efficiencies of both the bend and splitter which are the ratios of the power at the output waveguides to the input power, a 2-D FDTD method with Berenger perfectly matched layer boundary condition is used. The waveguide mode source along the input waveguide for both the bend and splitter has 8μm width as illustrated in Figure 7.1. To monitor the output power, the 8μm wide detectors are placed at the output waveguides.

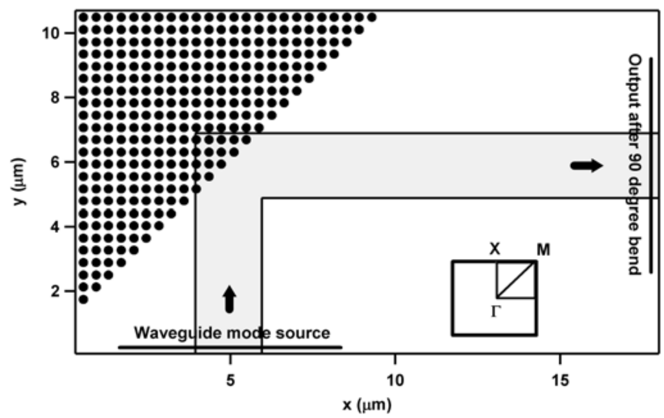

(a)

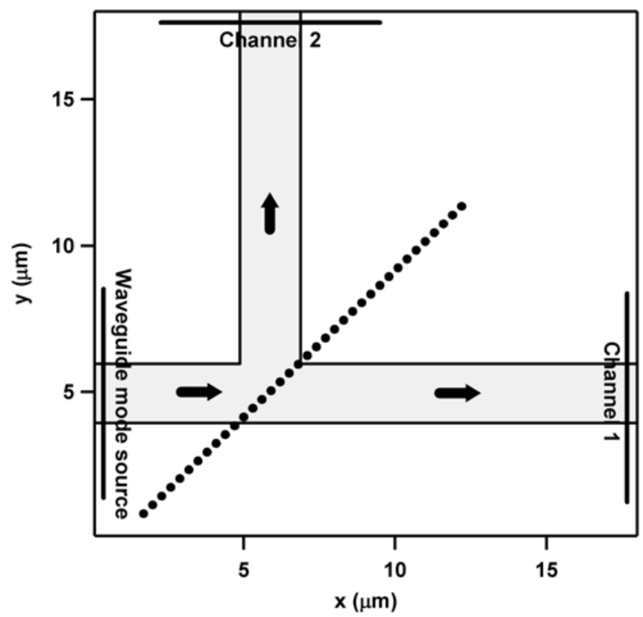

(b)

Figure 7.1. Hybrid PhC and CWG structures for (a) a high efficiency 90 degree bend and (b) a high efficiency beam splitter. Square inset in Figure 7.1(a) indicate the Brillouin zone of the PhC.

In Figure 7.2, the bend efficiency of the 90 degree bend structure as a function of wavelength is presented along with efficiencies at the two output channels of the splitter.

The bend efficiency over the wavelength range on the horizontal axis (C band for optical communication) is greater than 99% because there is no possible mode in the PhC region and no possible diffraction orders from the periodic boundary layer for the wavelength in this range [37]. For the splitter, the 45 degree tilted single row of Si posts is a subwavelength grating structure that allows only reflected and transmitted zero orders [37]. The efficiencies at the output channels 1 and 2 of the splitter are 40.4%~41.6% and 57.9%~59.2% over the wavelength range (total efficiency > 99%).

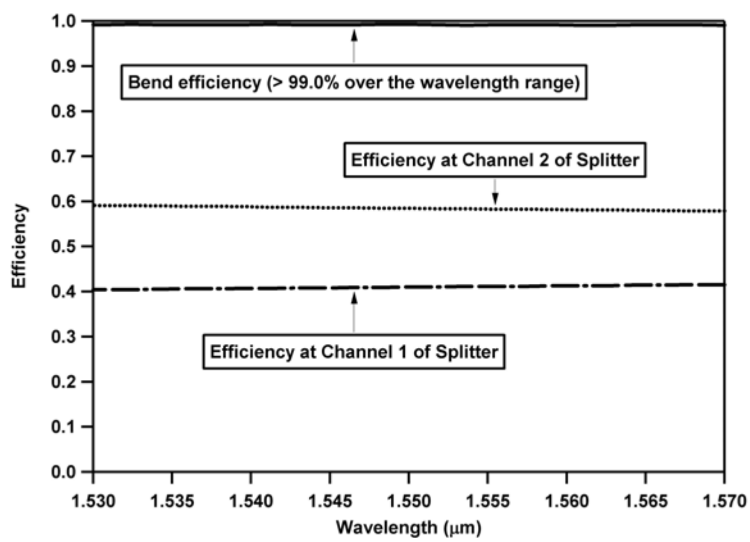

Figure 7.2. Efficiencies as a function of wavelength for TM polarization. Solid line indicates the bend efficiency of the hybrid structure while other two lines correspond to the efficiencies at channels of the splitter.

Figure 7.3 shows a base ring resonator combining hybrid 90 degree bend and splitter structures. The area occupied by the base ring resonator is 35μm x 50μm. Due to the large computational requirements for the numerical simulation of ring resonators, a 2-

D FDTD code is parallelized in order that the computation can be done by multiple CPUs (a parallelized 2-D FDTD). As shown in Figure 7.3, an 8μm wide waveguide mode source is launched at the input waveguide and the efficiencies on both drop and throughput ports are calculated at the 8μm wide detector lines. The spectral responses at the drop and throughput ports of the base structure are shown in Figure 7.4.

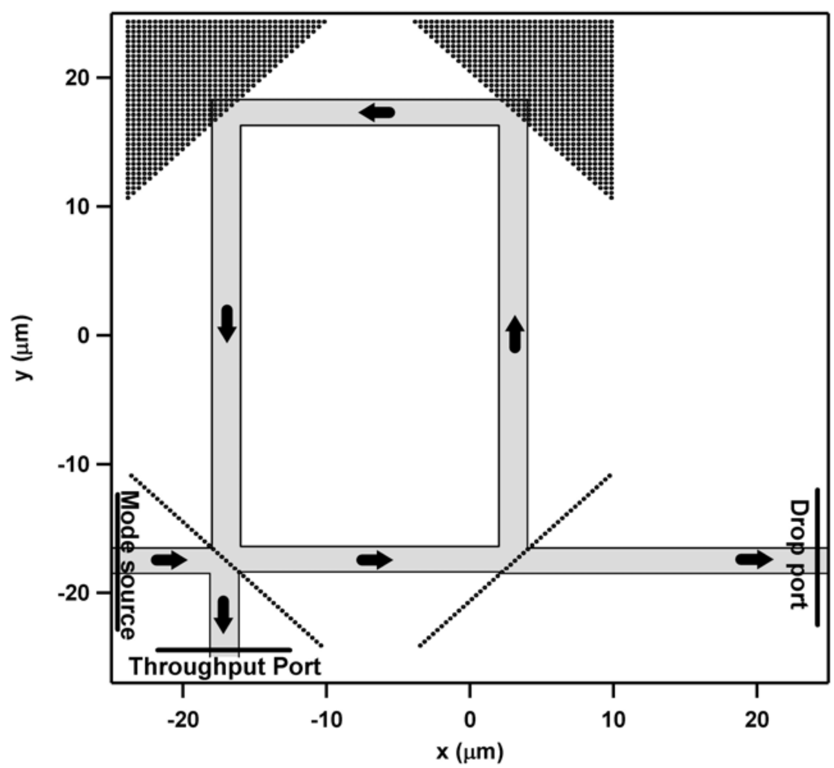

Figure 7.3. Geometry for the base ring resonator constructed with hybrid PhC and CWG structures. To maximize the efficiency, the throughput port is shifted 120nm to left and the waveguide in the middle of two splitters is shifted 120nm up.

As shown in Figure 7.4, the base ring resonator has the drop wavelength efficiency of 92.7% with a 2.5nm FWHM, a 14.1nm FSR, and a 595 Q factor. The extinction ratio calculated as a ratio of the power calculated from the throughput port to the power at the drop port for the drop wavelength is 13.6dB as shown in Figure 7.4.

Figure 7.5 shows a time snap shot of the electric field for the drop wavelength as calculated by our parallelized 2-D FDTD.

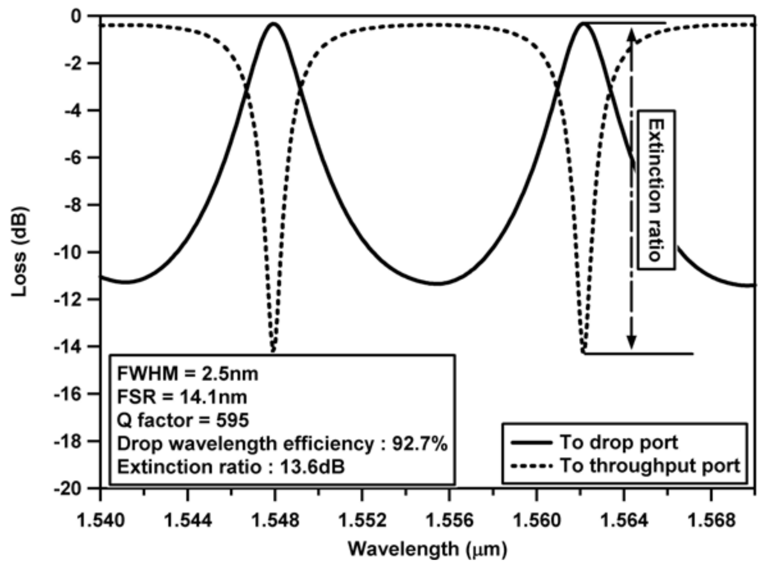

Figure 7.4. Spectral responses of the base ring resonator at the drop (solid line) and throughput (dashed line) ports.

To understand more detail of this new ring resonator configuration, I derived an equation for the efficiency calculation at the drop port. One can easily obtain the equation shown in Equation (7.1) with the method generally used to derive the transmission equation of a Fabry-Perot resonator [76].

$$Efficiency = \frac{T_S^2 / (1-R_S R_b)^2}{1+[4R_S R_b / (1-R_S R_b)^2]\sin^2\frac{\phi}{2}}, \tag{7.1}$$

$$\phi = \theta + 2\pi Nd/\lambda_0, \tag{7.2}$$

where the T_s and R_s are the efficiencies of the splitter at the output channels 1 and 2, R_b is the bend efficiency, θ correspond to the total phase delay at the splitters and bends, and d is the light propagation distance in the ring resonator. The free space wavelength is λ_0 and N is the effective index of the waveguide. Detailed explanations of Equation (7.1) for the given ring resonator geometry are given in the Appendix.

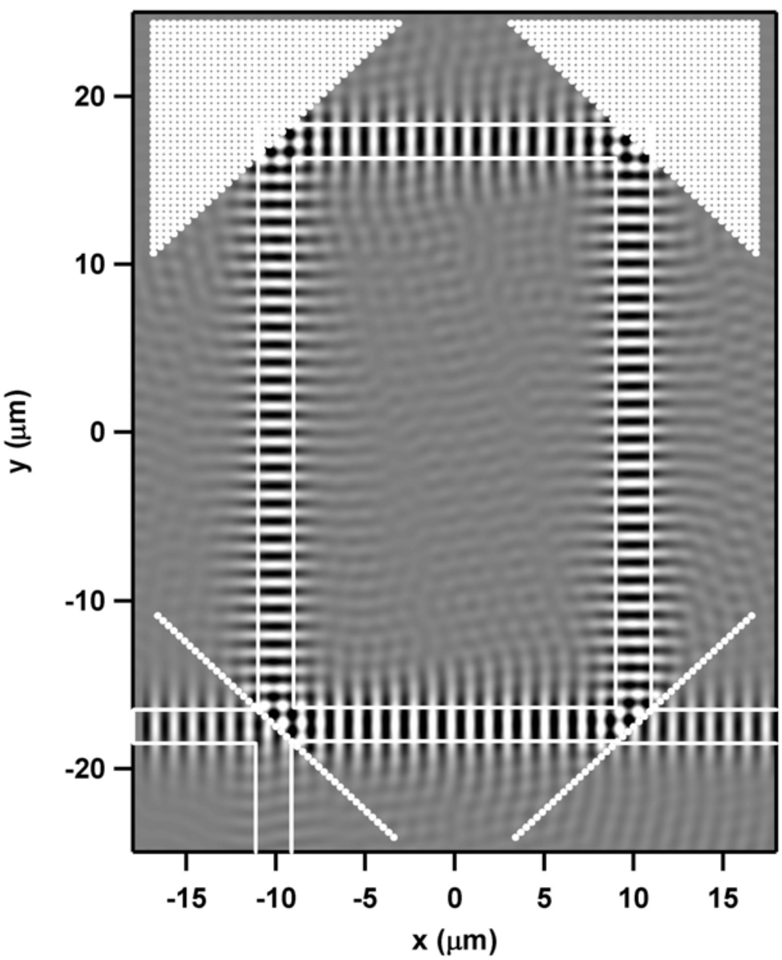

Figure 7.5. Time snap shot of the electric field at the drop wavelength. The computation is done by 4 CPUs with the parallelized 2-D FDTD. Yee cell size: 15nm and time step: 500,000.

As seen from Equation (7.1), the efficiencies at the drop port are maximum when sin(ϕ/2) goes to zero. Therefore, the drop wavelengths, which have maximum efficiency at the drop port, satisfy $\phi = 2m\pi$ (where m=0,1,2,3…..). Since ϕ is a function of the light propagation distance *d* for the given waveguide and hybrid structures for bends and splitters, the FSR of the ring resonator can be increased or decreased by changing *d*. Note that the Q factor of the base ring resonator can be changed by varying R_s or R_b. For the fixed *d*, since the phase delay accompanied by the variation of R_s or R_b is negligible, the spectral response of the ring resonator at the drop port is getting sharper or wider depending upon R_s or R_b which in turn change the FWHM of the peak. As the Q factor is a function of FWHM, therefore, the Q factor can be changed by R_s or R_b. In order to increase the Q factor from the base ring resonator, R_s is the only factor can be increased because R_b of the base ring resonator has already a maximum value.

Based on this understanding, the base ring resonator structure has been modified for obtaining resonators with a wider FSR or a higher Q factor than the base ring resonator.

7.3 Ring resonators with larger FSR and Q factor than the base structure

As shown in Figure 7.6, the hybrid 90 degree bend structures are moved down 15μm to the negative Y direction in order to decrease the light propagation distance in the ring resonator which in turn increases the FSR. Compared with the base ring resonator, all structures are remained same except the area occupied by the ring resonator (35μm x 35μm).

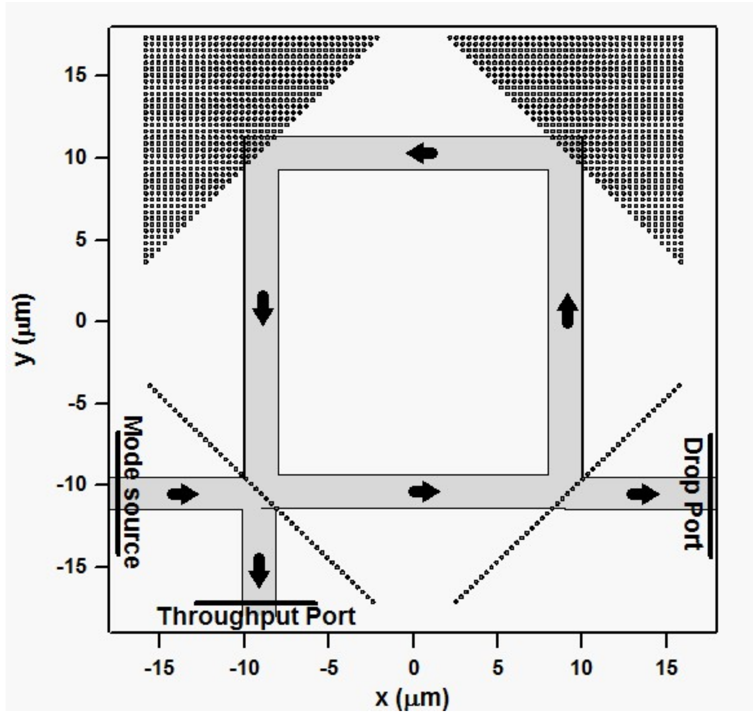

Figure 7.6. Ring resonator geometry which occupies 35μm x 35μm to increase the FSR.

The spectral responses for the modified and base ring resonators are shown in Figure 7.7 for comparison. The FSR is increased to 19.8nm and the drop wavelength efficiency is 91.0%. This wide FSR with high drop wavelength efficiency is an advantage of the proposed ring resonator configuration because this cannot be achieved from the low index contrast CWG ring resonator configuration. Even though a ring resonator structure is modified to increase the FSR, a ring resonator which has much smaller FSR can be realized by just increasing the overall ring resonator size. This wide adjustable range of FSR is another advantage of our ring resonator configuration.

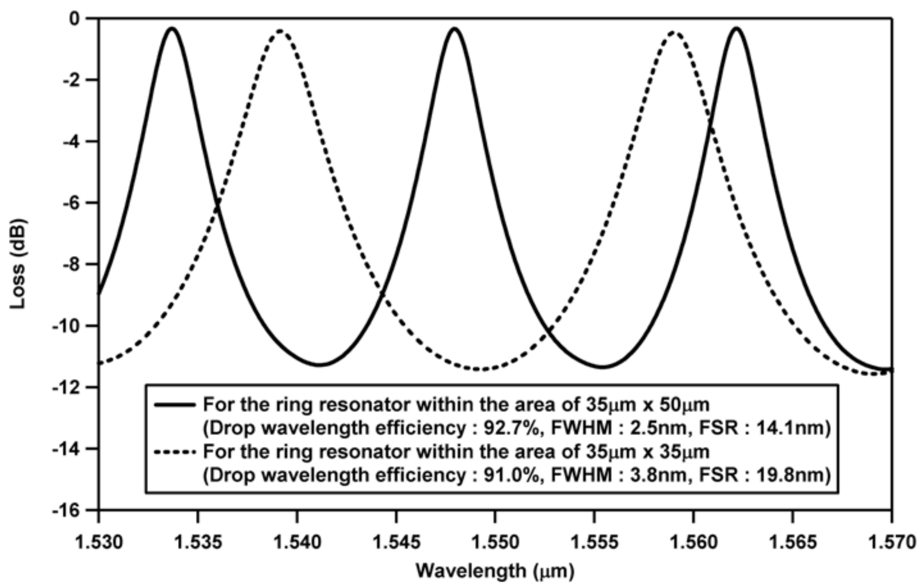

Figure 7.7. Spectral responses for the ring resonator which occupies 35μm x 35μm (dotted curve) compared with the base ring resonator structure (solid curve).

The Q factor of ring resonator can be also improved quite easily by increasing the power directed to channel 2 (R_s in Equation (7.1)) of the splitter while keeping the overall splitter efficiency high. As shown in Figure 7.8(a), another row of Si posts to the splitter (300nm separation in the x direction between the two rows of posts) is added to increase the power along channel 2. The output waveguide positions are adjusted to maximize the efficiency at each channel. The efficiencies as a function of wavelength for both channels are shown in Figure 7.8(b) for several different designs and compared with those of a single row of Si posts.

Efficiencies calculated at the drop port for ring resonators with double Si posts array splitters are shown in Figure 7.9 together with those of the base ring resonator structure for comparison.

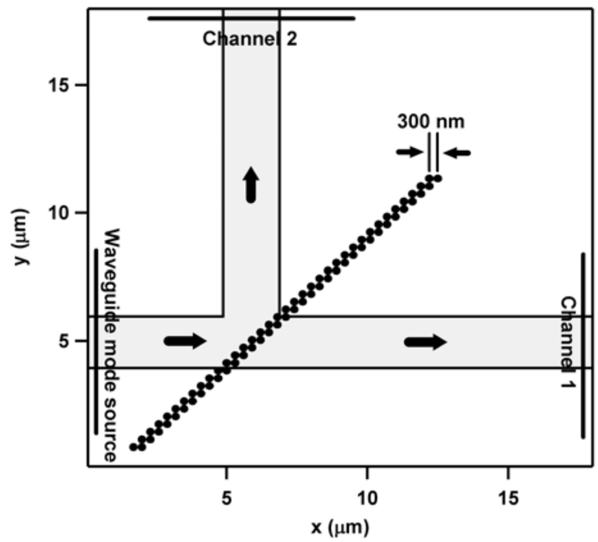

(a)

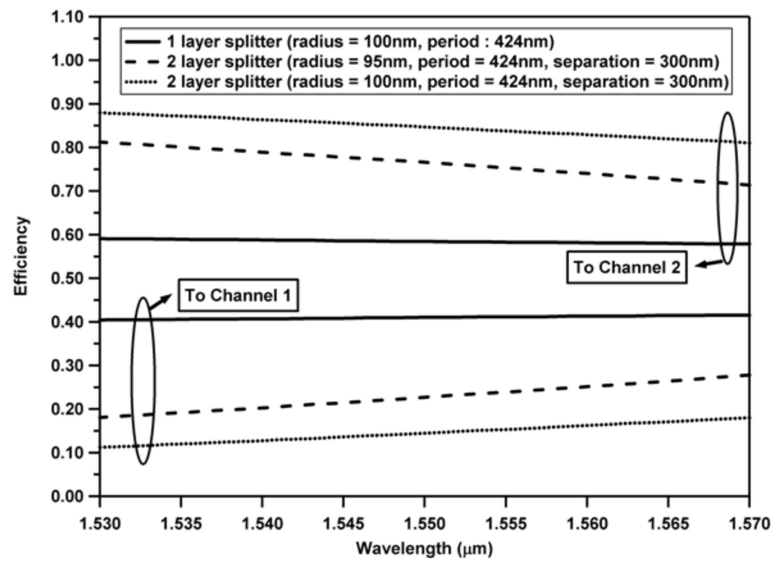

(b)

Figure 7.8. (a) The double Si posts array splitter structures with 100nm Si post radius and (b) spectral responses of all single and double Si posts array splitters as a function of wavelength. Solid line corresponds to the single Si posts array splitter and dashed and dotted lines are for the double Si posts array splitters with 95nm and 100 nm Si posts radii, respectively.

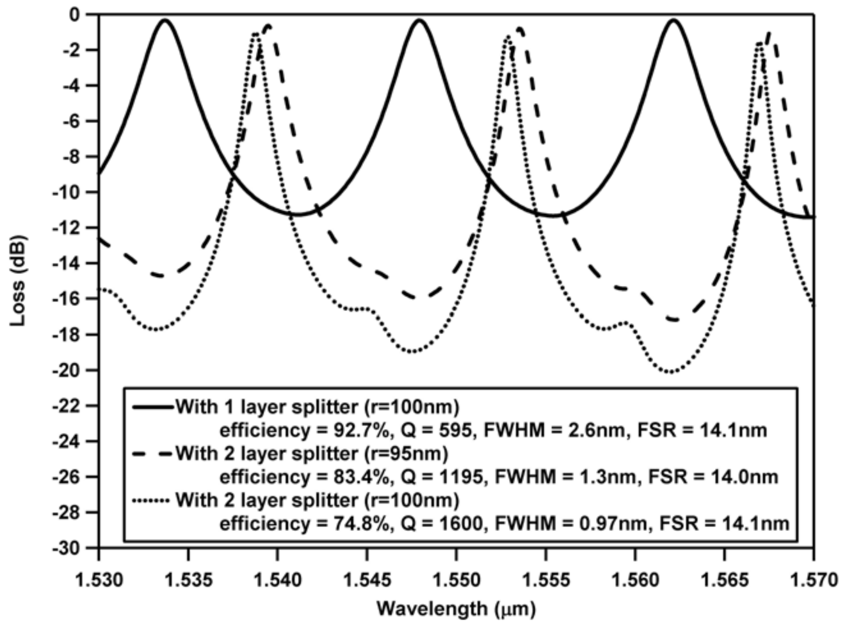

Figure 7.9. The efficiencies at the drop port of the ring resonators using single Si posts array splitter (solid line), double Si posts array splitter with 95nm radius (dashed line) and 100 nm radius (dotted line).

As seen from Figure 7.9, the ring resonator with double layer splitters comprised of 100nm radius Si posts has the Q factor of 1600 with the FSR of 14.1nm. Since the efficiency along the channel 1 (T_s in Equation (7.1)) is decreased and the efficiencies of hybrid structures for bends and splitters are less than 1, the drop wavelength efficiency is decreased to the 74.8%. An approach to design a ring resonator with high Q factor and high drop wavelength efficiency is increasing the overall ring resonator size which is not considered here. Even though the FSR of the ring resonator will be decreased with this approach, the Q factor will be increased while keeping the high drop wavelength efficiency.

7.4 Conclusion

A new configuration of ring resonator which has a relatively wide design freedom to achieve large FSR and Q factor is proposed in this Chapter. As examples, a ring resonator having 14.1nm FSR with 92.7% drop wavelength efficiency is presented. Then, the concepts and methods are discussed to modify the ring resonator to achieve a 19.8nm FSR ring resonator with 91.0% drop wavelength efficiency and a 1600 Q factor ring resonator with 14.1nm FSR. The proposed structure can be applied to any waveguide structure with proper design of the PhC region and the periodic structure for bends and splitters, respectively. This single ring resonator can be used as a building block for designing many different functional devices, such as compact add/drop filters, dense wavelength division demultiplexers, all pass filters, and all optical switches.

Chapter 8

DISCUSSION AND CONCLUSIONS

The focus of this dissertation is to design and propose hybrid PhC and CWG structures as an alternative approach to achieve ultracompact PLCs. High efficiency waveguide bends, splitters, polarizing beam splitter, Mach-Zender interferometer, and ring resonators within very small areas compared with conventional designs have been proposed and analyzed. To understand diffractive behaviors at the periodic boundary layer of PhC, wave vector diagrams are employed. For some waveguide bend designs, a μGA is used to suppress undesired diffractions and maximize bend efficiencies. All detail parameters considered for optimizations are presented. Bend efficiencies after μGA optimization are significantly improved not only for target wavelengths but also over wide wavelength ranges. A Mach-Zender and ring resonator structures combining ultracompact high efficiency bends and splitters show the possible applications of hybrid structures.

In this chapter, a summary of those hybrid PhC and CWG structures is presented and some future research plans follow.

8.1 Summary

After the basic concepts and tools are introduced (Chapter 2), hybrid PhC and CWG structures for a low refractive index waveguide to achieve ultracompact high efficiency 90 degree bend, splitter, and Mach-Zender interferometer are presented (Chapter 3). PhC composed of square lattice array of Si posts is placed at the corner of waveguides to change the light propagation direction to output waveguide which is at 90 degrees with respect to the input waveguide. The bend efficiency is 98.7%. The splitters have overall efficiencies greater than 99.4%. A Mach-Zender interferometer occupying only 18μm x 18μm area with high efficiency of 97.8% is designed by combining hybrid structures of 90 degree bends and splitters.

From a wave vector diagram analysis, it is found that the TE polarized light has a propagation mode for the PhC structure composed of a square Si posts array (Chapter 4). Detail analyses for the behavior of TE polarized light at the PhC structure lead to an ultracompact high efficiency polarizing beam splitter. The propagation direction of TE polarized light in the PhC region is carefully decided from the wave vector diagram and waveguides are designed to follow that direction. The designed polarizing beam splitter which occupies only an 15 μm X 10 μm area shows high efficiency (99.3% for TM polarized light and 99.0% for TE polarized light) with high extinction ratio (28.0dB for TM polarization and 32.2dB for TE polarization). From the tolerance analysis, wide tolerances for possible fabrication errors are obtained.

Hybrid structures for a high refractive index waveguide with low index contrast between core and clad are followed (Chapter 5). First of all, air hole PhC structures are considered to achieve high efficiency 90 degree waveguide bends for both TE and TM polarizations. A triangular lattice array of air holes is used for the TE polarization while a square lattice array is used for TM polarization based on their directional bandgap size. Diffractions for both polarizations at the boundary layers of PhCs limit the maximum bend efficiencies. A μGA with 2-D FDTD is efficiently used to optimize structures by suppressing undesired diffractions. After the optimization, the bend efficiencies for TE and TM polarizations are improved to 92.5% and 97.4%, respectively. A single row of air hole array at 45 degree angle with respect to the input waveguide separate the TM polarized light with 50/50 ratio to two orthogonal output waveguides (99.4% overall efficiency) while 45 degree tilted four rows of air hole array effectively function as a beam splitter for the TE polarized light (98.8% overall efficiency).

Because of the relative ease of fabrication, air hole PhC structures are considered to design ultracompact high efficiency low refractive index waveguide bends (Chapter 6). For TM polarizations, silica and polymer waveguide structures are considered to achieve ultracompact high efficiency 90 degree bend for λ=1.55μm. Diffractions limit the maximum bend efficiency calculated with mode overlap integral (MOI) and μGA is employed again to optimize the boundary structure of the PhC region to suppress them. The MOI bend efficiencies are improved significantly for both cases (99.4% for silica waveguide and 98.95% for polymer waveguide at the wavelength of 1.55μm). Another hybrid high efficiency 90 degree bend structure is designed for λ=1.33μm with another polymer waveguide structure. The MOI bend efficiency is 99.3% after the μGA optimization. These results show that the hybrid PhC and CWG structures for an ultracompact high efficiency 90 degree waveguide bend are not limited by the target wavelengths and waveguide structures.

A new ring resonator configuration by combining the hybrid PhC and CWG structures is proposed (Chapter 7). The waveguide structures considered for building ring resonators are low refractive index waveguides which are used in Chapters 3 and 4. With this ring resonator, much larger FSR compared to the conventional ring resonators is achieved. The FSR and Q factor of the ring resonator are changed by varying overall size or splitter structures. The maximum FSR obtained from a ring resonator is 19.8nm while the Q factor of 1600 is achieved from another ring resonator. Such a ring resonator could be used as a building block for compact add/drop filters, dense wavelength division multi/demultiplexers, all pass filters, and all optical switches.

8.2 Future research

The work presented in this dissertation is mainly numerical designs and analyses of those hybrid PhC and CWG structures which are fundamental components for densely integrated PLCs. The next efforts have to be focused on (1) fabricating those numerically designed hybrid PhC and CWG structures (bends, splitters, polarizing beam splitter, Mach-Zender interferometer, and ring resonator) and (2) designing devices with those hybrid structures.

8.2.1 Fabrication of the hybrid PhC and CWG structures

As an initial investigation for fabricating hybrid PhC and CWG structures, a triangular air hole PhC structure in Si substrate is fabricated from the NMDL. The electron beam lithography is used to pattern periodic holes in PMMA and those patterns are transferred into the Si substrate by the reactive ion etching (RIE).

The future research is needed to develop high aspect ratio etching techniques for various waveguide materials using RIE and inductively coupled plasma RIE (ICP-RIE) which are facilitated in the NMDL. As indicated from the 3-D FDTD simulation results [41], the depths of periodic dielectric materials for the PhC affect the bend efficiency significantly. Uniformity of the size of etched air holes and roughness of sidewall should be also considered carefully. Test methods for comparing the results from the numerical simulations and fabricated samples have to be addressed too.

8.2.2 Design devices using hybrid PhC and CWG structures

By combining fundamental hybrid PhC and CWG structures presented in this dissertation, many useful devices can be realized. Ring resonators and a Mach-Zender interferometer are presented as examples of possible applications. The future research is needed to design many densely integrated PLCs using those hybrid structures, such as add/drop filters, wavelength division multi/demultiplexers, band pass filters, and all optical switches.

However, since the overall size for those devices could be much bigger than the structures presented in this dissertation, an alternative method for designing such structures has to be considered together. The numerical computation of FDTD method for such a large computational size is a time consuming job and requires huge computation resources. The plane wave base MPB is not enough for calculating devices' responses.

As shown in Chapter 7 and the Appendix, I present an analytical expression for the efficiency calculation at the drop port of a ring resonator combining hybrid structures. As seen from the equation, a ring resonator response can be calculated based on the amplitude and phase responses of those fundamental hybrid structures (bends and splitters). As a first step toward this approach, responses from those hybrid structures should be calculated based on the rigorous numerical calculation (2-D FDTD). Those results should be verified by comparing results from the analytical calculation and 2-D FDTD for a relatively simple ring resonator or Mach-Zender interferometer. Those verified analytical methods can be used to design other functional devices.

APPENDIX

ANALYSIS FOR THE RING RESONATOR USING HYBRID PHOTONIC CRYSTAL AND CONVENTIONAL WAVEGUIDE STRUCTURES

A ring resonator combining the hybrid PhC and CWG structures can be simplified as shown in Figure A.1. The structure has two 90 degree bend structures (with reflection coefficient of r_{b1} or r_{b2} and phase delay of θ_{b1} or θ_{b2}) and two splitters (with reflection coefficient of r_{s1} or r_{s2}, transmission coefficient of t_{s1} or t_{s2}, and phase delays expressed by θ_{sr1}, θ_{sr2}, θ_{st1}, or θ_{st2}).

For the given incident field of

$$\overline{E}_{inc} = \left|\overline{E_0}\right| \exp j(\theta_0) \;\; (\left|\overline{E_0}\right| \text{: input field amplitude, } \theta_0 \text{: input phase}), \tag{A.1}$$

fields at the drop port after passing through the ring resonator can be expressed as shown in Equation (A.2).

$$\overline{E}_1 = \left|\overline{E_0}\right| t_{s1} t_{s2} \exp j(\theta_0 + \theta_{st1} + \theta_{st2} + \beta s) ,$$

$$\overline{E}_2 = \left|\overline{E_0}\right| t_{s1} r_{s2} r_{b1} r_{b2} r_{s1} t_{s2} \exp j(\theta_0 + \theta_{b1} + \theta_{b2} + \theta_{sb1} + \theta_{sb2} + \theta_{st1} + \theta_{st2} + \beta s + \beta d) ,$$

$$\overline{E}_3 = \left|\overline{E_0}\right| t_{s1} r_{s2}^2 r_{b1}^2 r_{b2}^2 r_{s1}^2 t_{s2} \exp j(\theta_0 + 2\theta_{b1} + 2\theta_{b2} + 2\theta_{sb1} + 2\theta_{sb2} + 2\beta d + \theta_{st1} + \theta_{st2} + \beta s) ,$$

$$\overline{E}_4 = \left|\overline{E_0}\right| t_{s1} r_{s2}^3 r_{b1}^3 r_{b2}^3 r_{s1}^3 t_{s2} \exp j(\theta_0 + 3\theta_{b1} + 3\theta_{b2} + 3\theta_{sb1} + 3\theta_{sb2} + 3\beta d + \theta_{st1} + \theta_{st2} + \beta s) ,$$

…………………………………

$$\overline{E}_{p+1} = \left|\overline{E_0}\right| t_{s1} r_{s2}^{p} r_{b1}^{p} r_{b2}^{p} r_{s1}^{p} t_{s2} \exp j(\theta_0 + p\theta_{b1} + p\theta_{b2} + p\theta_{sb1} + p\theta_{sb2} + p\beta d + \theta_{st1} + \theta_{st2} + \beta s),$$

and

$$\overline{E}_{drop} = \overline{E_1} + \overline{E_2} + \overline{E_3} + \overline{E_4} + \bullet\bullet\bullet + \overline{E_{p+1}}$$

$$= \left|\overline{E_0}\right| t_{s1} t_{s2} \exp j(\theta_0 + \theta_{st1} + \theta_{st2} + \beta s) \sum_{l} r_{s1}^{l} r_{s2}^{l} r_{b1}^{l} r_{b2}^{l} \exp jl(\theta_{sb1} + \theta_{sb2} + \theta_{b1} + \theta_{b2} + \beta d),$$

(and l = 0, 1, 2, 3, 4, ……p), (A.2)

where the $\overline{E}_{drop}$ denotes the electric field at the drop port while β, s, and d correspond to the propagation constant, separation between two splitters, and the overall propagation distance in the ring resonator, respectively.

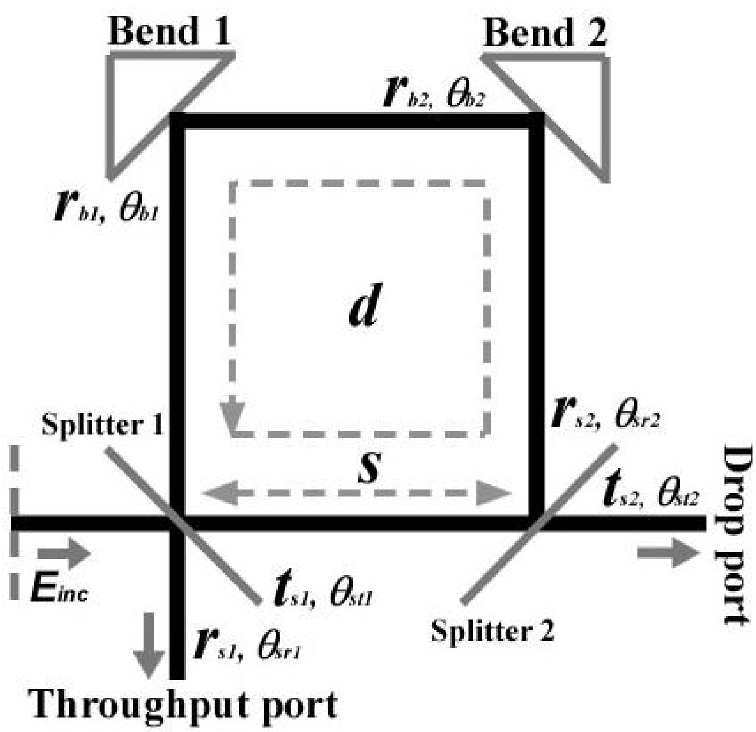

Figure A.1. Geometry of ring resonator for an analysis.

Then, $\overline{E}_{drop}$ can be simplified to

$$\overline{E}_{drop} = \frac{\left|\overline{E_0}\right| t_{s1} t_{s2} \exp j(\delta)(1 - r_{s2}^{p} r_{b1}^{p} r_{b2}^{p} r_{s1}^{p} \exp jp\phi)}{(1 - r_{s2} r_{b1} r_{b2} r_{s1} \exp j\phi)}, \tag{A.3}$$

where $\delta = \theta_0 + \theta_{st1} + \theta_{st2} + \beta s$ and $\phi = \theta + 2\pi Nd/\lambda_0$ ($\theta = \theta_{b1} + \theta_{b2} + \theta_{sb1} + \theta_{sb2}$, $\beta = 2\pi N/\lambda_0$), N : effective index of waveguide mode, λ_0 : free space wavelength).

Because r_{b1}, r_{b2}, r_{s1}, and r_{s2} are less than 1, Equation (A.3) is even simplified as p in Equation (A.3) goes to infinity. Now, $\overline{E}_{drop}$ can be expressed by

$$\overline{E}_{drop} = \frac{\left|\overline{E_0}\right| t_{s1} t_{s2} \exp j(\delta)}{(1 - r_{s2} r_{b1} r_{b2} r_{s1} \exp j\phi)}. \tag{A.4}$$

The drop wavelength efficiency of a ring resonator, which is a ratio of the power at the drop port to the input power, can be calculated by

$$\frac{P_{drop}}{P_{inc}} = \frac{\left|\overline{E_{drop}}\right|^2}{\left|\overline{E_0}\right|^2} = \frac{t_{s1}^2 t_{s2}^2}{[(1 - r_{s1}^2 r_{s2}^2 r_{b1}^2 r_{b2}^2) - 2 r_{s1} r_{s2} r_{b1} r_{b2} \cos(\phi)]}. \tag{A.5}$$

Finally, the expression for the drop wavelength efficiency η of a ring resonator is

$$\eta = \frac{\dfrac{t_{s1}^2 t_{s2}^2}{(1 - r_{s1} r_{s2} r_{b1} r_{b2})^2}}{1 + [\dfrac{4 r_{s1} r_{s2} r_{b1} r_{b2}}{(1 - r_{s1} r_{s2} r_{b1} r_{b2})^2}] \sin^2(\dfrac{\phi}{2})}. \tag{A.6}$$

This is a general expression of drop wavelength efficiency.

Now, let us consider the special case considered in Chapter 7.

For this case, the following relations are satisfied.

$r_{b1} = r_{b2}$,

$r_{s1} = r_{s2}$,

$t_{s1} = t_{s2}$,

$\theta_{b1} = \theta_{b2}$,

$\theta_{sb1} = \theta_{sb2}$. (A.7)

Then, Equation (A.5) is

$$\eta = \frac{\dfrac{T_s^2}{(1-R_s R_b)^2}}{1+[\dfrac{4R_s R_b}{(1-R_s R_b)^2}]\sin^2(\dfrac{\phi}{2})}, \tag{A.8}$$

where T_s is the efficiency at the output waveguide passing through the splitter ($T_s = t_{s1}^2 = t_{s2}^2$) while R_s is the efficiency at the output waveguide which is at 90 degree angle with respect to the input waveguide. The efficiency of the 90 degree bend is denoted as R_b. The phase term in Equation (A.8) is

$$\phi = \theta + 2\pi Nd/\lambda_0, \tag{A.9}$$

where $\theta = 2\theta_b + 2\theta_{sb}$. (A.10)

Equations (A.8), (A.9), and (A.10) can be used to calculate the spectral responses at the drop port for ring resonators shown in Chapter 7.

REFERENCES

[1] M. Koshiba, *Optical waveguide analysis*, (McGraw-Hill, New York, 1992).

[2] H. Nishihara, M. Haruna, and T. Suhara, *Optical integrated circuits*, (McGraw-Hill, New York 1989).

[3] K. Okamoto, *Integrated optical circuits and components: Design and applications*, edited by E. J. Murphy, (Marcel Dekker, New York, 1999), Chap. 4, p. 55-87.

[4] D. L. Lee, *Electromagnetic principles of integrated optics*, (John Wiley & Sons, New York, 1986).

[5] C. T. Lee and M. L. Wu, "Apexes-linked circle gratings for low-loss waveguide bends," IEEE Photon. Technol. Lett., **13**, 597-599 (2001).

[6] R. A. Jarvis, J. D. Love, and F. Ladouceur, "Bend-radius reduction in planar waveguides using UV post-tuning," Electron. Lett., **33**, 892-894 (1997).

[7] R. L. Espinola, R. U. Ahmad, F. Pizzuto, M. J. Steel, and R. M. Osgood, "A study of high-index-contrast 90 degree waveguide bend structures," Opt. Express, **8,** 517-528 (2001), http://www.opticsexpress.org/abstract.cfm?URI=OPEX-8-9-517.

[8] M. Popovic, K. Wada, S. Akiyama, H. A. Haus, and J. Michel, "Air trenches for sharp silica waveguide bends," J. Lightwave Techonol., **20**, 1762-1772 (2002).

[9] S. Lardenois, D. Pascal, L. Vivien, E. Cassan, and S. Laval, "Low-loss submicrometer silicon-on-insulator rib waveguides and corner mirrors," Opt. Lett., **28**, 1150-1152 (2003).

[10] E. Yablonovitch, "Inhibited spontaneous emission in solid-state physics and electronics," Phys. Rev. Lett., **58**, 2059-2062 (1987).

[11] See for example the special issue on photonic crystals in IEEE J. Quant. Elect., **38**, (2002).

[12] H. Benisty, C. Weisbuch, D. Labilloy, M. Rattier, C. J. M. Smith, T. F. Krauss, R. M. D. L. Rue, R. Houdre, U. Oesterle, C. Jouanin, and D. Cassagne, "Optical and confinement properties of two-dimensional photonic crystals," J. Lightwave Technol., **17**, 2063-2077 (1999).

[13] S. G. Johnson, P. R. Villeneuve, S. Fan, and J. D. Joannopoulos, "Linear waveguides in photonic-crystal slabs," Phys. Rev. B, **62**, 8212-8222 (2000).

[14] T. Baba, A. Motegi, T. Iwai, N. Fukaya, Y. Watanabe, and A. Sakai, "Light propagation characteristics of straight single-line-defect waveguides in photonic crystal slabs fabricated into a silicon-on-insulator substrate," IEEE J. Quantum Electron., **38**, 743-752 (2002).

[15] Y. Sugimoto, N. Ikeda, N. Carlsson, K. Asakawa, N. Kawai, and K. Inoue, "AlGaAs-based two-dimensional photonic crystal slab with defect waveguides for planar lightwave circuit applications," IEEE J. Quantum Electron., **38**, 760-769 (2002).

[16] A. Adibi, Y. Xu, R. K. Lee, A. Yariv, and A. Scherer, "Properties of the slab modes in photonic crystal optical waveguides," J. Lightwave Technol., **18**, 1554-1564 (2000).

[17] M. Loncar, T. Doll, J. Vuckovic, and A. Scherer, "Design and fabrication of silicon photonic crystal optical waveguides," J. Lightwave Technol., **18**, 1402-1411 (2000).

[18] A. Chutinan and S. Noda, "Waveguides and waveguide bends in two-dimensional photonic crystal slabs," Phys. Rev. B, **62**, 4488-4492 (2000).

[19] S. Y. Lin, E. Chow, S. G. Johnson, and J. D. Joannopoulos, "Demonstration of highly efficient waveguiding in a photonic crystal slab at the 1.5-μm wavelength," Opt. Lett., **25**, 1297-1299 (2000).

[20] A. Talneau, L. L. Gouezigou, and N. Bouadma, "Quantitative measurement of low propagation losses at 1.55μm on planar photonic crystal waveguides," Opt. Lett., **26**, 1259-1261 (2001).

[21] M. Notomi, A. Shinya, K. Yamada, J. Takahashi, C. Takahashi, and I. Yokohama, "Structural tuning of guiding modes of line-defect waveguides of silicon-on-insulator photonic crystal slabs," IEEE J. Quantum Electron., **38**, 736-742 (2002).

[22] A. Talneau, L. L. Gouezigou, N. Bouadma, M. Kafesaki, C. M. Soukoulis, and M. Agio, "Photonic-crystal ultrashort bends with improved transmission and low reflection at 1.55 μm," Appl. Phys. Lett., **80**, 547-549 (2002).

[23] H. Benisty, S. Olivier, C. Weisbuch, M. Agio, M. Kafesaki, C. M. Soukoulis, M. Qiu, M. Swillo, A. Karlsson, B. Jaskorzynska, A. Talneau, J. Moosburger, M. Kamp, A. Forchel, R. Ferrini, R. Houdre, and U. Oesterle, "Models and measurements for the transmission of submicron- width waveguide bends defined in two-dimensional photonic crystals," IEEE J. Quantum Electron., **38**, 770-785 (2002).

[24] S. Olivier, H. Benisty, C. Weisbuch, C. J. M. Smith, T. F. Krauss, R. Houdre, and U. Oesterle., "Improved 60° bend transmission of submicron-width waveguides defined in two-dimensional photonic crystals," J. Lightwave Technol., **20**, 1198-1203 (2002).

[25] Y. Sugimoto, N. Ikeda, N. Carlsson, K. Asakawa, N. Kawai, and K. Inoue, "Light-propagation characteristics of Y-branch defect waveguides in AlGaAs-based air-bridge-type two-dimensional photonic crystal slabs," Opt. Lett., **27**, 388-390 (2002).

[26] S. Boscolo, M. Midrio, and T. F. Krauss, "Y junctions in photonic crystal channel waveguides: High transmission and impedance matching," Opt. Lett., **27**, 1001-1003 (2002).

[27] O. Painter, A. Husain, A. Scherer, P. T. Lee, I. Kim, J. D. O'Brien, and P. D. Dapkus, "Lithographic tuning of a two-dimensional photonic crystal laser array," IEEE Photon. Technol. Lett., **12**, 1126-1128 (2000).

[28] S. Y. Lin, E. Chow, S. G. Johnson, and J. D. Joannopoulos, "Direct measurement of the quality factor in a two-dimensional photonic-crystal microcavity," Opt. Lett., **26**, 1903-1905 (2001).

[29] H. Benisty, D. Labilloy, C. Weisbuch, C. J. M. Smith, T. F. Krauss, D. Cassagne, A. Beraud, and C. Jouanin, "Radiation losses of waveguide-based two-dimensional photonic crystals: Positive role of the substrate," Appl. Phys. Lett., **76**, 532-534 (2000).

[30] W. Bogaerts, P. Bienstman, D. Taillaert, R. Baets, and D. D. Zutter, "Out-of-plane scattering in photonic crystal slabs," IEEE Photon. Technol. Lett., **13**, 565-567 (2001).

[31] P. Lalanne and H. Benisty, "Out-of-plane losses of two-dimensional photonic crystals waveguides: Electromagnetic analysis," J. Appl. Phys., **89**, 1512-1514 (2001).

[32] P. Lalanne, "Electromagnetic analysis of photonic crystal waveguides operating above the light cone," IEEE J. Quantum Electron., **38**, 800-804 (2002).

[33] M. Tokushima and H. Yamada, "Light propagation in a photonic-crystal-slab line-defect waveguide," IEEE J. Quantum Electron., **38**, 753-759 (2002).

[34] C. Chen, A. Sharkawy, D. M. Pustai, S. Shi, and D. W. Prather, "Optimizing bending efficiency of self-collimated beams in non-channel planar photonic crystal waveguides," Opt. Express, **11,** 3153-3159 (2003), http://www.opticsexpress.org/abstract.cfm?URI=OPEX-11-23-3153.

[35] A. Sharkawy, S. Shi, and D. W. Prather, "Multichannel wavelength division multiplexing with photonic crystals," Appl. Opt., **40**, 2247-2252 (2001).

[36] S. Olivier, C. Smith, M. Rattier, H. Benisty, C. Weisbuch, T. Krauss, R. Houdre, and U. Oesterle, "Miniband transmission in a photonic crystal coupled-resonator optical waveguide," Opt. Lett., **26**, 1019-1021 (2001).

[37] G. P. Nordin, S. Kim, J. Cai, and J. Jiang, "Hybrid integration of conventional waveguide and photonic crystal structures," Opt. Express, **10**, 1334-1341 (2002), http://www.opticsexpress.org/abstract.cfm?URI=OPEX-10-23-1334.

[38] S. Kim, G. P. Nordin, J. Jiang, and J. Cai, "Micro-genetic algorithm design of hybrid conventional waveguide and photonic crystal structures," accepted for publication on Optical Engineering.

[39] S. Kim, G. P. Nordin, J. Cai, and J. Jiang, "Ultracompact high-efficiency polarizing beam splitter with a hybrid photonic crystal and conventional waveguide structure," Opt. Lett., **28**, 2384-2386 (2003).

[40] S. Kim, G. P. Nordin, J. Jiang, and J. Cai, "High efficiency 90 degree silica waveguide bend using an air hole photonic crystal region," accepted for publication on IEEE Photon. Technol. Lett..

[41] J. Cai, G. P. Nordin, S. Kim, and J. Jiang, "3-D Analysis of hybrid conventional waveguide/photonic crystal 90 degree bend," submitted to Appl. Opt.

[42] A. Taflove, *Computational electrodynamics: The finite-difference time-domain method*, (Artech House, Boston, 1995).

[43] J. Jiang and G. P. Nordin, "A rigorous unidirectional method for designing finite aperture diffractive optical elements," Opt. Express, **7**, 237-242 (2000) http://www.opticsexpress.org/abstract.cfm?URI=OPEX-7-6-237.

[44] Jianhua Jiang, Jingbo Cai, G. P. Nordin, and Lixia Li, "Parallel microgenetic algorithm design for photonic crystal and waveguide structures," Opt. Lett., **28**, 2381-2383 (2003).

[45] C. Manolatou, S. G. Johnson, S. Fan, P. R. Villeneuve, H. A. Haus, and J. D. Joannopoulos, "High-density integrated optics," IEEE J. Lightwave technol., **17**, 1682-1692 (1999).

[46] J. D. Joannopoulos, R. D. Meade, and J. N. Winn, *Photonic crystals: Molding the flow of light*, (Princeton University Press, New Jersey, 1995).

[47] K. M. Ho, C. T. Chan, and C. M. Soukoulis, "Existence of a photonic gap in periodic dielectric structures," Phys. Rev. Lett., **65**, 3152-3154 (1990).

[48] H. S. Sozuer, J. W. Haus, and R. Inguva, "Photonic bands: Convergence problems with the plane-wave method," Phys. Rev. B, **45**, 13962-13972 (1992).

[49] J. P. Berenger, "A perfectly matched layer for the absorption of electromagnetic waves," J. Comput. Phys., **114**, 185-200 (1994).

[50] S. G. Johnson and J. D. Joannopoulos, *Photonic crystals: The road from theory to practice*, (Kluwer Academic Publishers, Massachusetts, 2002).

[51] S. J. McNab, N. Moll, and Y. A. Vlasov, "Ultra-low loss photonic integrated circuit with membrane-type photonic crystal waveguides," Opt. Express, **11**, 2927-2939 (2003), http://www.opticsexpress.org/abstract.cfm?URI=OPEX-11-22-2927.

[52] K. S. Yee, "Numerical solution of initial boundary value problems involving Maxwell's equations in isotropic media," IEEE Trans. Antennas Propagation, **AP-14**, 302-307 (1966).

[53] J. Jiang, *Rigorous analysis and design of diffractive optical elements*, Ph.D. thesis, University of Alabama in Huntsville, 2000.

[54] P. S. J. Russell, T. A. Birks, and F. D. L. Lucas, "Photonic bloch waves and photonic band gaps" in *Confined electrons and photonics: New physics and applications*, edited by E. Burstein, C. Weisbuch, (Plenum Press, New York, 1995).

[55] M. Notomi, "Theory of light propagation in strongly modulated photonic crystals: Refractionlike behavior in the vicinity of the photonic band gap," Phys. Rev. B, **62**, 10,696-10,705 (2000).

[56] T. Baba and M. Nakamura, "Photonic crystal light deflection devices using the superprism effect," J. Quant. Elect., **38**, 909-914 (2002).

[57] R. M. de Ridder, A. F. M. Sander, A. Driessen, and J. H. J. Fluitman, "An integrated optic adiabatic TE/TM mode splitter on silicon," J. Lightwave Technol., **11**, 1806-1811 (1993).

[58] P. Wei and W. Wang, "A TE-TM mode splitter on lithium niobate using Ti, Ni, and MgO diffusions," Photon. Technol. Lett., **6**, 245-248 (1994).

[59] L. B. Soldano, A. H. de Vreede, M. K. Smit, B. H. Verbeek, E. G. Metaal, and F. H. Groen, "Mach-zehnder interferometer polarization splitter in InGaAsP/InP," Photon. Technol. Lett., **6**, 402-405 (1994).

[60] H. Maruyama, M. Haruna, and H. Nishihara, "TE-TM mode splitter using direction coupling between heterogeneous waveguides in $LiNbO_3$," J. Lightwave Technol., **13**, 1550-1554 (1995).

[61] S. M. Garner, V. Chuyanov, S. Lee, A. Chen, W. H. Steier, and L. R. Dalton, "Vertically integrated waveguide polarization splitters using polymers," Photon. Technol. Lett., **11**, 842-844 (1999).

[62] R. R. A. Syms and J. Cozens, *Optical guided waves and devices*, (McGraw-Hill, New York, 1992), Chap. 6, p. 120-144.

[63] Y. P. Li and C. H. Henry, "Silica-based optical integrated circuits," IEE Proc.-Optoelectron., **143**, 263-280 (1996).

[64] X. Fu, M. Fay, and J. M. Xu, "1 X 8 Supergrating wavelength-division demultiplexer in a silica planar waveguide," Opt. Lett., **22**, 1627-1629 (1997).

[65] A. Kaneko, T. Goh, H. Yamada, T. Tanaka, and I. Ogawa, "Design and applications of silica-based planar lightwave circuits," IEEE J. Select. Topics Quantum Electron., **5**, 1227-1236 (1999).

[66] C. R. Doerr, L. W. Stulz, and R. Pafchek, "Compact and low-loss integrated box-like passband multiplexer," IEEE Photon. Technol. Lett., **15**, 918-920 (2003).

[67] L. G. de Peralta, A. A. Bernussi, S. Frisbie, R. Gale, and H. Temkin, "Reflective arrayed waveguide grating multiplexer," IEEE Photon. Technol. Lett., **15**, 1398-1400 (2003).

[68] W. Chen, Z. Zhu, Y. J. Chen, J. Sun, B. Grek, and K. Schmidt, "Monolithically integrated 32 X four-channel client reconfigurable optical add/drop multiplexer on planar lightwave circuit," IEEE Photon. Technol. Lett., **15**, 1413-1415 (2003).

[69] C. Liguda, G. Bottger, A. Juligk, R. Blum, M. Eich, H. Roth, J. Junert, W. Morgenroth, H. Elsner, and H. G. Meyer, "Polymer photonic crystal slab waveguides," Appl. Phys. Lett., **78**, 2434 – 2436 (2001).

[70] B. E. Little, J. S. Foresi, G. Steinmeyer, E. R. Thoen, S. T. Chu, H. A. Haus, E. P. Ippen, L. C. Kimerling, and W. Greene, "Ultra-compact Si-SiO2 microring resonator optical channel dropping filters," IEEE Photon. Technol. Lett., **10**, 549-551 (1998).

[71] A. Vorckel, M. Monster, W. Henschel, P. H. Bolivar, and H. Kurz, "Asymmetrically coupled silicon-on-insulator microring resonators for compact add-drop multiplexers," IEEE Photon. Technol. Lett., **15**, 921-923 (2003).

[72] P. Rabiei, W. H. Steier, C. Zhang, and L. R. Dalton, "Polymer micro-ring filters and modulators," J. Lightwave Technol., **20**, 1968-1975 (2002).

[73] G. Bourdon, G. Alibert, A. Beguin, B. Bellman, and E. Guiot, "Ultralow loss ring resonators using 3.5% index-contrast Ge-doped silica waveguides," IEEE Photon. Technol. Lett., **15**, 709-711 (2003).

[74] S. T. Chu, B. E. Little, W. Pan, T. Kaneko, S. Sato, and Y. Kokubun, "An eight-channel add-drop filter using vertically coupled microring resonators over a cross grid," IEEE Photon. Technol. Lett., **11**, 691-693 (1999).

[75] B. E. Little, S. T. Chu, W. Pan, and Y. Kokubun, "Microring resonator arrays for VLSI photonics," IEEE Photon. Technol. Lett., **12**, 323-325 (2000).

[76] B. E. A. Saleh and M. C. Teich, *Fundamentals of photonics*, (A Wiley-Interscience Publication, New York, 1991), Chap. 9, p. 310-341.